2016

UNDERSTANDING ELECTRICAL CONDUCTION IN LITHIUM ION BATTERIES THROUGH MULTI-SCALE MODELING

Jie Pan
University of Kentucky, jie.pan@uky.edu

Digital Object Identifier: http://dx.doi.org/10.13023/ETD.2016.237

Recommended Citation

Pan, Jie, "UNDERSTANDING ELECTRICAL CONDUCTION IN LITHIUM ION BATTERIES THROUGH MULTI-SCALE MODELING" (2016). *Theses and Dissertations--Chemical and Materials Engineering*. 62.
https://uknowledge.uky.edu/cme_etds/62

STUDENT AGREEMENT:

I represent that my thesis or dissertation and abstract are my original work. Proper attribution has been given to all outside sources. I understand that I am solely responsible for obtaining any needed copyright permissions. I have obtained needed written permission statement(s) from the owner(s) of each third-party copyrighted matter to be included in my work, allowing electronic distribution (if such use is not permitted by the fair use doctrine) which will be submitted to UKnowledge as Additional File.

I hereby grant to The University of Kentucky and its agents the irrevocable, non-exclusive, and royalty-free license to archive and make accessible my work in whole or in part in all forms of media, now or hereafter known. I agree that the document mentioned above may be made available immediately for worldwide access unless an embargo applies.

I retain all other ownership rights to the copyright of my work. I also retain the right to use in future works (such as articles or books) all or part of my work. I understand that I am free to register the copyright to my work.

REVIEW, APPROVAL AND ACCEPTANCE

The document mentioned above has been reviewed and accepted by the student's advisor, on behalf of the advisory committee, and by the Director of Graduate Studies (DGS), on behalf of the program; we verify that this is the final, approved version of the student's thesis including all changes required by the advisory committee. The undersigned agree to abide by the statements above.

Jie Pan, Student

Dr. Yang-Tse Cheng, Major Professor

Dr. Thomas Dziubla, Director of Graduate Studies

UNDERSTANDING ELECTRICAL CONDUCTION IN LITHIUM ION BATTERIES THROUGH MULTI-SCALE MODELING

DISSERTATION

A dissertation submitted in partial
fulfillment of the requirements for
the degree of Doctor of Philosophy
in the College of Engineering at the
University of Kentucky

By
Jie Pan
Lexington, Kentucky

Director: Dr. Yang-Tse Cheng, Professor of Materials Engineering
Co-Director: Dr. Matthew J. Beck, Associate Professor of Materials Engineering
Lexington, Kentucky

2016

ABSTRACT OF DISSERTATION

UNDERSTANDING ELECTRICAL CONDUCTION IN LITHIUM ION BATTERIES THROUGH MULTI-SCALE MODELING

Silicon (Si) has been considered as a promising negative electrode material for lithium ion batteries (LIBs) because of its high theoretical capacity, low discharge voltage, and low cost. However, the utilization of Si electrode has been hampered by problems such as slow ionic transport, large stress/strain generation, and unstable solid electrolyte interphase (SEI). These problems severely influence the performance and cycle life of Si electrodes. In general, ionic conduction determines the rate performance of the electrode, while electron leakage through the SEI causes electrolyte decomposition and, thus, causes capacity loss. The goal of this thesis research is to design Si electrodes with high current efficiency and durability through a fundamental understanding of the ionic and electronic conduction in Si and its SEI.

Multi-scale physical and chemical processes occur in the electrode during charging and discharging. This thesis, thus, focuses on multi-scale modeling, including developing new methods, to help understand these coupled physical and chemical processes. For example, we developed a new method based on *ab initio* molecular dynamics to study the effects of stress/strain on Li ion transport in amorphous lithiated Si electrodes. This method not only quantitatively shows the effect of stress on ionic transport in amorphous materials, but also uncovers the underlying atomistic mechanisms. However, the origin of ionic conduction in the inorganic components in SEI is different from that in the amorphous Si electrode. To tackle this problem, we developed a model by separating the problem into two scales: 1) atomistic scale: defect physics and transport in individual SEI components with consideration of the environment, e.g., LiF in equilibrium with Si electrode; 2) mesoscopic scale: defect distribution near the heterogeneous interface based on a space charge model. In addition, to help design better artificial SEI, we further demonstrated a theoretical design of multicomponent SEIs by utilizing the synergetic effect found in the natural SEI. We show that the electrical conduction can be optimized by varying the grain size and volume fraction of two phases in the artificial multicomponent SEI.

KEYWORDS: lithium ion batteries, solid electrolyte interphase, amorphous silicon electrode, ionic conduction, diffusion, heterogeneous interface

Author's signature: Jie Pan

Date: June 10, 2016

UNDERSTANDING ELECTRICAL CONDUCTION IN LITHIUM ION BATTERIES THROUGH MULTI-SCALE MODELING

By
Jie Pan

Director of Dissertation: Yang-Tse Cheng

Co-Director of Dissertation: Matthew J. Beck

Director of Graduate Studies: Thomas Dziubla

Date: June 10, 2016

Dedicated to my parents and
the love in my life

ACKNOWLEDGMENTS

Life is an adventure, nobody can make it happen but us! To make me reach this stage, I received a lot of help, guidance, and encouragement from people around me. I would like to firstly give my great thanks to my doctoral dissertation advisor: Dr. Yang-Tse Cheng, who provided his continuous support to help me overcome various barriers in my Ph.D. adventure. He has indeed provided abundant instruction as well as in-depth discussions and comments at every stage of my doctoral study. Secondly, but not less importantly, I would like to express my great gratitude to my co-advisor, Dr. Yue Qi, who has fully exemplified the high quality scholarship to which I aspire and pursue. She has provided constructive guidance and challenged my thinking to improve and shape my dissertation. In addition, I would like to especially thank Dr. Matthew J. Beck for his helpful and insightful discussions in my graduate study. Without their navigation, I would not be able to pin my flag at the top of this "mountain".

Next, I would like to thank Dr. Qinglin Zhang (now at General Motors), Dr. Xingcheng Xiao (at General Motors), and Dr. Juchuan Li (now at Apple Inc.) for their cooperative experimental work. I also wish to thank my research committee members: Dr. T. John Balk, Dr. Jonathan F. Wenk, and Dr. Gang Cao. Their suggestions and discussions are very important building bricks to concrete my doctoral dissertation. In addition, I would like to thank my lab mates: Dr. Rutooj D. Deshpande, Dr. Ilona Hoffmann, Jiagang Xu, Tao Chen, Bo Lu, Alshroofy Mohanad, Baleegh Alobaid, Yikai Wang, Long Zhang, Jiazhi Hu, for their support and help on my research.

Life is a love. I greatly appreciate my parents for their long-lasting supports and

encouragements over the past 29 years, which led and motivated me to obtain this doctoral degree.

Life is a promise. I would like to greatly thank Dr. Yong Wan, who has a strong background in physics and mathematics, for the helpful scientific discussions in my research and continuous support in my personal life.

Life is a gift. I own significant gratitude to my dear and precious friends: Xu Zhang, Lei Han, Peizhen Li, Jue Wang, Xiaojin Wang, Teng Huang, Wei Wan, Zhi Zhang, Yunchao Li, Miluo Zhang, Yan Jin, Zeren Xu, and Lukas Rossel, who made my life more colorful during my graduate study.

TABLE OF CONTENTS

LIST OF FIGURES

LIST OF TABLES

Chapter 1 Background and motivations

1.1 Silicon electrode and its solid electrolyte interphase

There are increasing demands on the performance electrochemical storage systems, since it is widely agreed that we should in the future rely more on renewable energy sources rather than burning fossil fuels. This is based on two main concerns: the natural source of fossil oil and charcoal, is limited; the second is the environmental concerns about the CO_2 emission causing global warming and pollution from incomplete combustion, e.g., CO and formaldehyde. However, most sustainable energy sources, such as solar, tidal and wind energy, are not stable all the time which foster the requirements of developing electrochemical storage device that can absorb and release power efficiently. Especially in the civil transportation industries, high capacity and efficiency energy storage systems are required for electric vehicles (EVs). In the past, the fuel cell seemed to be a good candidate with high energy density, but the operation and hydrogen storage problems impede its practical operation.[3] Alternatively, the lithium ion batteries (Li-ion Batteries or LIBs) would be one of the most promising candidates in the near future.

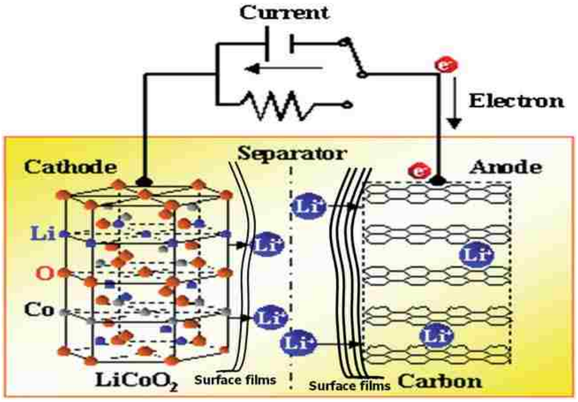

Figure 1.1: A schematic picture about the $LiCoO_2$−Graphite battery system.(Adapted from reference [1]. Copyright © The Royal Society of Chemistry 2011)

Figure 1.1 illustrates the commercial Li-ion battery system at present for most portable electronic devices, e.g., laptop, cellphone, in which the cathode material is $LiCoO_2$ and the anode material is graphite. The charging and discharging are driven by the Li ion transportation lithiating or delithiating with the electrodes. The separator between cathode and anode should be an ionic conductor and electronic insulator, which can prevent direct red-ox reaction between the electrodes. However, the low energy density, low power density and degradation problems of current battery systems impede the wide application in vehicles. Since the energy released during battery discharging[4] is

$$Energy = \int V \mathrm{d}q \tag{1.1}$$

where V is the voltage and q the amount of charge transferred, one of the alternatives to increase the energy storage is to increase the charge capacity in the battery. In recent years, Silicon (Si)[5] has received much interest as a promising anode material for its high Li-storage capacity compared to graphite or tin (Figure 1.2), low discharge potential, and cost.[2,6] Unfortunately, these merits come with a range of problems: large volume expansion upon cycling ($\approx 300\%$), unstable solid electrolyte interphase (SEI) formation, and low Li diffusion coefficient during lithiation and delithiation, all of which induce severe degradation problems, capacity loss, and limited the rate and cycling performance of LIBs.[5,7–11]

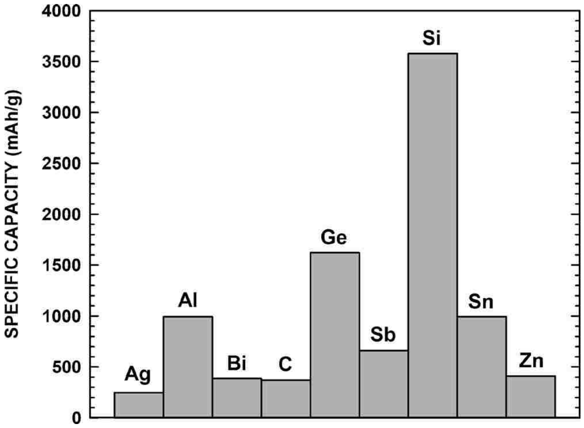

Figure 1.2: Specific capacities of different anode materials.(Adapted from reference [2]. Copyright © The Electrochemical Society 2007)

Recently, in order to make Si-based anodes commercially usable, research efforts have been devoted to improving the rate performance and capacity retention of Si electrode. The main efforts in the recent years have been focused on the following three aspects:

- Nanostructured Si systems (nanowire[12–15], nanotube[16,17], nanoparticle[18], patterned nanostructure[19]) were built with the idea that they could provide the structural buffer space to accommodate expansion and fast Li diffusion paths. Nam *et al.*[19] reported the improvement cycling performance by different nanopatterned Si electrode. Cui's group[13] in Stanford University found the Si nanowire anode based LIBs can sustain the large volume change during cycling, preventing electrode from pulverization and losing in electronic conduction. Their Si electrode maintained the 75% of the theoretical capacity when discharging. Unfortunately, the large surface-to-volume ratio caused the electrode exposed significantly to the electrolyte, which induced another problem: increasing Solid Electrolyte Interphase (SEI) formation on the electrode surface. SEI is formed due to the red-ox reaction of the components in electrolytes with Si on the surface of electrode and can prevent further side reaction, like in graphite, if it is stable. The SEI formed on Si electrode cannot sustain the 300% volume expansion, and, the electrolyte degrades the electrodes and causes capacity loss and low current efficiency.

- Making composite material (Graphite/Silicon[20], TiO_2/Silicon[21] composites) electrodes in “composite” microstructures was another avenue that has been focused on to put Si into commercial use. The idea of immersing nano-Si particles into graphite or TiO_2 matrix was that the graphite around the Si can buffer the volume change and increase the kinetics of Li ion transport in electrochemical cycles. Lee *et al.*[20] made spherical silicon/graphite/carbon composites anodes and showed around 700 mAh/g can be delivered with almost 100% coulomb efficiency within the first 50 cycles. Gallium was proposed as a “self-healing” electrode[22] for its solid-liquid transition during lithiation and delithiation. However, due to the low diffusion coefficient of Li ion in the Si electrode, one question was which part in the composites would Li ion prefer to insert into. The capacity would be significantly reduced if Li ion goes into the less-active part rather than Si.

- Surface modification, also known as artificial SEIs, has also recently been shown to be a promising method that can mitigate both the chemical and mechanical degradation in cathodes ($LiCoO_2$[23]) and anodes (graphite[23], Si[24–26]). Cui’s group demonstrated the effect of naturally formed oxides on Si nanowire surface and showed the suppress effect on Si volume expansion within 50 nm diameter enhanced the durability of Si electrode[25]. In addition, their Si nanotube with ion-conductive oxides outside layer can be cycled up to 6000 times with 85% of the initial capacity[24]. Xiao *et al.*[26] adopted a film structure of Si to study the effects of Al_2O_3 coatings which showed a formation of stable interfacial layer with a high Li ion permeability. Since Al_2O_3 is relatively stiff, it can constrain the volume expansion and mitigate the mechanical degradation[26]. Electrolyte additives such as Fluoroethylene Carbonate (FEC)[27] was used as a surface modification method and one of its advantages was lower in cost than that for chemical vapor deposition method, such as Atomic Layer Deposition (ALD) coatings. Etacheri *et al.*[27] studied the effect of FEC as a co-solvent on the performance of Si nanowire electrodes. They proved that the reduced irreversible capacity loss was due to the FEC induced thinner and compact film formation on the surface. However, these concepts are all far from commercial use, which motivate us to seek alternative coating materials or electrolyte additives with appropriate film thickness, Si particle size and geometry. As a result, an integrated experimental and computational model is required in order to design an optimized coating.

1.2 Motivations and overview of this thesis

The goal of this thesis is to design Si electrodes with high current efficiency and durability through fundamental understanding of the ionic and electronic conduction in Si and its SEI. In general, ionic conduction determines the rate performance of the electrode, while the electron leakage through the SEI causes electrolyte decomposition and, thus, causes capacity loss. Multi-scale physical and chemical processes occur in the electrode during charging and discharging. This thesis, thus, focuses on multi-scale modeling, including developing new methods, to help understand these coupled physical and chemical processes. Chapter 2 introduces a brief overview of the computational tools and methods. Chapter 3 presents a new method based on *ab initio* molecular dynamics to study the effects of stress/strain on the Li ion transport in amorphous Si electrodes. However, the origin of ionic conduction in the inorganic components of SEI is different from that in the amorphous Si electrode. To tackle this problem, I developed a model separating the problem into two scales: 1) atomic scale: defect physics and transport in single SEI components with consideration of their environment; 2) mesoscopic scale: defect distribution near the interface of different components. In Chapter 4, we present a study of defect physics and its transport in an important SEI components: LiF. The defect profile in equilibrium with the contacted electrode is correlated to the ionic and electronic conduction through the single solid electrolyte coating. Based on the knowledge of defect chemistry in single SEI components, in Chapter 5, we present a further study of the influence of heterogeneous interfaces between different SEI components, such as, LiF and Li_2CO_3, to the defect distribution. Our results show that this defect redistribution near the interface plays a very important role to promote the ionic conduction but prevent electron leakage through the SEI. In order to utilize this synergetic effect and optimize the electrical conduction through the SEI, in Chapter 6, we propose a SEI structure with two components that can maximize the ionic conduction and minimize the electronic conduction. Based on this sturcture, the effect of grain size and volume ratio to the promotion of ionic conduction was also studied. Finally, Chapter 7 presents a summary of the research work and discusses some future research directions.

Chapter 2 Overview of the computational methods

2.1 Density Functional Theory

Quantum mechanics was one of the most important break-throughs in the twentieth century. Materials are composed of nuclei and electrons. The Born-Oppenheimer approximation (BO)[28] provides a simple mathematical way to treat nuclei and electrons separately by a separation of the energy surface as a function of nuclei positions and the electron movements. This treatment was based on the fact that the nuclei are always much heavier than electrons, meaning that electrons respond much more rapidly to the surroundings. As a result, we fix the atomic position and solve the equations describing the election motion for the ground state energy, which is, for simplification, the time-independent, non-relativistic Schrödinger equation

$$\left[-\frac{\hbar^2}{2m}\sum_{i=1}^{N}\nabla_i^2+\sum_{i=1}^{N}V(\mathbf{r}_i)+\sum_{i=1}^{N}\sum_{j<i}U(\mathbf{r}_i,\mathbf{r}_j)\right]\Psi=E\Psi \tag{2.1}$$

where m is the electron mass. The terms in the Hamiltonian are defined as, from the left to right, the kinetic energy of electrons, the interaction between electrons and nuclei, and the interaction energy between different electrons. The most challenging part in solving this equation is the electron self-interaction part $\sum_{i=1}^{N}\sum_{j<i}U(\mathbf{r}_i,\mathbf{r}_j)$. Among methods to address this, the Hartree-Fock Self-Consistent-Field method (HF-SCF)[28] provides a solution for Coulomb and exchange energy by application of central field approximation. However, it ignores the electron correlation (Configuration Interaction), since the states of electrons in the method are independent of each other. In the past, several methods, such as variational theory and perturbation theory (MP2, MP3), have been adopted for adding or addressing the correlation energy in configuration with exchange. The most computational efficient of these methods is widely accepted to be the density functional theory (DFT).

Density functional theory, firstly proposed by Kohn and Hohenberg[29] in 1964, is based on two key theorems:

- *The ground-state energy from Schrödinger's equation is a unique functional of the electron density*
$$n(\mathbf{r}) = 2\sum_i \psi_i^*(\mathbf{r})\psi_i(\mathbf{r}). \tag{2.2}$$
- *The electron density that minimizes the energy of the overall functional is the true electron density corresponding to the full solution of the Schrödinger equation.*

Based on this, Kohn and Sham showed that, rather than solving equation 2.1, it is equivalent to find the right electron density by solving a set of single electron equations (Kohn-Sham Equations)[29]

$$\left[-\frac{\hbar^2}{2m}\nabla^2 + V(\mathbf{r}) + V_H(\mathbf{r}) + V_{XC}(\mathbf{r})\right]\psi_i(\mathbf{r}) = \varepsilon_i\psi_i(\mathbf{r}) \tag{2.3}$$

the first and the second term are defined as the kinetic energy of electrons and the sum of electron-ion, electron-electron and ionic coulomb interaction energy. $V_H(\mathbf{r})$ (Hartree potential)[29]

$$V_H(\mathbf{r}) = e^2 \int \frac{n(\mathbf{r}')}{|\mathbf{r} - \mathbf{r}'|} \mathrm{d}^3 r' \tag{2.4}$$

defines the correction for the unphysical self coulomb interactions. The last part $V_{XC}(\mathbf{r})$ is the exchange-correlation (XC) contributions and is defined as a functional derivative[29] of XC energy

$$V_{XC}(\mathbf{r}) = \frac{\delta E_{XC}(\mathbf{r})}{\delta n(\mathbf{r})}. \tag{2.5}$$

However, the difficulties in having the exact E_{XC} force us to use some approximations, such as local density approximation (LDA), generalized gradient approximation (GGA).[29] Compared with LDA, GGA, such as Perdew-Burke-Ernzerhof (PBE) functional[30], contains the gradient of electron density and is one of the most popular functionals in DFT calculations.

Another important aspect in quantum chemistry simulation is the basis sets ($\psi_i = \sum_\alpha c_\alpha \varphi_\alpha$). There are two main categories of basis sets: 1) atomic orbital basis sets, such as hydrogen orbitals, based on the fact that molecules are assembles of slightly distorted atoms; 2) Plane wave basis sets with the principle that the nuclei are periodic perturbations to the free electrons

$$n_m(\mathbf{r}) = \frac{1}{\sqrt{\Omega}} \sum_{\mathbf{G}} c_m(\mathbf{G}) \exp(i\mathbf{G} \cdot \mathbf{r}) \tag{2.6}$$

where Ω is the normalization factor (volume of box), $\mathbf{G}$ is the reciprocal lattice vector and $\mathbf{r}$ is the real space position. Here it is proposed to use the plane-wave basis sets for three reasons: 1) The pseudopotentials (the ions in pseudopotential method are composed of non-valence electrons and nuclei) are currently available to enhance the efficiency of plain-wave calculations; 2) It is efficient in AIMD[29]; 3) The convergence could be guaranteed with increasing the size of plane-wave basis sets.

However, we cannot do a calculation with an infinite plain-wave basis sets, since $\mathbf{G}$ can be any integer values. We must truncate the basis sets. This is done by specifying a plane-wave cut-off energy (E_{cut}) in our simulation and the value is kept the same all through different calculations.

$$\frac{1}{2} \mid \mathbf{G} \mid^2 \leq E_{cut} \tag{2.7}$$

In addition, Equation 2.6 only contains the Γ-point plane-wave expansion. Bloch theorem[31] stated that the eigenfunction for a periodic potential would be a plane wave times a function with cyrstal periodicity $u_{\mathbf{k}}(\mathbf{r})$. As a result, our wavefunction would be

$$\psi_{\mathbf{k},m}(\mathbf{r}) = \exp(i\mathbf{k} \cdot \mathbf{r}) n_{\mathbf{k},m}(\mathbf{r}) = \frac{1}{\sqrt{\Omega}} \sum_{\mathbf{G}} c_{\mathbf{k},m}(\mathbf{G}) \exp[i(\mathbf{G} + \mathbf{k}) \cdot \mathbf{r}] \tag{2.8}$$

where $\mathbf{k}$ would be any allowed wave-vectors in the primitive cell of the reciprocal space. Monkhorst and Pack[32] have shown that integrating sets of special points in the Brillouin Zone could provide an accurate result of the periodic functions of wave vectors. As a result, in our simulation, rather than integrating all the possible k-points for the plain-wave functions in the first Brilouin Zone, we will carefully select some representative points (KPOINTS) to maintain high computational efficiency.

2.2 Molecular Dynamics

Molecular Dynamics Simulation (MD) provides an extension to static methods to solve many-body problems numerically. It not only allows us to compare the simulation results with experiments based on thermodynamics and statistical physics, but also can shed lights on the atomic or molecular motion based on Newtonian mechanics. An important ensemble in MD is canonical ensemble or NVT, constant number of particles, constant volume, constant temperature, which mimics some real experimental settings. A thermostat is required in order to control the simulation temperature. One of the most popular thermostat for realizing NVT-MD is the Nosé -Hoover thermostat[29,33] by extending the Lagrangian for microcanonical ensemble to

$$L = \frac{1}{2}\sum_{i=1}^{3N} m_i s^2 v_i^2 - U(r_1, \ldots, r_{3N}) + \frac{Q}{2}(\frac{\mathrm{d}s}{\mathrm{d}t})^2 - gk_BT\ln s \tag{2.9}$$

where if $s(t) \equiv 1$, it returns to NVE lagrangian. The Newtonian equations, used to update the system, can be derived by

$$\frac{\mathrm{d}}{\mathrm{d}t}(\frac{\partial L}{\partial v_i}) = \frac{\partial L}{\partial r_i}. \tag{2.10}$$

The temperature in the MD simulation is then controlled by a "friction" term ξ through the following Newtonian equations

$$\begin{aligned} \frac{\mathrm{d}v_i}{\mathrm{d}t} &= -\frac{1}{m_i}\frac{\partial U(r_1, \ldots, r_{3N})}{\partial r_i} - \frac{\xi}{m_i}v_i, \\ \frac{\mathrm{d}\xi}{\mathrm{d}t} &= \frac{1}{Q}\left[\sum_{i=1}^{3N} m_i v_i^2 - 3Nk_BT\right] \end{aligned} \tag{2.11}$$

Ab initio Molecular Dynamics is a branch of MD simulation but the potential is defined by, rather than a force field which explicitly defines the atomic forces (e.g., harmonic potential approximation), quantum chemistry calculations (e.g., DFT). To make it clear, the Lagrangian in Equation 2.9 should be modified to

$$L = \frac{1}{2}\sum_{i=1}^{3N} m_i s^2 v_i^2 - E[\varphi(r_1, \ldots, r_{3N})] + \frac{Q}{2}(\frac{\mathrm{d}s}{\mathrm{d}t})^2 - gk_B T \ln s. \tag{2.12}$$

The simulation routine is mainly in such a sequential way: 1) calculate the ground state energy; 2) the positions of ions are updated according to the potential in one MD step based on Newtonian Mechanics; 3) then returns to the first step. In the past, this approach was time consuming, which impelled the development of Car-Parrinello Molecular Dynamics[29] (the basic idea is to simultaneously simulate the motion of nuclei and electrons by MD). However, in recent years, the Born-Oppenheimer Molecular Dynamics (BOMD) has been more widely used.

Chapter 3 Lithium ion transport in high capacity anodes

3.1 Summary

Silicon, as a promising electrode material for high energy density lithium ion batteries, experiences large strains and stresses during lithiation and delithation. The coupling effect between stress and lithium diffusion leads to a grand challenge to optimizing the design of Si electrodes with high capacity and high rate capability, particularly considering the amorphization of Si at initial cycles. In this study, we established a relationship between stress and the diffusion coefficients of Li in amorphous Si by *ab initio* molecular dynamics calculations (AIMD). The prediction from AIMD was validated by the potentiostatic intermittent titration measurements. Our results showed that two Li diffusion mechanisms can operate depending on the stress state. Specifically, the stress can increase Li diffusion either through increasing free volume under tension or by changing local structure under compression. However, within the range of stress generated during the lithiation and delithation process, diffusion coefficients are expected to vary by only one order of magnitude.

This chapter is reproduced from the work published as: Jie Pan, Qinglin Zhang, Juchuan Li, Matthew J. Beck, Xingcheng Xiao, Yang-Tse Cheng, "Effects of Stress on Lithium Transport in Amorphous Silicon Electrodes for Lithium-ion Batteries," Nano Energy 13, 192-199 (2015). Copyright © Elsevier Ltd. 2015

3.2 Introduction

In recent years, silicon (Si) has received much interest as a promising negative electrode material for lithium ion batteries (LIBs) because of its high specific capacity, low discharge voltage, and low cost.[34–37] However, these merits come with a range of problems: large volume expansion upon cycling ($\sim 300\%$), cracking, and structural changes[38,39], leading to severe capacity degradation and short cycle life. Furthermore, lithium (Li) transport in Li_xSi electrodes is slow with a diffusion coefficient approximately between 10^{-10} and 10^{-14} cm^2s^{-1}[40–43]. The performance of LIBs at high charge/discharge rates (i.e., high current densities) critically depends on the Li transport properties in electrodes. To limit the impact of these challenges, nano-structured Si systems (e.g., nanowires[13–15,44,45], nanotubes[16,17], nanoparticles[18,46], and patterned nanostructures[19]) have been proposed to meet the demands for high performance batteries. In these electrode structures, improved rate-performance is made by reducing the effective diffusion distance that Li must travel. These improvements are achieved at the cost of (1) severe solid electrolyte interface (SEI) formation due to large surface area and (2) relatively low energy density. In order to design Si electrodes with required performance and durability, careful engineering is needed to balance the intrinsic properties of Si and nanostructuring. Thus, it is necessary, in the context of charge/discharge rate, to understand the detailed mechanism of Li diffusion in Si electrodes.

One the other hand, the coupling effect of lithium diffusion and its induced stress makes the understanding of lithium transport more difficult, since stress can impact Li diffusion and vice versa. Although several publications have reported Li diffusion coefficients in Si[40–43], the effect of stress on diffusion behavior has not been reported. Large stresses on the order of a few GPa[47,48] have been observed during lithiation and delithiation of Si. In most cases, Si electrodes are amorphous. Unfortunately, there is no universal rule which can describe the effects of hydrostatic stress on diffusion[49] in amorphous alloys. In some amorphous systems, the hydrostatic compressive stress would increase the diffusion coefficient (e.g., the viscosity decreased with pressure in $NaAlSi_2O_6$ melts[50], and enhanced interdiffusion in amorphous Si/Ge multilayers[51]), while in some other amorphous systems the effects of pressure on diffusion are absent (e.g., ^{57}Co diffusion in $Co_{81}Zr_{19}$[52]). In addition, it was found that a compressive stress could decrease the diffusion rates in some metallic glasses (e.g., ^{95}Zr diffusion in $Co_{92}Zr_8$[53]). The fact that Si experiences both compressive and tensile stresses during electrode cycling raised additional complexities. Therefore, it is necessary to study the detailed kinetics and structural changes under hydrostatic tension and compression in order to understand Li transport in amorphous Si.

In this chapter, we present a study integrating both calculations and experiments to investigate the effect of stress on Li diffusion in Si electrodes. Explicit *ab initio* molecular dynamics (AIMD) simulations based on density functional theory (DFT) were performed to study the changes in structure, diffusion rates, and transport mechanisms in stressed LiSi systems. Our calculations found that Li diffusion coefficients vary within one order of magnitude under the stresses encountered in Si electrodes, in agreement with experimental observations of Li diffusion coefficients in lithiated Si. The results of this work provide a better understanding at the atomic level of Li diffusion behavior in amorphous Si, which can also be helpful to the understanding of diffusion in other similar inorganic amorphous systems.

3.3 Methodology

3.3.1 Computational details

Ab initio Molecular Dynamics simulations, which provide fundamental information about diffusion at the atomic scale, were performed using the Vienna *Ab initio* Simulation Package (VASP)[54,55]. The exchange and correlation function was approximated at the level of the generalized gradient approximation (GGA) in the Perdew-Burke-Ernzerhof (PBE) flavor[30]. In addition, the ionic cores were modeled with projector-augmented-wave (PAW) potentials[56]. The Brillouin zone was sampled at the Γ point, which represented about $3.3 \times 10^{-4}\text{Å}^{-3}$ k-points for the selected box size. The energy cutoff for the planewave expansion of the electronic eigenfunctions was 350 eV. These parameters were selected based on convergence tests of calculated total energy, and were comparable with the parameters used in previous calculations[6].

In the present calculations, we focus on amorphous LiSi (atomic ratio 1:1) composition as an example of a range of amorphous $\mathrm{Li}_x\mathrm{Si}$ materials relevant to Si based LIB electrodes. Amorphous LiSi alloy structures were prepared by AIMD within VASP[54,55]. The systems were first created as crystals, typically containing 192 atoms (96 atoms for each species). These structures were then heated up to a temperature above the melting temperature[57] (e.g., 1700 K). At this temperature, systems were equilibrated for 8000 MD steps with a 0.5 fs time step. To obtain amorphous structures relevant at lower temperatures, the systems were then quenched to a temperature of interest to perform structural studies and diffusion calculations (e.g., 1200 K and 900 K) with a rapid cooling rate: 200 K per 2000 time steps (1000 fs), similar to the cooling rates used in previous calculations[6,58]. To prepare systems with different stresses at a specific temperature, we performed AIMD simulations at various volumes by adjusting the simulation box size from above to below the equilibrium volume of the stress-free state. A total of 2000 time steps (0.5 fs/step) was used to equilibrate the volume controlled system. The potential energy of each system converged to a stable value (the differences in potential energy were within 10^{-4} eV/atom) after 2000 time steps, signalling the end of the equilibration phase of the AIMD simulations at a given volume. After that, the potential energy of another 2000 time steps were averaged and the energy values of different volumes were fitted to a third order polynomial with respect to the box volume V (Figure 3.1).

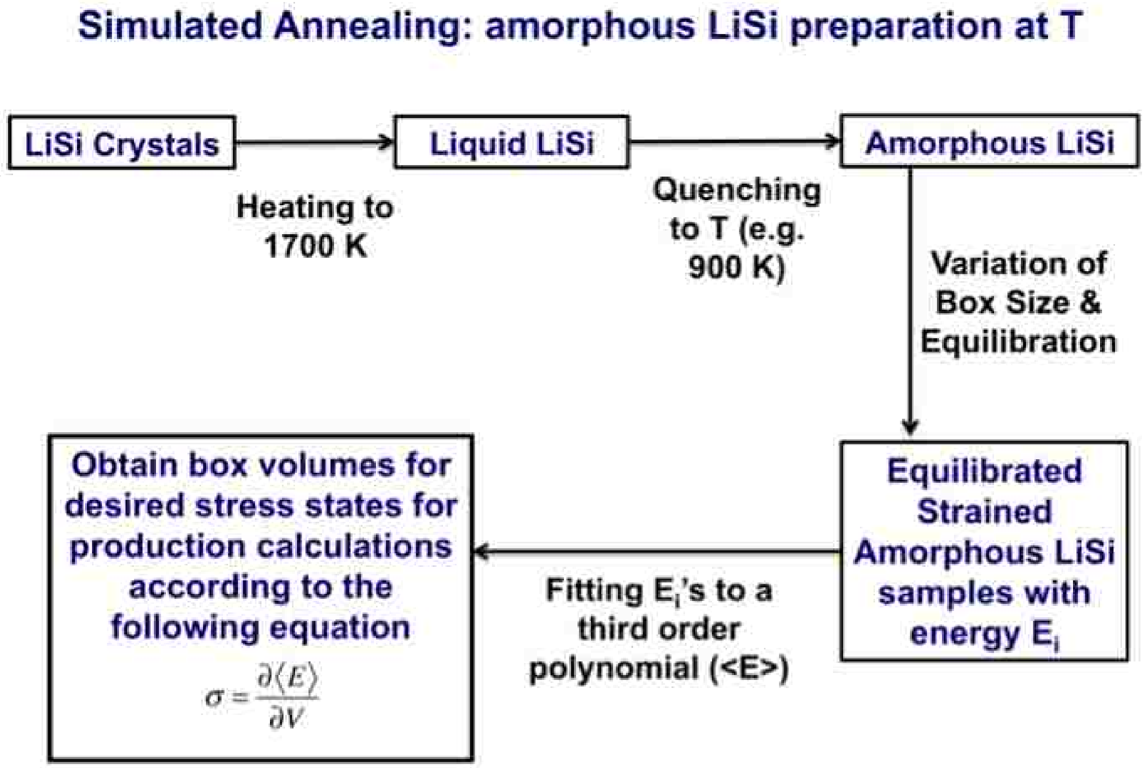

Figure 3.1: *Ab initio* molecular dynamics preparation of amorphous LiSi samples at temperature T.

The hydrostatic stress in the simulation box is determined as

$$\sigma_{T,N} = \left.\frac{\partial\langle E(V,T,N)\rangle}{\partial V}\right|_{T,N}, \tag{3.1}$$

where $\langle E(V,T,N)\rangle$ is the the equilibrated potential energy represented by the third order polynomial which is a function of the volume, V, of the simulation boxes, the temperature, T, and the number of atoms, N. The equilibrium volume (stress-free volume) at different temperatures correspond to the volume V_{equi} at which

$$\frac{\partial\langle E\rangle}{\partial V} = \frac{1}{3a_0^2}\frac{\partial\langle E\rangle}{\partial a_0} = 0, \tag{3.2}$$

where a_0 is the supercell lattice constant. The equilibrated simulation box volumes corresponding to each stress state of interest (e.g., 2, 1, -1, and -2 GPa) were calcu-

Table 3.1: The volume of stress free supercell at each temperature and the estimated bulk modulus.

Temperature (K)	$V_0(\mathring{A}^3)$	Bulk modulus (GPa)
1500	3199.47	16.01
1200	3135.17	18.29
1000	3133.22	24.51
900	3100.37	26.74

lated from Equation 3.1 and were used to construct amorphous LiSi (a-LiSi) boxes at various stress states (The volume of the stress free supercell and the bulk modulus of amorphous LiSi at each simulation temperature are listed in Table 3.1). These stressed boxes were equilibrated for 1000 time steps prior to characterization.

3.3.2 Experimental details

Diffusion coefficients of Li in amorphous Si were measured using a potentiostatic intermittent titration technique (PITT). The working electrodes were 100 nm thick Si films on Cu foils fabricated by E-beam evaporation, and the counter electrodes were pure Li metals. The electrolyte was 1 M $LiPF_6$ salt in 1:1 ratio of ethylene carbonate/dimethyl carbonate (EC/DMC). PITT experiments were conducted using a Bio-Logic potentiostat (VMP3) at room temperature. Potential steps of 5 mV were applied until the current was bellow 1 mA g^{-1}, equivalent to a rate of C/4200. Diffusion coefficients were obtained using the intercept of long times ($\tau \gg 1$)[59] and the interfacial kinetics were considered to be much faster compared with diffusion[40,60].

The stresses in the thin film was measured by the *in-situ* Multi-beam Optical Stress Sensor (MOSS) stress measurement method[61–63]. Thin film amorphous silicon samples of 100 nm were deposited by e-beam evaporation system on quartz-titanium substrates. Before depositing Si, a 200 nm thick titanium layer was deposited on the quartz as the current collector. In addition, the titanium improves the adhesion between amorphous silicon and the substrate. The custom-made cells were subjected to galvanostatic cycles (constant currents) against lithium metal between 1.5 V and 0.05 V with a rate of C/10. The back surface of the quartz wafer was visible through a quartz window on top of the sealed cell, which allowed the laser of the MOSS system to go through to monitor the bending of thin film electrodes. By monitoring the bending with MOSS, the curvature of substrate was obtained. Within the stress level, the quartz substrate deformed elastically. The bi-axil stress in the film was calculated from the curvature κ by Stoney equation[64]

$$\sigma_f = \frac{E_s h_s^2 \kappa}{6 h_f (1-\nu_s)}, \tag{3.3}$$

where E_s is the Young's modulus of substrate, h_s the substrate thickness, h_f is the film thickness, and v_s is the Poisson's ratio of substrate.

3.4 Results and discussion

The partial radial distribution function (RDF), namely the second order correlation function $g(\mathbf{r})$, describing the probability to find an atom in a shell at the distance r from a reference atom, provides a measure of how atoms are arranged in a material. In amorphous materials, it characterizes the short range order and allows structural comparisons among different systems. Partial RDFs were calculated by invoking the effective isotropy of amorphous structures as

$$g_{\beta-\alpha}(r) = \frac{1}{\langle\rho\rangle}\frac{\mathrm{d}n_\alpha(r, r+\mathrm{d}r)}{\mathrm{d}v(r+dr)} \simeq \frac{1}{\langle\rho\rangle}\frac{\mathrm{d}n_\alpha(r, r+\mathrm{d}r)}{4\pi r^2 dr}, \tag{3.4}$$

where $\langle\rho\rangle$ is the averaged particle density, $\mathrm{d}n_\alpha(r, r+\mathrm{d}r)$ is the number of particles of type α in the shell $(r, r+\mathrm{d}r)$ at distance r of a reference atom β, $\mathrm{d}v(r+dr)$ is the volume of the shell. Figure 3.3 shows the calculated partial RDFs, $g_{Li-Li}(r)$, $g_{Li-Si}(r)$ and $g_{Si-Si}(r)$ for stress-free LiSi at 1200 K. All partial RDFs were averaged over 5000 time steps in the MD trajectory. Figure 3.3 shows that Si is the nearest neighbor to both Li and Si. The Si-Si neighbor distance is 2.4 Å and it is slightly larger than the

Table 3.2: Comparison of bulk modulus of amorphous LiSi at room temperature with literature

	AIMD (this study)	Nanoindentation[70]	MD[6]
Bulk modulus (GPa)	35	37*	36

*:The bulk modulus is estimated from the Young's modulus by assuming Poisson's ratio (ν) is 0.3: $K = \frac{E}{3(1-2\nu)}$, where K is the bulk modulus and E is the Young's modulus.

value of 2.3 Å in the crystalline Si[65]. The nearest neighbors of Li are Si (around 2.6 Å) and the first peak of Li-Li pair is located at $r = 2.7$ Å. That Si is nearest to both Li and Si is because Li atoms repel each other, and Si-Si covalent bonds are still strong in amorphous Li-Si systems (Figure 3.2). Grid-based Bader Charge analysis[66–68] shows that the electronic state of Si varies from $[Ne]3s^2 3p^2$ in crystalline Si to $[Ne]3s^2 3p^3$ in the amorphous LiSi (a-LiSi), and Li atoms are positively charged. This factor explains the slight increment in the length of Si-Si bonds[6] and the preference by Li atoms to have Si as their nearest neighbors. Comparing with previous simulation data[6], the first and second peaks in all of our $g(r)$ agree with those in the latest time step (15 ps). Furthermore, the second $g_{Si-Si}(r)$ peak in our simulation is at 4.1 to 4.3 Å and it is supported by the experimental partial RDF data in the second cycle[69]. In addition, the extrapolated bulk modulus of our simulated LiSi amorphous structure is consistent with previous experimental and computational results (Table 3.2). Thus, our simulated structure is consistent with previous computational and experimental studies. In addition, comparing partial RDFs at 900 and 1200 K shows that the locations of the first peaks in the partial RDFs each shift to lower r values with the lower temperature but only by 1%. The order of the nearest neighbor peaks remains the same (from small to large separation: Si-Si, Si-Li, Li-Li).

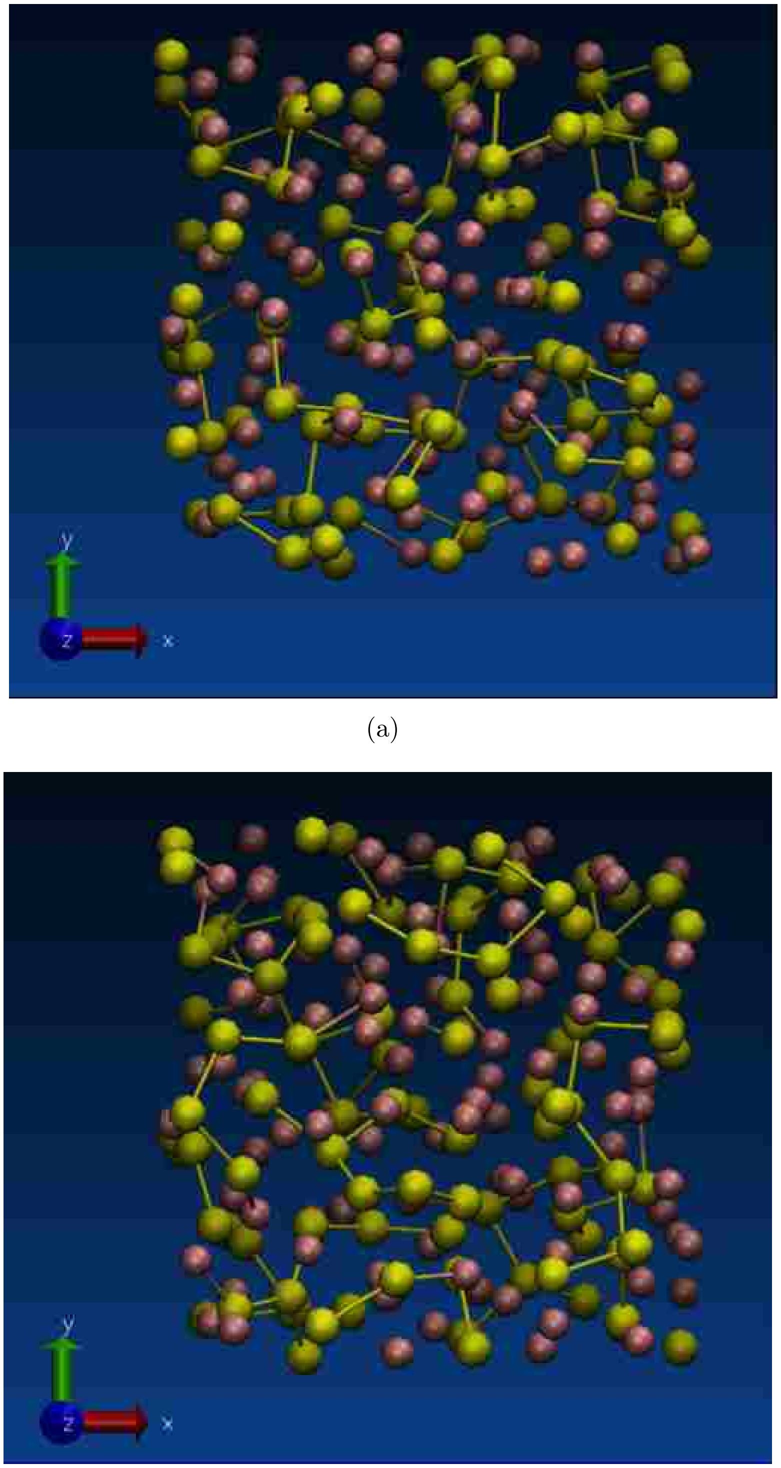

(a)

(b)

Figure 3.2: Snapshot of atomic structures at 900 K in MD simulations ((a): 2 GPa tensile stress was applied; (b): -2 GPa compressive stress was applied). Pink atoms: Li; yellow atoms: Si.

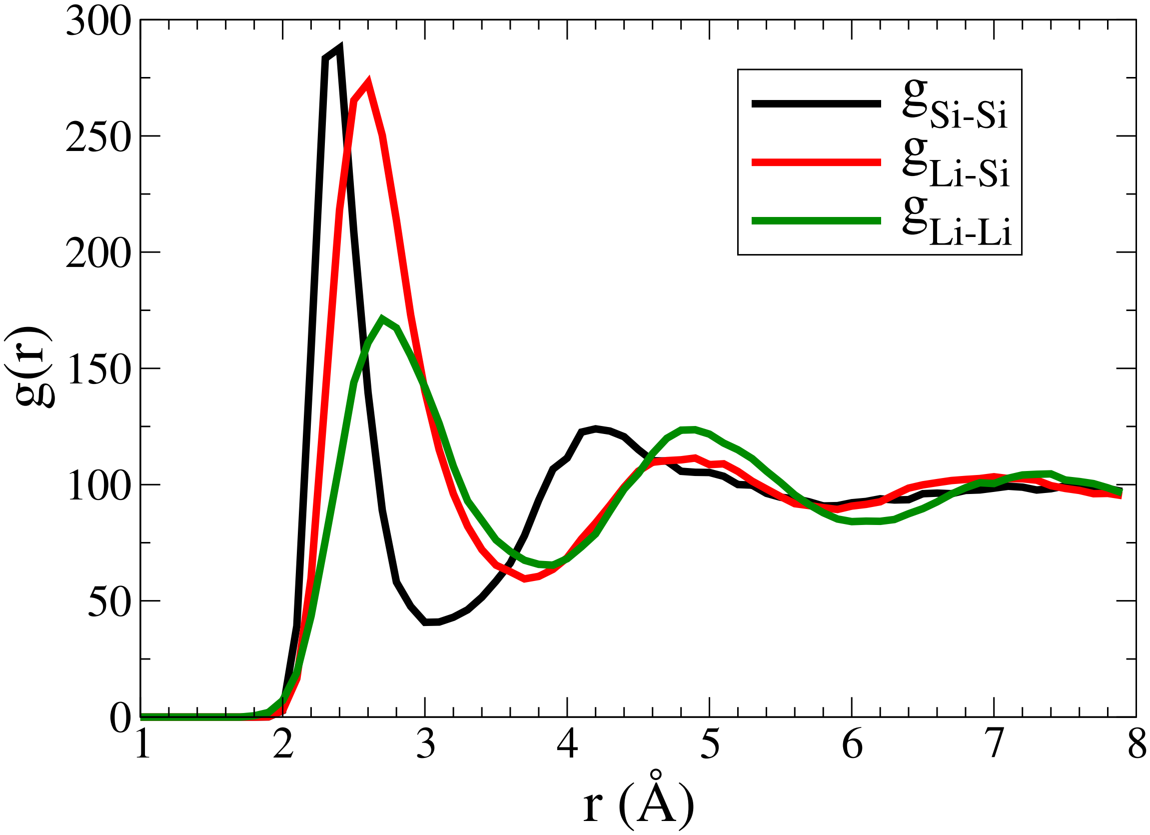

Figure 3.3: The Partial Radial Distribution Function of Si-Si, Li-Si, and Li-Li pairs in a-LiSi at 1200 K.

The diffusion coefficient can be estimated from the Mean Squared Displacement (MSD) of each atom type during a finte temperature MD[71]

$$\langle[\Delta R(t)]^2\rangle = \frac{1}{N}\sum_{i=1}^{N} |\overrightarrow{R_i}(t) - \overrightarrow{R_i}(0)|^2, \tag{3.5}$$

where $\langle \Delta R(t)^2\rangle$ is the MSD and $\overrightarrow{R_i}(t)$ are the atomic positions. The diffusion coefficients are then calculated using the Stokes-Einstein Relationship[6,71]

$$D_{Li} = \lim_{t\to\infty} \frac{\langle[\Delta R_{Li}(t)]^2\rangle}{6t}. \tag{3.6}$$

In this study, the diffusion coefficients of Li at room temperature in a-LiSi with different stress states were extrapolated from AIMD calculations at elevated temper-

Table 3.3: Effective diffusion barrier ΔG (eV) of Li in amorphous LiSi under different stress states.

	2 GPa	1 GPa	0 GPa	-1 GPa	-2 GPa
ΔG (eV)	0.32	0.35	0.37	0.37	0.32

atures (Figure 3.4) according to the Arrhenius Law

$$D_{Li}(T) = D_0 \exp(\frac{-\Delta G}{k_B T}), \tag{3.7}$$

where ΔG is the effective diffusion barrier (values of ΔG are listed in Table 3.3), k_B is Boltzmann constant and T is temperature. The extrapolated diffusion coefficients at 300 K (Figure 3.5(a)) shows that increasing the tensile stress leads to faster Li diffusion in a-LiSi. Compression, on the other hand, results in a relatively small change in diffusivity. At 300 K, the diffusion rate increases at -2 GPa compared with that at -1 GPa (compressive stress). In latter discussions, we will show that this phenomenon can be attributed to a local structural change that destablizes the Li in the cage formed by surrounding Li and Si atoms.

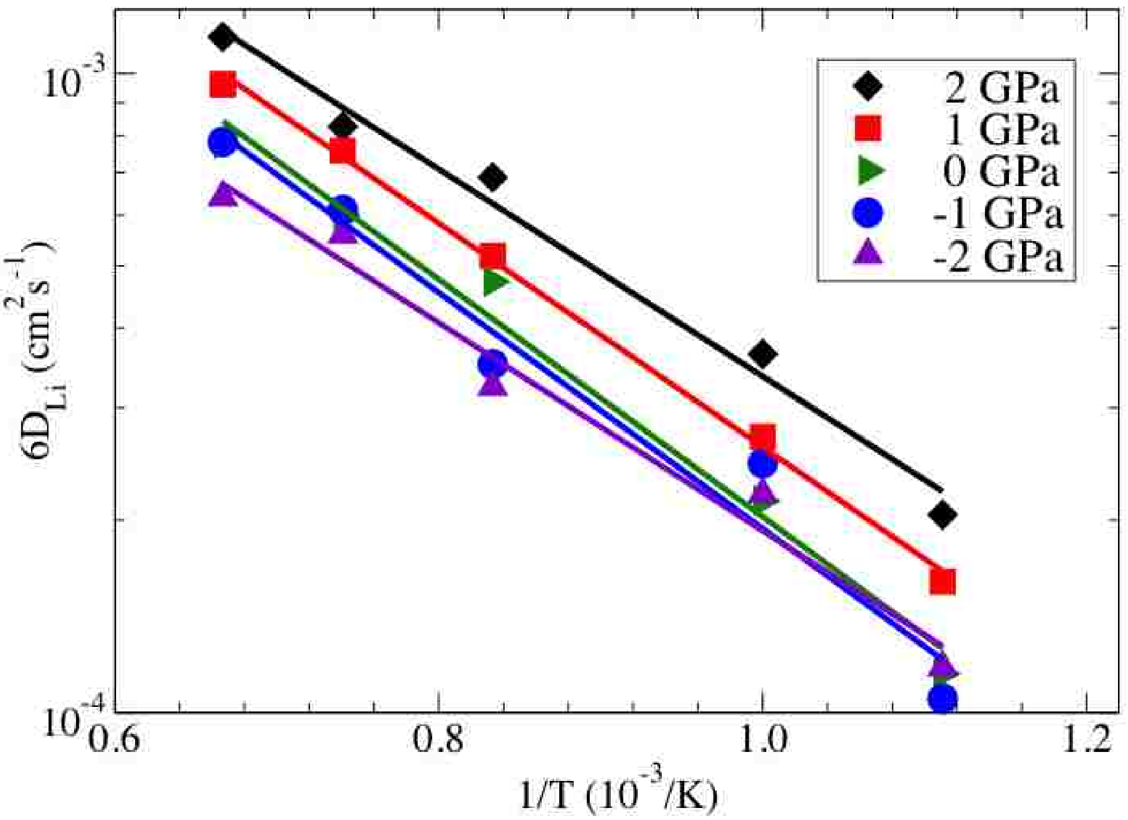

Figure 3.4: The extrapolation of diffusion coefficients at 300 K from high temperature simulations.

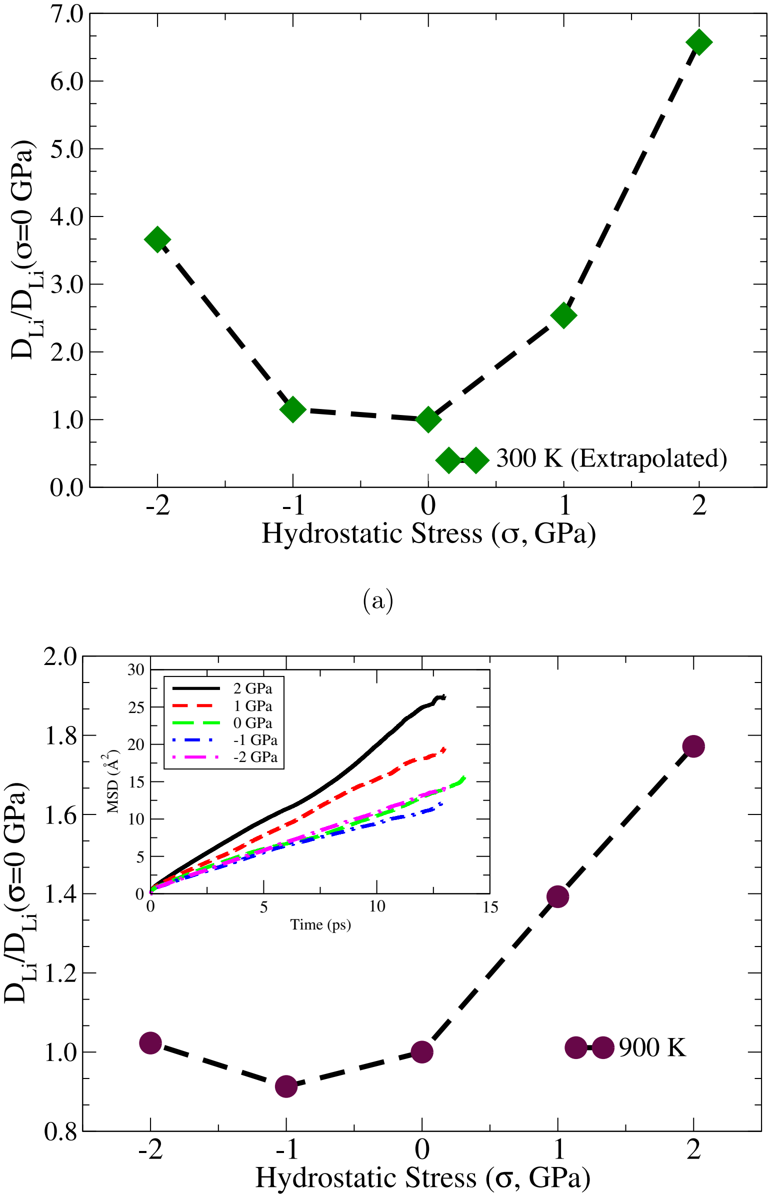

(a)

(b)

Figure 3.5: (a) The relative diffusion coefficients $(D_{Li}/D_{Li}(\sigma = 0GPa))$ as a function of stress at 300 K. (b) The relative diffusion coefficients $(D_{Li}/D_{Li}(\sigma = 0GPa))$ as a function of stress at 900 K. Insert: The MSD of Li in a-LiSi at 900 K, the lowest temperature in our simulation, with different hydrostatic (positive value means tensile stress and negative value means compressive stress) stress states.

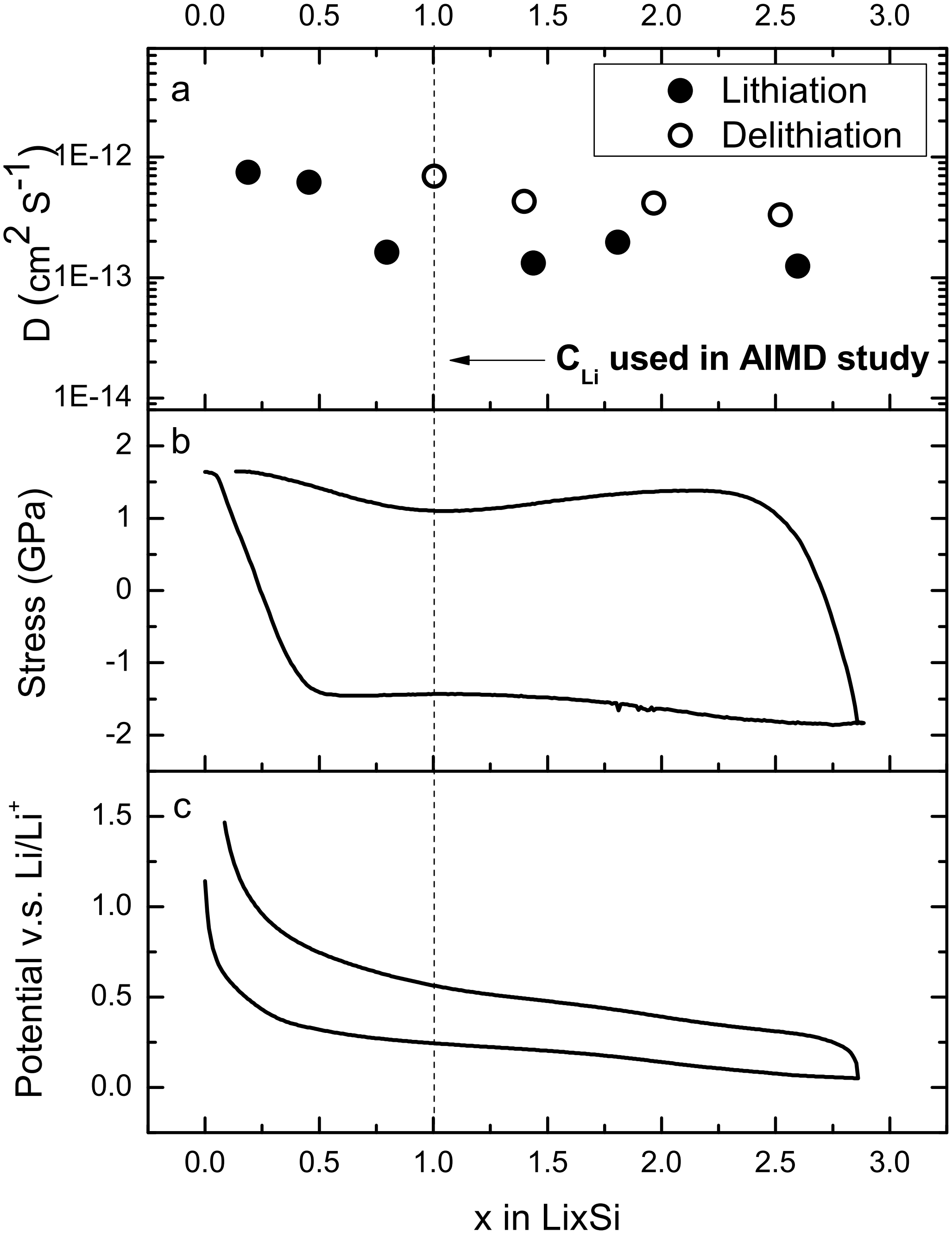

Figure 3.6: (a) Diffusion coefficients during lithiation and delithiation at different Li concentrations; (b) nominal stress calculated by Stony equation vs. x in $\mathrm{Li}_x\mathrm{Si}$ under charge/discharge rate of C/10. (c) cell voltage vs. x in $\mathrm{Li}_x\mathrm{Si}$ during stress measurement.

Experiments have shown that the stress during lithiation and delithiation of Si is several GPas[47,48]. Therefore, based on the above simulation results, the diffusion coefficients during lithiation and delithiation are expected to be similar, with diffusivity during delithiation (under tension) trending somewhat higher than that during lithiation (under compression). This expectation was verified using the the Potentiostatic Intermittent Titration Technique (PITT) measurements, which measured diffusivity at a constant Li concentration. To minimize other effects on Li diffusion, a thin film structure is selected in the PITT measurements. Thin film structure is chosen for this study, because 1) it takes shorter time to reach uniform composition; 2) cracking can be minimized[72]; 3) the complications from binders and conducting additives are avoided. Figure 3.6(a) compares the diffusion coefficients at the same state-of-charge in lithiation and delithiation. The results of *in-situ* stress measurements in the Si electrode accompanied by the potential profile is shown in Figure 3.6(b)-(c). The experimental results indicate that within the composition range investigated in this work, i.e., x between 0 and 2.7 in $\mathrm{Li}_x\mathrm{Si}$, the diffusion coefficients are within the same order of magnitude. The diffusion coefficients for Li under compression stress is slightly lower than those under tensile stress with the stress difference around 3 GPa. Thus, the variation of calculated diffusivity values at different stress states agree quantitatively with experimental results.

To better understand the effect of stress on diffusivity in a-LiSi, we examine the detailed structural changes induced by stress. We did this study from the atomic trajectories simulated at 900 K for the reasons that: 1) 900 K is below the melting temperature according to the Li-Si phase diagram[57]; 2) The trend of diffusion coefficients in response to the applied stress is the same as that at 300 K (Figure 3.5(b)). To study the structural change, we first considered stress-induced changes in the partial RDFs. If there were no changes in the short-range atomic ordering, we would expect the first peak of partial RDFs for each atomic pair to shift uniformly with a_0.

However, in LiSi the first peaks of Li-Li, Si-Li, and Si-Si RDFs shift asymmetrically in response to stress. Figure 3.7(a) shows the volumetric changes as a function of stress. By invoking the effective isotropy of amorphous materials under hydrostatic stress, the change in one dimension would be +2% under +2 GPa tensile stress and -1.6% under -2 GPa compressive stress compared with the stress free state. Figure 3.7(b) to 3.7(d) show the partial RDFs under different stress states. The covalent Si-Si bond is found to be the most rigid bond, with the location of the first Si-Si neighbor peak insensitive to stress (Figure 3.8). However, the Li-Li first neighbor peak shifts ±3% under respective ±2 GPa stress. In addition, the Si-Li first neighbor peaks shift ±1.5% under ±2 GPa stress, respectively. These different stress-induced changes in nearest neighbor spacings represent a change in the local environment, thus influencing the diffusion rates by altering the effective activation barrier. The different strength of pair interactions in a-LiSi (from strong to weak: Si-Si, Si-Li, and Li-Li) is the reason causing the change of the local environment with stress. In addition, we note that this observation provides an atomic level understanding of the elastic softening of LiSi relative to Si[58,73–75].

The coordination number (CN), describing the number of atoms located within a cut-off length (usually defined as a bond length) in amorphous materials, provides a quantitative measure of the change in a local atomic environment. Previous studies in other materials systems have shown that the CN can vary strongly due to an applied stress, causing, in some cases, changes in diffusivity[50,51,76]. To calculate CNs, a physically meaningful cut-off length must be defined for each atomic pair. To account for fluctuations in the amorphous LiSi system compared with crystalline LiSi, we choose cut-off lengths corresponding to 110% of the equivalent bond length in crystalline LiSi[77]: 2.65 Å for Si-Si, 3.0 Å for Li-Li, and 3.05 Å for Si-Li. The values of cut-off length are comparable with previous calculations in a-LiSi system[78]. The average CN for Si-Si (Figure 3.9(a)) is ~2.5 and varies between 4.5 and 5.2 for Si-Li in agreement

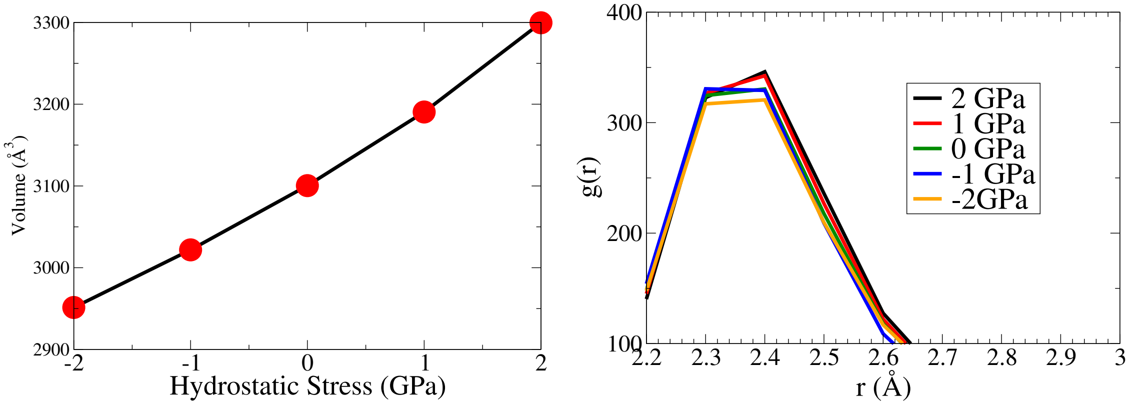

(a) Volumetric change due to stresses

(b) Si-Si pair

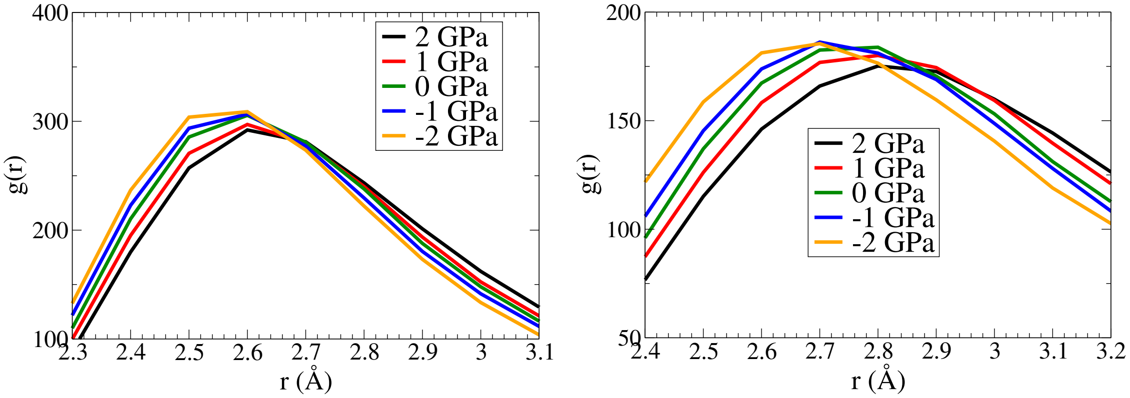

(c) Si-Li pair

(d) Li-Li pair

Figure 3.7: (a) The volume of the simulation boxes under hydrostatic stress at 900 K. (b)-(d) The change of the first peak in partial RDFs under different hydrostatic pressure states at 900 K.

with a previous study[78] on biaxially stressed amorphous LiSi. However, we note that changes in CNs as a function of hydrostatic stress are nonuniform for different atomic pairs (Figure 3.9(b)). The most significant change is in the Li-Li pair, where the CN increases by 1.0 as the stress changes from -2 GPa to 2 GPa. In addition, from the MD trajectories, the diffusion process of Li at low temperatures can be described as discrete movements: vibrating in a cage formed by its surrounding atoms then, after a while, it jumps from one cage to another (cage depicts the structure formed by surrounding Li and Si atoms, within which the target diffusive Li vibrates). As a result,

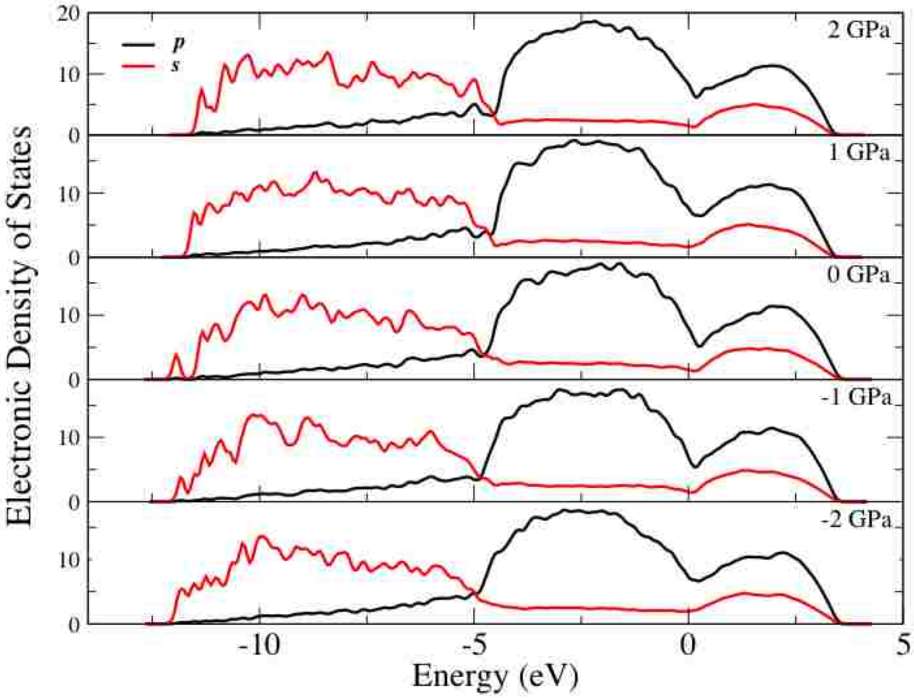

(a)

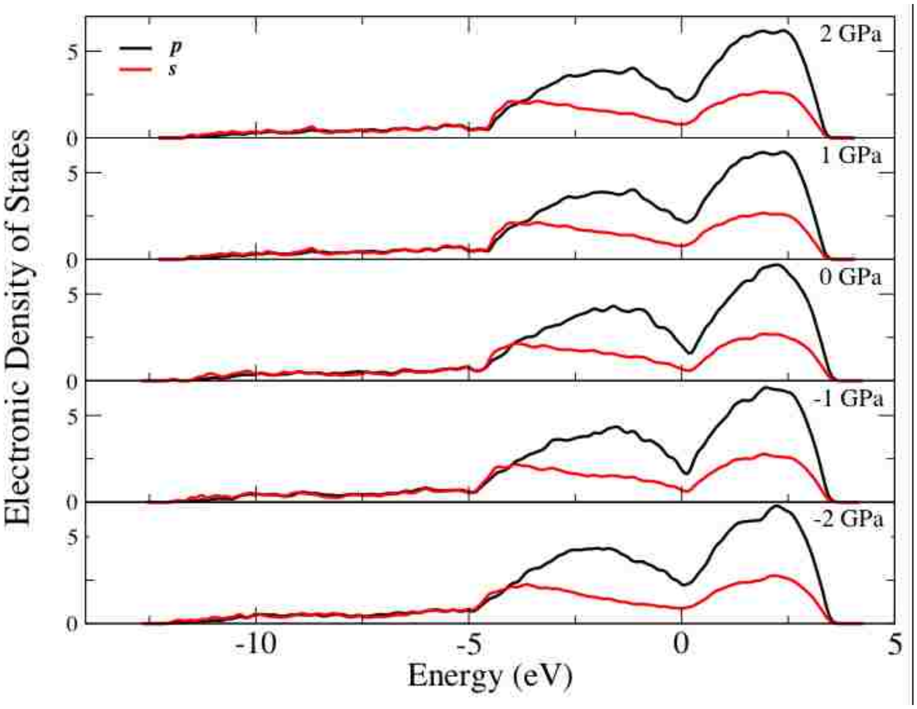

(b)

Figure 3.8: (a) Orbital projected density of states around Si atoms in amorphous LiSi under different stresses. (b) Orbital projected density of states around Li atoms in amorphous LiSi under different stresses. (0 eV in the plot corresponds to the Fermi energy of the system.)

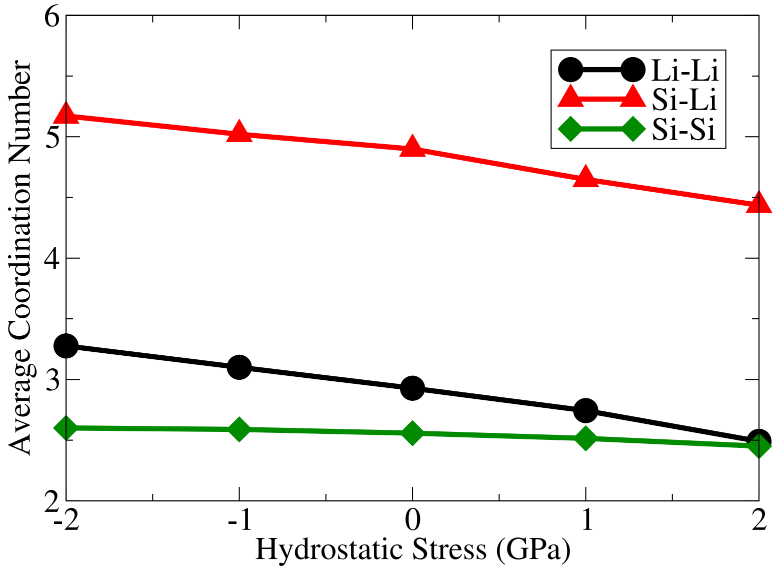

(a) Coordination number

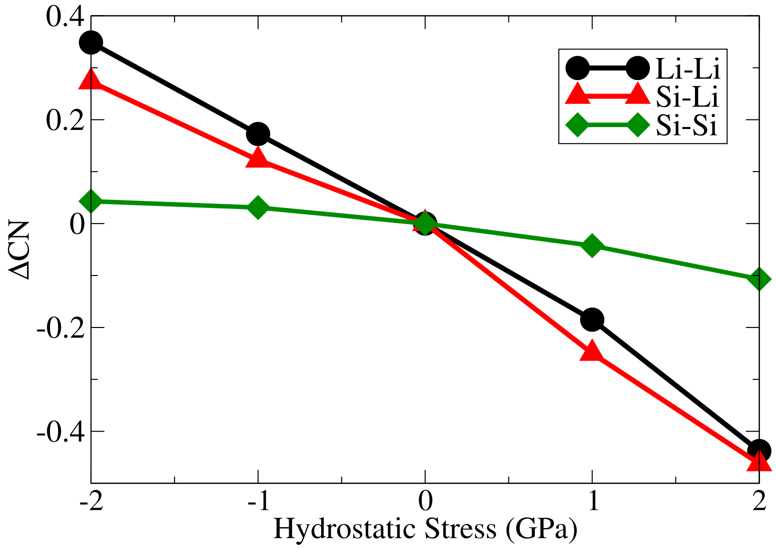

(b) ΔCN

Figure 3.9: (a) The coordination number as a function of stress at 900 K; (b) ΔCN with reference of CN at stress free state.

Li atoms are adjacent to significantly more Li atoms under compression. Since Li is positively charged in LiSi, this local structural change represents an destabilization of Li within cages which can facilitate the diffusion of Li.

Considering the change of diffusivity under tension, we note that the pressure dependence of diffusion can be characterized by an “activation volume” ΔV[49,51],

$$\Delta V = \left[-\frac{1}{RT} \frac{\partial \ln(D/D_0)}{\partial P} \right]_T , \tag{3.8}$$

where P is pressure (compressive stress is positive). For equilibrium systems, ΔV consists of two components[51]: ΔV_d, the volumetric change due to the formation of a defect and ΔV_m, the variation of volume when the diffusing atom moves from a normal site to a saddle point,

$$\Delta V = \Delta V_d + \Delta V_m. \tag{3.9}$$

From this perspective, stress influences diffusion by two related mechanisms. First, the tensile stress can increase diffusivity by increasing the available volume for defect formation, ΔV_d[49,79]. Second, for negative values of ΔV_m, a compressive stress can increase diffusion. A negative ΔV_m has been recognized in other Si or Ge containing systems[50,51,76]. Our results suggest that the activation volume for Li migration in LiSi is negative. As a result, tensile stress can increase diffusivity on the condition that $|\Delta V_d| > |\Delta V_m|$, and compression can increase diffusivity on the condition that $|\Delta V_m| > |\Delta V_d|$. The possible reason for $\Delta V_m < 0$ is the open covalent network structure in the system[51]. According to partial RDFs (Figure 3.7(c)), the nearest neighbors of Li are Si atoms under all stress states in the LiSi system. As a result, Li diffusion at low temperature in LiSi requires Li jumping through cages formed by the surrounding Si atoms. Since the rigid nature of the Si-Si bond, Li diffusion must be accompanied by Si-Si bond angle distortion to allow diffusive motion. This bond angle fluctuation can cause $\Delta V_m < 0$ as found in a previous study[51].

3.5 Conclusions

We combined computational and experimental methods to study stress effects on Li diffusion in Si electrodes. Based on atomic scale AIMD simulations, we found that the Li diffusion coefficient is not a monotonic function of stress ranging from tensile to compression. This occurs because the local atomic structure around Li changes under stress, causing changes in bonding between the diffusing Li and its neighboring atoms. Thus, the diffusion barrier can decrease with increasing compressive stress. As a result of the competition of free volume and local environment, the diffusion coefficients are expected to vary by one order of magnitude during lithiation and delithiation. This provides useful information for further optimizing the design of Si based nanostructure in order to control the Li diffusion and its induced stress/strain.

Chapter 4 Electrical conduction in solid electrolyte coatings on electrodes

4.1 Summary

Understanding the ionic conduction in solid electrolytes in contact with electrodes is vitally important to many applications, such as lithium ion batteries. The problem is complex because both the internal properties of the materials (e.g., electronic structure) and the characteristics of the externally contacting phases (e.g., voltage of the electrode) affect defect formation and transport. In this chapter, we developed a method based on Density Functional Theory to study the physics of defects in a solid electrolyte in equilibrium with an external environment. This method was then applied to predict the ionic conduction in lithium fluoride (LiF), in contact with different electrodes which serve as reservoirs with adjustable Li chemical potential (μ_{Li}) for defect formation. LiF was chosen because it is a major component in the solid electrolyte interphase (SEI) formed on lithium ion battery electrodes. Seventeen possible native defects with their relevant charge states in LiF were investigated to determine the dominant defect types on various electrodes. The diffusion barrier of dominant defects was calculated by the Climbed Nudged Elastic Band Method. The ionic conductivity was then obtained from the concentration and mobility of defects using the Nernst-Einstein relationship. Three regions for defect formation were identified as a function of μ_{Li}: 1) intrinsic, 2) transitional, and 3) p-type region. In the intrinsic region (high μ_{Li}, typical for LiF on the negative electrode), the main defects are Schottky pairs and in the p-type region (low μ_{Li}, typical for LiF on the positive electrode) are Li ion vacancies. The ionic conductivity is calculated to be approximately 10^{-31} Scm^{-1} when LiF is in contact with a negative electrode but it can increase to 10^{-12} Scm^{-1} on a positive electrode. This new insight suggests that divalent cation (e.g., Mg^{2+}) doping is necessary to improve Li ion transport through

the engineered LiF coating, especially for LiF on negative electrodes. Our results provide a new understanding of the influence of the environment on defect formation and demonstrate a linkage between defect concentration in a solid electrolyte and the voltage of the electrode.

This chapter is reproduced from the work published as: Jie Pan, Yang-Tse Cheng, Yue Qi, "General method to predict voltage-dependent ionic conduction in a solid electrolyte coating on electrodes," Physical Review B 91 (13), 134116 (2015). Copyright © American Physical Society 2015

4.2 Introduction

The origin of ionic conduction in solid electrolytes is defect formation and transport in ionic materials.[31,80–82] At a defined temperature, the internal equilibria of defects depend on two aspects: 1) the atomic structure of the defects; and 2) the electronic band structure of the material.[81,83,84] However, in reality, an ionic material of interest always operates in an environment (e.g., PbO in oxygen gas[81], Li ionic conductors coated on electrodes). In this situation, due to the formation of defects, the compound can deviate from the exact stoichiometric composition. As a result, the concentration of defects varies with the environment in which the ionic material is in a thermodynamic equilibrium.[81] For example, by increasing the partial oxygen pressure P_{O_2} (equivalently chemical potential of oxygen $\mu_{O_2} = \mu^{\circ}_{O_2} + RT\ln\frac{P_{O_2}}{P^{\circ}}$[81]) passing over PbO, the concentration of oxygen vacancies decreases while that of the oxygen interstitials increases as depicted in the Kröger-Vink or Brouwer Diagram.[81,83] Therefore, the environment can be treated as a "tuner" that can change the concentrations of defects in a material. In general, the environment is not only limited to the gas phase, but can be liquid or solid phase, such as electrodes on which the solid electrolyte is coated. Similarly, the concentrations of defects in the solid electrolyte would be electrode voltage dependent according to the Nernst equation ($V = -\frac{1}{z_i F}(\mu_M^{Cathode} - \mu_M^{Anode})$)[85]. The goal of this work is to develop a method to study defect physics and thus, ionic conduction in a material in contact with an external environment, e.g., a solid electrolyte on various electrodes for lithium ion batteries (LIBs).

Recently, solid electrolytes attracted a lot of research emphasizes not only because of the promising future of all-solid batteries[82,86–94], but also their importance as an interfacial layer between electrodes and liquid electrolytes, known as a solid electrolyte interphase (SEI)[95,96]. The performance of liquid electrolyte based LIBs relies on forming a stable SEI on the electrode surface.[95,96] In theory, an ideal SEI is expected to be ionic conducting[97–99], electrical insulating[100–102] and mechanically stable[103,104]. However, the characters of a natural SEI depend on many factors (e.g., property of electrode and electrolyte molecules) and a stable passivating layer is not always formed. For example, silicon (Si) electrode, one of the most promising negative electrodes with the highest theoretical capacity[105], cannot maintain a stable interphase[104] due to its large volume expansion[106–109]. This leads to a continuous capacity loss and degradation of the battery. Recently, surface coatings[110–113] and electrolyte additives[114] have been proposed as two promising ways to modify SEIs. In the first approach, surface coatings, such as Al_2O_3, TiO_2, and AlF_3, have been designed to serve as an artificial SEI to migrate electrochemical and mechanical degradation of the electrodes.[110–113,115,116] It was believed that solid electrolyte thin film coatings, also known as engineered artificial SEIs, were more stable than naturally formed SEIs in maintaining passivation, preventing continuous liquid electrolyte molecule decomposition, and protecting the electrodes from further degradation.[110–113] The second approach, by adding small amounts of electrolyte additives (e.g., Vinylene Carbonate[117,118], Fluoroethylene Carbonate[119–125]), the performance of the electrodes was improved with a longer cycling life. The additives have been shown to change the inorganic components in the SEI (e.g., increased formation of lithium fluoride).[119–125] The mechanisms responsible for the two promising approaches are not well understood. A theoretical approach is therefore needed to understand the mechanism of ionic and electronic conduction in SEI components.

A theoretical method to understand ionic conduction in a solid electrolyte shall include two parts: 1) the concentration of defects in the solid electrolyte in contact with electrodes and 2) the transport of the dominant defects (e.g., Li vacancy). The dependence of charged defect reactions on the chemical potential of electrons (i.e., Fermi energy) has been observed in various material systems.[126–129] More generally, Zhang[130] developed a first principles based method and demonstrated that defect concentration is a function of the chemical potential of atomic constituents. This formalism has been successfully applied to study multiple defect physics, e.g., defect compensation in ZnSe[131], zinc vacancies as the dominant intrinsic acceptor defects in ZnO[132], and nitrogen vacancies as the dominant intrinsic donor defects in *p*-type GaN[133]. In 2004, Van de Walle[134] published a comprehensive review article on this method and its applications to study defect physics in III-nitrides.

However, to benefit battery design, it is necessary to link defect reactions to an electrochemically measurable parameter, such as the open circuit voltage of the electrode. In this work, we extended this method[130–134] based on density functional theory to calculate the ionic conductivity in a solid electrolyte on electrodes. In our approach, electrodes are modeled as lithium (Li) reservoirs with a range of Li chemical potential values (μ_{Li}) and μ_{Li} can be related to the voltage of electrodes. Through this process, the Fermi energy dependent defect reactions in a solid electrolyte can be related to the voltage of neighboring electrodes. Shi[98] have taken a similar approach to investigate Li point defects in Li_2CO_3[98,99] as a function of the open-circuit voltage of electrode that Li_2CO_3 is coated on. In their work, Li interstitials, Li vacancies, and Li Frenkel pairs were considered as possible point defects, since carbon and oxygen were covalently bonded forming the oxocarbon anion CO_3^{2-}. In general, both cation and anion defects need to be considered in ionic materials, e.g., lithium fluoride (LiF). In addition, there remain other technical challenges in their method, such as the determination of the effective density of states at a finite temperature from density functional approximations and estimation of contribution of paired defects to ionic conduction.

In this study, our interest focuses on ionic conduction in LiF coated on various electrodes with rigorous considerations of the remaining technical challenges. LiF is one of the promising engineered SEI coating materials on the electrodes (e.g., Si) of LIBs, since the improved performance of electrodes has been linked to the increased concentration of LiF in the natural SEI.[119–125,135] In addition, perfect LiF crystals have a wide band gap[136–138], and can thus block the electron leakage to the electrolyte from the electrodes. In the present work, as a development of a general approach to evaluate all possible point defects, we studied ionic conductivity of a total of seventeen possible native defects with their relevant charge states in LiF on the surface of different electrodes. In addition, using this newly developed first principle based ionic defect calculation method, we demonstrate the dependence of defect formation and, accordingly, the ionic conduction as a function of the chemical potential of Li in the electrodes. Finally, the possibility of LiF as an engineered artificial SEI is discussed from the perspective of ionic and electrical conduction.

4.3 Theory and methodology

4.3.1 Thermodynamics of defects

In ionic crystals, typical types of defects include interstitials, vacancies, Frenkel pairs and Schottky pairs.[31,80,81] TABLE 4.1 summarizes possible defects with various charge states in LiF and their notations used in this study. In our model, defects are equilibrated with external Li reservoirs (known as external defect equilibria[81], in which deviation from the exact stoichiometric composition is allowed). As a result, the formation energy of a defect i with charge q is defined as[98,99,130–134]

$$\begin{aligned} E_f(i,q) =&[E_{tot}(i,q) - n_{Li}\mu_{Li} - n_F\mu_F \\ &+ q(\varepsilon_F + E_V + \Delta V)] - E_{tot}^{bulk}, \end{aligned} \tag{4.1}$$

where $E_{tot}(i,q)$ and E_{tot}^{bulk} are the calculated energies for the LiF supercell with and without one defect i. E_V ($E_V = 0$) is the valence band top of bulk LiF. ΔV is the electrostatic energy correction term to align the valence band maximum of the defected cells with that in the bulk LiF.[131,134] n_{Li} (n_F) is defined as the number of different Li (F) atoms compared with imperfect and perfect LiF supercells (e.g., for Li_i, $n_{Li} = 1$ and $n_F = 0$). μ_{Li} and μ_F are the chemical potential of Li and F in their reservoirs. In our calculation, μ_{Li} is a free parameter depending on the properties of coated electrodes; μ_F is approximated by assuming that LiF is the most stable compound for F to form

$$\mu_F = \mu_{LiF} - \mu_{Li}. \tag{4.2}$$

In addition, it is necessary to determine the bounds on μ_{Li} in Equation (4.1).[134] μ_{Li} depends on the electrodes on which LiF is coated, i.e., LiF coated on the anode or cathode. On the one hand, we consider that LiF is subjected to an upper bound when LiF is coated on Li metal: $\mu_{Li}^{max} = \mu_{Li}^{Metal} \approx -2.02$ eV. If we push μ_{Li} higher, Li metal would be deposited with F^- ion dissolved in electrolyte. On the other hand, the lower bound is considered when LiF is coated on the cathode: $\mu_{Li}^{min} = \mu_{LiF} - \mu_F^{F_2(gas)} \approx -9.71$ eV. Under this extreme condition, F_2 gas would be generated with Li^+ dissolved in the electrolyte. However, for battery applications, the typical μ_{Li} is higher than this limit (i.e., $\mu_{Li} \approx -6.6$ eV corresponding to about 4.6 volts against Li metal)[139]. As a result, we use $\mu_{Li} \approx -6.6$ eV as μ_{Li}^{min} in our study.

The Fermi energy (ε_F), which is an unknown parameter, is referenced to the valence band top in Equation (4.1). In perfect LiF, the Fermi level lies in the middle of the band gap; however, defects can create additional states in the band gap and vary the Fermi level. In our calculation, ε_F is determined by imposing the charge neutrality[98,99,130] by balancing free electrons($n_\ominus$), free holes($n_\oplus$), and charged defects

$$\sum_i q_i S(i,q) = n_\ominus - n_\oplus, \tag{4.3}$$

where $S(i,q)$ and q_i are the concentration and the associated charge of defect species, i, respectively. For pairs (e.g., Frenkel and Schottky pairs), there are energy penalties to separate the nearest-neighbor pairs (e.g., for SP, the pair with 2.52 Å farther away in distance has ~0.4 eV higher in formation energy). Therefore, only the nearest-neighbor Frenkel (Schottky) Pairs were included in charge balancing. At thermodynamic equilibrium, the concentration of defect i with formation energy $E_f(i,q)$ at a finite temperature T is

$$S(i,q) = N_s(i)\mathrm{e}^{-E_f(i,q)/k_BT}, \tag{4.4}$$

where $N_s(i)$ is the number of sites where defect i can be generated per unit volume. $n_\ominus$ ($n_\oplus$) are the concentration of electrons (holes) in the conduction (valence) band. At a given temperature, they are defined as

$$n_\ominus = \int_{E_C}^{\infty} d\varepsilon\, f(\varepsilon)D(\varepsilon), \tag{4.5a}$$

$$n_\oplus = \int_{-\infty}^{E_V} d\varepsilon\, (1 - f(\varepsilon))D(\varepsilon), \tag{4.5b}$$

where E_C (E_V) is the bottom (top) of the conduction (valence) band, $f(\varepsilon) = 1/(1 + \exp(\frac{\varepsilon-\varepsilon_F}{k_BT}))$ is the Fermi-Dirac distribution, and $D(\varepsilon)$ is the calculated electronic density of states. Since, for LiF, $\varepsilon - \varepsilon_F \gg k_BT$ (T is 300 K in our calculation), Equation (4.5) can be approximated by

$$n_\ominus = N_C\mathrm{e}^{-(E_C-\varepsilon_F)/k_BT}, \tag{4.6a}$$

$$n_\oplus = N_V\mathrm{e}^{-(\varepsilon_F-E_V)/k_BT}, \tag{4.6b}$$

where $N_C(N_V)$ is the effective density of states in the conduction (valence) band

$$\begin{aligned} N_C &= \int_{E_C}^{\infty} d\varepsilon\, \mathrm{e}^{-(\varepsilon - E_C)/k_B T} D(\varepsilon), && (4.7\text{a}) \\ N_V &= \int_{-\infty}^{E_V} d\varepsilon\, \mathrm{e}^{(\varepsilon - E_V)/k_B T} D(\varepsilon). && (4.7\text{b}) \end{aligned}$$

For materials with wide band gaps (e.g., alkali halides), only the energy levels near the bottom (top) of the conduction (valence) band can be occupied (unoccupied). Therefore, we approximate N_C (N_V) as

$$\begin{aligned} N_C &\approx \int_{E_C}^{E_C+\Delta} d\varepsilon\, D(\varepsilon), && (4.8\text{a}) \\ N_V &\approx \int_{E_V-\Delta}^{E_V} d\varepsilon\, D(\varepsilon), && (4.8\text{b}) \end{aligned}$$

where Δ is a small energy interval above the conduction band (below the valence band for N_V).

Table 4.1: Summary of Defects Types in LiF

Notation (i)	Kröger-Vink Notation[81,83,84]	Defect Types
Li_i	$Li_i^\times$	Li neutral interstitial
Li_i^+	$Li_i^\bullet$	Li positively charged interstitial
F_i	$F_i^\times$	F neutral interstitial
F_i^-	F_i'	Li negatively charged interstitial
V_{Li}	$V_{Li}^\times$	Li neutral vacancy
V_{Li}^-	V_{Li}'	Li negatively charged vacancy
V_F	$V_F^\times$	F neutral vacancy
V_F^+	$V_F^\bullet$	F positively charged vacancy
FP_{Li} [a]	$Li_i^\bullet + V_{Li}'$	Li Neutral Frenkel Pair
FP_{Li}^+ [a]	$Li_i^\bullet + V_{Li}^\times$	Li positively charged Frenkel Pair
FP_{Li}^- [a]	$Li_i^\times + V_{Li}'$	Li negatively charged Frenkel Pair
FP_F [a]	$F_i' + V_F^\bullet$	F Neutral Frenkel Pair
FP_F^+ [a]	$F_i^\times + V_F^\bullet$	F positively charged Frenkel Pair
FP_F^- [a]	$F_i' + V_F^\times$	F negatively charged Frenkel Pair
SP [a]	$V_{Li}' + V_F^\bullet$	Neutral Schottky Pair
SP^+ [a]	$V_{Li}^\times + V_F^\bullet$	Positively charged Schottky Pair
SP^- [a]	$V_{Li}' + V_F^\times$	Negatively charged Schottky Pair

[a]: The formation energies of paired defects (Frenkel pair and Schottky pair) are dependent on their distances of separation. For each type of pairs, the formation energies of the nearest, second nearest, and third nearest neighbor pairs were calculated and the one with the lowest formation energy was included in Equation (4.3). In addition, another scenario is the dilute pair (non-interacting) when two dilute point defects (e.g., V_{Li}^-, V_F^+) have the same formation energy.

4.3.2 Defect diffusion and ionic conduction

The ionic conductivity in ionic materials depends on both the formation and the diffusion of defects.[81] The flux density of a defect (i, q) under a concentration gradient and a potential gradient can be described as the sum of Fick's and Ohm's law[81]

$$\mathbf{j}(i, q) = -\frac{S(i, q)D(i, q)}{RT}(\nabla \ln S(i, q) + qF\nabla\phi), \tag{4.9}$$

where $D(i, q)$ is the diffusion coefficient of the defect (i, q), F is the Faraday constant, and ϕ is the electric potential. $D(i, q)$ can be calculated by Arrhenius equation at a finite temperature T[140]

$$\begin{aligned} D(i,q) &= gf\nu^*(\Delta x)^2\text{exp}(-E_m(i,q)/k_BT) \\ &\approx \frac{1}{2}\nu^*(\Delta x)^2\text{exp}(-E_m(i,q)/k_BT), \end{aligned} \tag{4.10}$$

where ν^* is the typical phonon frequency (e.g., $\nu^* \approx 10^{13}$ Hz along $[1\bar{1}0]$ direction[141]), Δx is the net travel distance in each hop, g is the geometric factor, f ($f = \frac{1+\sum_{j=1}^{z} Q_j\text{cos}\theta_j}{1-\sum_{j=1}^{z} Q_j\text{cos}\theta_j}$[142], where Q_j is the jumping possibility along angle θ_j) is the correlation factor, and $E_m(i,q)$ is diffusion barrier of the defect (i,q). For 1-D diffusion approximation (i.e., V_{Li}^- diffuses along $[1\bar{1}0]$ direction), $\sum_{j=1}^{z} Q_j\text{cos}\theta_j = \frac{1}{2}[\text{cos}(0)+\text{cos}(\pi)] = 0$ and $g = \frac{1}{2}$.

By assuming that the concentration of defects is spatially uniform, the flux density depends only on the applied potential gradient

$$\mathbf{j}(i,q) = -qF\frac{S(i,q)D(i,q)}{RT}\nabla\phi. \tag{4.11}$$

Multiplying qF to both sides of Equation (4.11), the flux density $\mathbf{j}(i,q)$ is converted to the current density

$$\mathbf{i}(i,q) = -q^2F^2\frac{S(i,q)D(i,q)}{RT}\nabla\phi. \tag{4.12}$$

From Equation (4.12), we can calculate the contribution of defect (i,q) to ionic conduction by

$$\sigma(i,q) = -\frac{\mathbf{i}(i,q)}{\nabla\phi} = q^2F^2\frac{S(i,q)D(i,q)}{RT}, \tag{4.13}$$

and the total ionic conduction is the sum of the contributions from main defects in the system

$$\sigma = \sum_i \sigma(i,q). \tag{4.14}$$

4.3.3 Computational details

In this study, the energies and electronic density of states were calculated by Density Functional Theory (DFT) with plane wave basis sets in the Vienna *ab initio*

Simulation Package (VASP).[54,55] The exchange-correlation functional was approximated by generalized gradient approximation (GGA) in the Perdew-Burke-Ernzerhof (PBE) flavor.[143] Projector-augmented-wave (PAW) potentials were used to mimic the ionic potentials.[144] The crystal LiF has sodium chloride face-centered cubic structure (space group: Fm$\bar{3}$m, No. 225[80,145]) and the structure was optimized with the total energy converged to 10^{-5} eV/supercell. A $3 \times 3 \times 3$ supercell was used in the optimization with a cut-off energy of 480 eV for the plane wave basis sets, a $3 \times 3 \times 3$ Monkhorst-Pack k-point mesh, and Fermi-smearing with 0.05 eV width. The lattice constant of LiF after the optimization is 4.07 Å and the error is within 1.3% compared with experimental results.[146]

The ground state energy $E_{tot}(i,q)$ of defect i with charge q and E_{tot}^{bulk} of the perfect LiF cell were calculated in the VASP-optimized $3 \times 3 \times 3$ LiF supercell which is large enough to satisfy the dilute defect condition. To account for interactions from image defects or charges, we studied the scaling behavior of $\Delta E = E_{tot}(i,q) - E_{tot}^{bulk}$ of three representative cases: Li_i (zero charge), V_{Li}^- (one negative charge), and V_F^+ (one positive charge). The local structure of the same point defect of $3 \times 3 \times 3$ LiF supercell was identical to that in $4 \times 4 \times 4$ supercell calculation and the difference in ΔE was less than 2%. The charged defects were modeled by adding (for negatively charged defects) or subtracting (for positively charged defects) one background electron to/from the total valence electrons in the supercell. In this study, the electrostatic energy correction ($\Delta V \approx 0.03$ eV) was obtained from the average electrostatic energy difference between the defected cell (e.g., V_{Li}^-) and the perfect cell[131,147,148]. (We noted that there are other methods to estimate ΔV, e.g., by inspecting the electrostatic potential far away from the charged defect[134]. The values of ΔV obtained from different methods are within the same orders of magnitude (10^{-2} eV) and the choice of ΔV does not change the magnitude of defect concentrations. In addition, a similar magnitude of ΔV has been observed in the literature[147] for other ionic materials.) A neutralization Jellium background charge was assumed by VASP to improve the energy convergence with respect to the supercell size.[149–151] The diffusion barriers $E_m(i, q)$ of dominant defects were calculated by Climbed Nudged Elastic Band Method (CI-NEB)[152,153] implemented within VASP.

4.4 Results and discussion

4.4.1 Formation of defects in LiF

The formation of defects depends on the properties of the specific material (e.g., band structure), the defects (e.g., defect structure and charge states), and the reservoir (e.g., μ_{Li}). Figure 4.2 shows the formation energy (E_f) of several defects with low formation energies as a function of chemical potential μ_{Li} of the Li reservoir. Three constraints are important to be considered in the defect formation in nearly stoichiometric compounds: 1) charge neutrality, which is imposed by Equation (4.3), 2) mass conservation, and 3) fixed proportion of cation (Li^+) and anion (F^-) lattice sites, regardless of their occupancy.[84] In our calculations, the charge neutrality is assumed to be satisfied by bounded charge on defects, free electrons, and free holes. At a high μ_{Li}, V_{Li}^- and V_F^+ are formed with similar formation energies. Since V_{Li}^- and V_F^+ carry the same amount but opposite charges, the charge neutrality is satisfied by defects in this μ_{Li} range. The coexistence of V_{Li}^- and V_F^+ can be viewed as the creation of a dilute SP (the black arrow in Figure 4.2). The magenta line (marked as *SP[Dilute]*) denotes the formation energy of a dilute SP when $\mu_{Li} > -5.5$ eV. In addition, in this μ_{Li} region, it can be noticed that the nearest-neighbor SP (green solid line in Figure 4.2) has a lower formation energy than the dilute SP. However, when μ_{Li} is decreased, especially below -5.5 eV, the formation energy of V_F^+ is further increased and V_{Li}^- formation energy decreased. In this μ_{Li} range, the concentrations of V_{Li}^- and V_F^+ diverge significantly. In order to maintain the charge neutrality, holes are created. In this region, the Fermi level is very close to the top of the valence band (Figure 4.1). As a result, holes can be generated by exciting electrons from the valence band to the defect levels[84,130,131,133]induced by Li vacancies near the Fermi energy. In addition, the mass is conserved between LiF and Li/F reservoirs (constraint 2) and the proportion of sites in the calculation system is fixed (constraint 3).

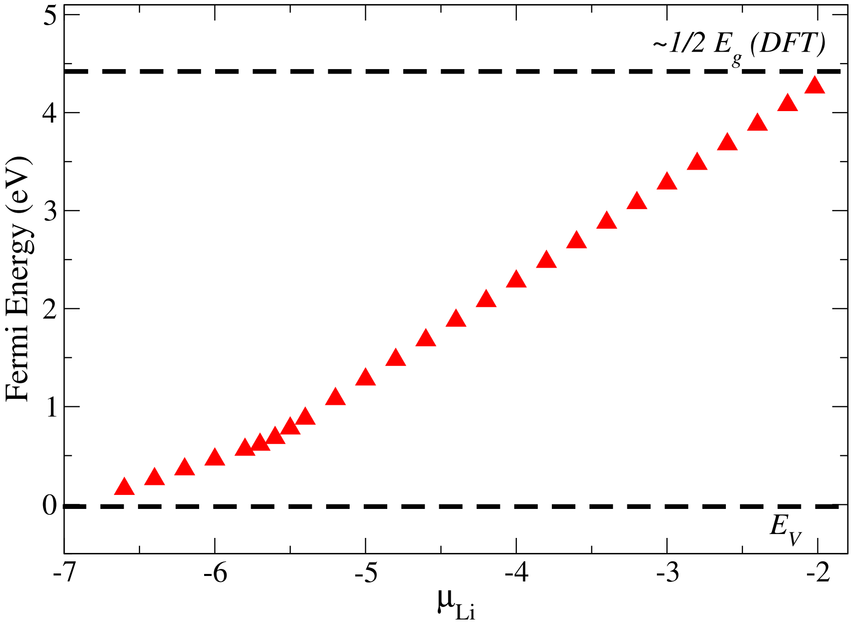

Figure 4.1: Fermi energy of LiF as a function of the chemical potential μ_{Li} in the reservoir.

In summary, there are two defect formation reactions in LiF depending on μ_{Li} of the Li reservoir:

1. LiF on high μ_{Li} reservoirs (e.g., Li metal), the main reaction is

$$\mathrm{Li_nF_n - Li_R - F_R \xrightleftharpoons{\Delta G_i(\delta r)} Li_{n-1}F_{n-1} + V_{Li}^- + V_F^+} \tag{4.15}$$

   where $\mathrm{Li_nF_n}$ is the perfect LiF crystal, $\mathrm{Li_R/F_R}$ refers to the Li(F) in the reservoir, and this reaction has a increasing activation energy $\Delta G_i(\delta r) = E_f(V_{Li}^-) + E_f(V_F^+)$ with increasing the separation (δr) of two vacancies;

2. LiF on low μ_{Li} reservoirs (e.g., $\mathrm{LiCoO_2}$), the main reaction is

$$\mathrm{Li_nF_n - Li_R \xrightleftharpoons{\Delta G_p} Li_{n-1}F_n + V_{Li}^- + \oplus} \tag{4.16}$$

   where $\oplus$ is a hole. This reaction has an activation energy $\Delta G_p = E_f(V_{Li}^-)$.

According to reactions (4.15) and (4.16), we define three defect formation regions depending on μ_{Li} of the reservoir (Figure 4.3) and the dominant defect concentration as a function of μ_{Li} of the reservoir is calculated for each region.

- **Intrinsic Region**: in this region, the hole concentration is at least 7-8 orders of magnitude lower than that of Schottky pairs. As a result, the defect formation can be approximated by the reaction (4.15) and the defect concentration can be estimated by $S(V_{Li}^-) = S(V_F^+) = N_s \mathrm{exp(-\Delta G_i(\delta r)/k_B T)}$, where, as discussed, $\Delta G_i(\delta r)$ depends on the distance of the pair items V_{Li}^- and V_F^+. In Figure 4.3, the left-triangle line (nearest-neighbor SP with the lowest ΔG_i) and right-triangle line (dilute SP with the highest ΔG_i) correspond to the two limits of the concentration of SP in this region, respectively. As a result, the majority ionic carriers in the intrinsic region are SPs (V_{Li}^- and V_F^+ pairs).

- ***p*-type Region**: the defect formation is dominated by reaction (4.16), forming mainly V_{Li}^- and the bounded charge is balanced by holes. The corresponding concentration of V_{Li}^- is calculated by $S(V_{Li}^-) = N_s \mathrm{exp(-\Delta G_p/k_B T)}$. As a result, the majority ionic carrier in this region is free V_{Li}^-.

- **Transitional Region**: defects are formed by both reactions (4.15) and (4.16). In this region, the concentrations of V_F^+ and V_{Li}^- start to diverge and the dominant defect type changes from SP(Intrinsic Region) to V_{Li}^- (*p*-type Region). The excess charge on V_{Li}^- which is not balanced by V_F^+ is balanced by holes. In order to calculate the defects concentration in this region, we use the charge balance concept by defining a portion p of V_{Li}^- whose charge is balanced by

V_F^+. By this definition, $1-p$ corresponds to the portion of V_{Li}^-, in which the localized negative charge was balanced by holes. The starting point of this region is chosen from the point of μ_{Li} that the concentration of holes is about 10 orders of magnitude less than that of dilute SP. This type of V_{Li}^- is depicted as up-triangle line in the transition region depicted in Figure 4.3. Therefore, p can be determined by

$$\frac{1-p}{p} = \frac{n_\oplus}{S_{SP}}. \tag{4.17}$$

4.4.2 Consideration of computational errors and comparison with experiments

Density Functional Theory with generalized gradient approximation (DFT-GGA) is known to have its own deficiencies which may lead to errors in the density of states in the conduction band and the value of band gap ($E_g = E_C - E_V$)[154]. In our calculations, several possible influences of the error were considered: 1) the value of N_C, 2) the value of ε_F, and 3) the underestimation of $E_f(i,q)$ of defects with the defects induced electronic states occupied (e.g., V_{Li}^-, Li_i, V_F)[155]. To minimize the influence of these errors, we did the following corrections and considerations: 1) N_C was corrected by the ratio of the effective mass of electrons ($m_\ominus^*$)[145] and holes ($m_\oplus^*$)[156] in LiF with the relationship $N_C/N_V = (m_\ominus^*/m_\oplus^*)^{3/2}$[31,80], 2) we tested the sensitivity of ε_F to the value of E_g by using the experimental value E_g^{exp}[136–138] and found that they were not sensitive to $E_g^{DFT-GGA}$ and E_g^{exp} ($E_g^{DFT-GGA} < E_g^{exp}$) in LiF. It is because that $E_g^{DFT-GGA}$ are high enough to prevent free electrons in the conduction band (Equation (4.3) and (4.6a)) in LiF, and 3) V_{Li}^- is formed by removing a Li^+ ion from a Li lattice site and the six-fold coordinated F^- remain as F^- ions. However, for V_{Li}, one of the nearest neighbor F^- ions becomes a neutral F atom. Because the excess electron in the V_{Li}^- system stays at the F-2p orbital (near valence band maximum), DFT-GGA can predict a reliable value of the formation energy of V_{Li}^-.[155]

In addition, for defects that can have their defect induced electronic states near the conduction band minimum (e.g., Li_i, V_F), their $S(i,q)$ are very low. We think that the errors that DFT-GGA can overestimate $S(i,q)$ would be insignificant. Therefore, we expected the influence of the errors in determining main defect types would be negligible.

Our results are consistent with experimental values.[157–159] The intrinsic defect formation energy (Reaction listed in (4.15)) was extrapolated from ionic conduction measurement of divalent ion (e.g., Mg^{2+}) doped LiF at elevated temperatures. A formation energy ΔG_{exp} was defined according to the mass action law[81,160]

$$\begin{aligned} S_{V_{Li}^-}S_{V_F^+} = S_{SP}^2 =& N_s(V_{Li}^-)N_s(V_F^+)\mathrm{e}^{-\Delta G_{exp}/k_BT} \\ =& N_s(V_{Li}^-)N_s(V_F^+)\mathrm{e}^{-2\Delta G_i/k_BT}. \end{aligned} \tag{4.18}$$

According to the definition of ΔG_{exp}, our results predict the theoretical two limits for ΔG_{exp}: 2.24 eV (nearest-neighbor SP) and 2.94 eV (dilute SP). The experimental value of ΔG_{exp} are $\sim$ 2.68 eV[157–159]with an individual V_{Li}^- formation energy $\Delta G_{V_{Li}^-} \sim$ 0.73 eV[161].

4.4.3 Diffusion barriers of dominant defects

4.4.3.1 Diffusion of dilute vacancies in LiF

We studied the diffusion barriers of the main defects in LiF (V_{Li}^- and V_F^+) through CI-NEB calculations[152,153]. Since V_{Li}^- and V_F^+ sites maintain the same symmetry, we constructed two diffusion pathways for each: through face-center (FC, along $[1\bar{1}0]$ direction) and through body-center (BC, along $[1\bar{1}\bar{1}]$ direction). For V_{Li}^-, after relaxation, the saddle point of the constructed BC path relaxed to a point between FC and BC (shown in Figure 4.4 inserted: Path 2). The diffusion barrier for V_{Li}^- is slightly smaller for path 2 ($\sim$ 0.57 eV) than that for path 1 (FC path, $\sim$ 0.60 eV), although path 2 has a larger travel distance than path 1. However, for V_F^+, two constructed pathways relaxed to the same saddle point (FC path) with a 0.69 eV diffusion barrier.

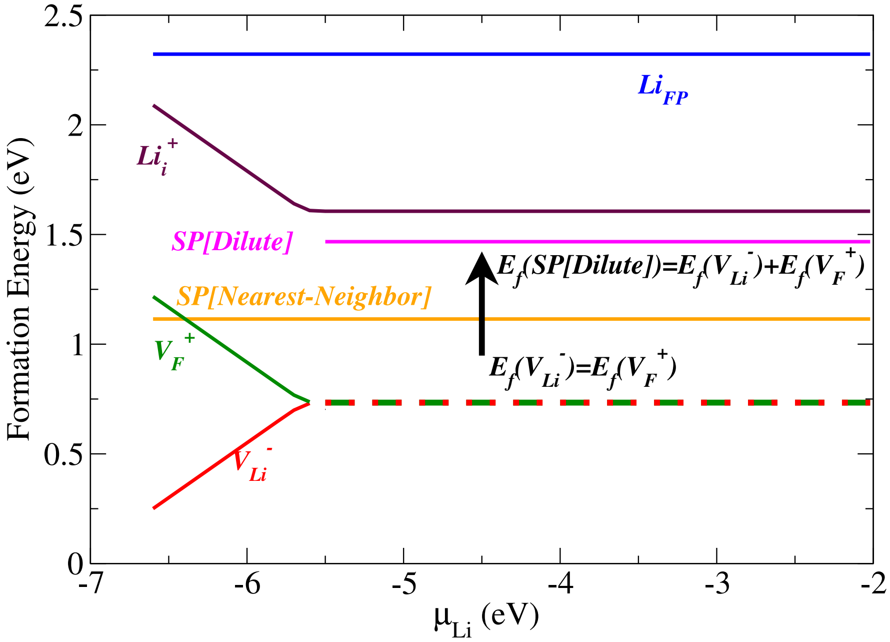

Figure 4.2: Formation energy (E_f) of several defects from TABLE 4.1 with low formation energies as a function of Li chemical potential μ_{Li}. The formation energy of each defect was obtained for the self-consistent (zero-charge) Fermi energy at each value of μ_{Li}.

The higher diffusion barrier for V_F^+ can be attributed to that F^- has a larger ionic radii compared with Li^+.

4.4.3.2 Diffusion of nearest-neighbor schottky pair

It is important to discuss the motion of neutral nearest-neighbor SP and its contribution to the ionic conductivity, since it has higher concentration compared with dilute SP in the intrinsic region. We considered two mechanisms for nearest-neighbor SP to diffuse in the LiF: 1) Nearest-neighbor SP diffuses together to its nearest available site and 2) Nearest-neighbor SP separates to V_{Li}^- and V_F^+ and then diffuse. In ionic conductivity measurement[160], the first mechanism is not counted since the nearest-neighbor SP does not carry any charge (Equation (4.13)).

As a result, the second mechanism is considered in our ionic conductivity calculations. The disassociation energy barrier (ΔG_d, shown in Figure 4.5) is estimated

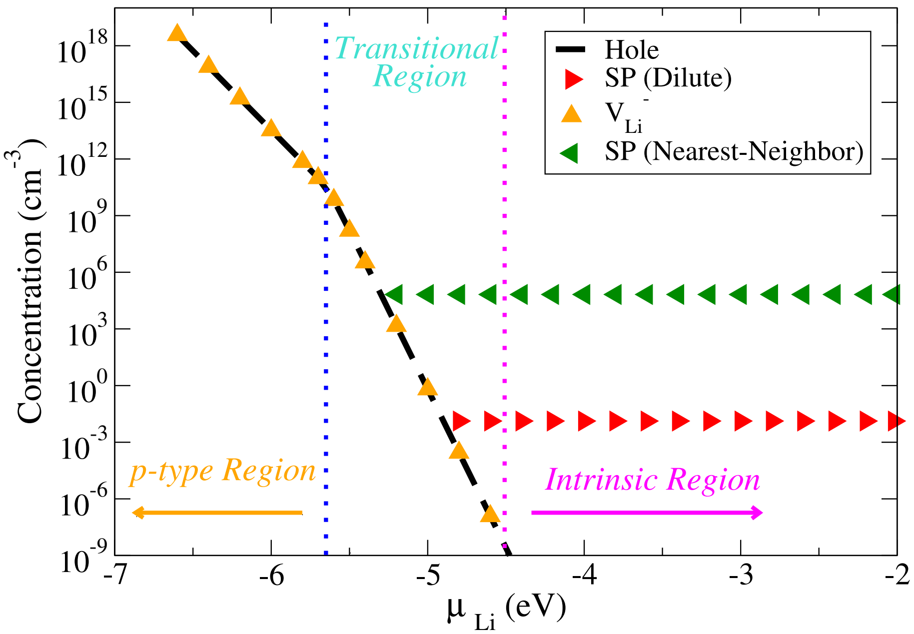

Figure 4.3: Three regions of defect formation (Kröger-Vink Diagram) in LiF as a function of μ_{Li} of the reservoir. V_{Li}^{-} (orange up-triangle) denotes the portion of V_{Li}^{-} whose charge is balanced by holes formation.

based on two assumptions: 1) V_{Li}^{-} is more mobile than V_{F}^{+} (section 4.4.3.1) and 2) Nearest-neighbor SP dissociates when V_{Li}^{-} diffuses to its next nearest neighbor (shown in inserted figure of Figure 4.5). This disassociation energy ($\approx$ 0.6 eV) is added to estimate the contribution of nearest-neighbor SP to ionic conduction. The contribution of NNSP to the total ionic conductivity is about 5 orders of magnitude lower than that from dilute SP at room temperature. Although the second nearest-neighbor SP is not well separated (about 0.1 eV lower in energy than dilute SP), we would expect the contribution of NNSP very small.

4.4.4 Ionic conduction in LiF

The ionic conductivity is calculated according to the main defects in each region defined in Section 4.4.1:

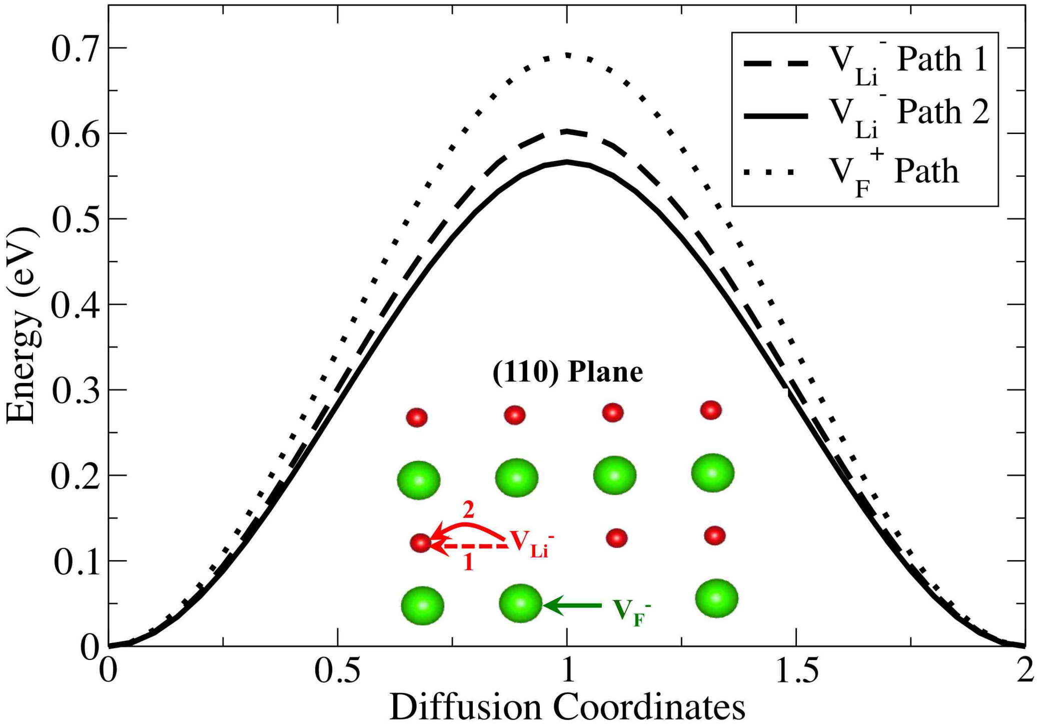

Figure 4.4: Diffusion barriers of V_{Li}^{-} through paths 1, 2 and V_{F}^{+} through the face-centered center path. Insert: Schematic figure shows diffusion pathways for V_{Li}^{-} and V_{F}^{+}.

- **Intrinsic Region**:

$$\begin{aligned}\sigma &= \sigma_{SP_d} + \sigma_{SP_n} \\ &\approx \frac{q^2F^2}{RT}[S_{SP_d} + S_{SP_n}\exp(\frac{-\Delta G_d}{k_BT})](D_{V_{Li}^-} + D_{V_F^+}),\end{aligned} \tag{4.19}$$

where ΔG_d is the disassociation energy calculated in section 4.4.3.2, S_{SP_d} and S_{SP_n} are the concentration of dilute and nearest-neighbor SP. Since V_F^+ has ~0.12 eV higher in migration barrier compared with V_{Li}^-, its contribution is insignificant to the total ionic conduction.

- **Transitional Region**:

$$\begin{aligned}\sigma &= \sigma_{V_{Li}^-} + \sigma_{SP_d} + \sigma_{SP_n} \approx \sigma_{V_{Li}^-} + \sigma_{SP_d} \\ &\approx \frac{q^2F^2}{RT}[pS_{V_{Li}^-}(D_{V_{Li}^-} + D_{V_F^+}) + (1-p)S_{V_{Li}^-}D_{V_{Li}^-}],\end{aligned} \tag{4.20}$$

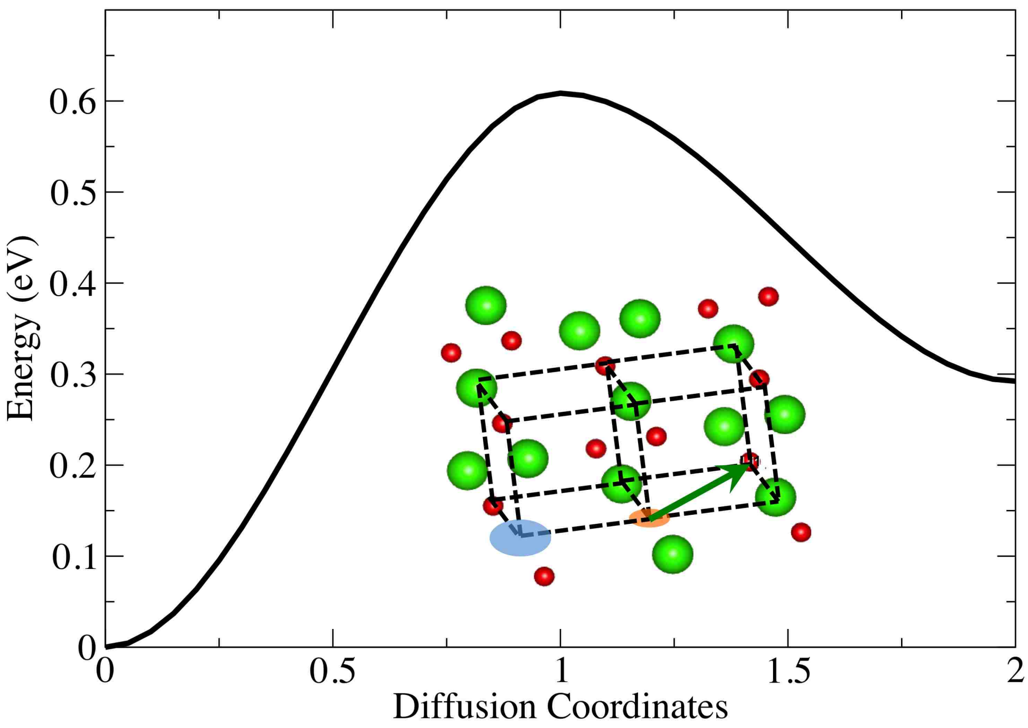

Figure 4.5: Disassociation energy of a Nearest-neighbor Schottky pair. Insert: Schematic figure shows the calculated pathway for the Nearest-neighbor Schottky pair disassociation.

where p is the portion of V_{Li}^- whose charge is balanced by the formation of V_F^+ as defined in Section 4.4.1. In this region, we neglect the contribution from NNSP due to 1) its small contribution compared with dilute SP; 2) in this region, the contribution from V_{Li}^- becomes dominant especially when approaching p-type region.

- ***p*-type Region**:

$$\sigma = \sigma_{V_{Li}^-} = \frac{F^2q^2}{RT} S_{V_{Li}^-} D_{V_{Li}^-}. \tag{4.21}$$

The calculated results are shown in Figure 4.6. The activation energy ($E_f + E_m \approx$ 2.03 eV) in the intrinsic region is comparable with experimental extrapolation (1.99 eV)[159] to the intrinsic region at room temperature. The ionic conductivity is small in the intrinsic region (high μ_{Li}) and is increased dramatically when μ_{Li} is below -4.6 eV. This dramatic increase in ionic conductivity is due to the formation of V_{Li}^{-} which is preferred at low μ_{Li} and it is no longer constrained by the formation of V_{F}^{+} to balance the charge (Figure 4.3).

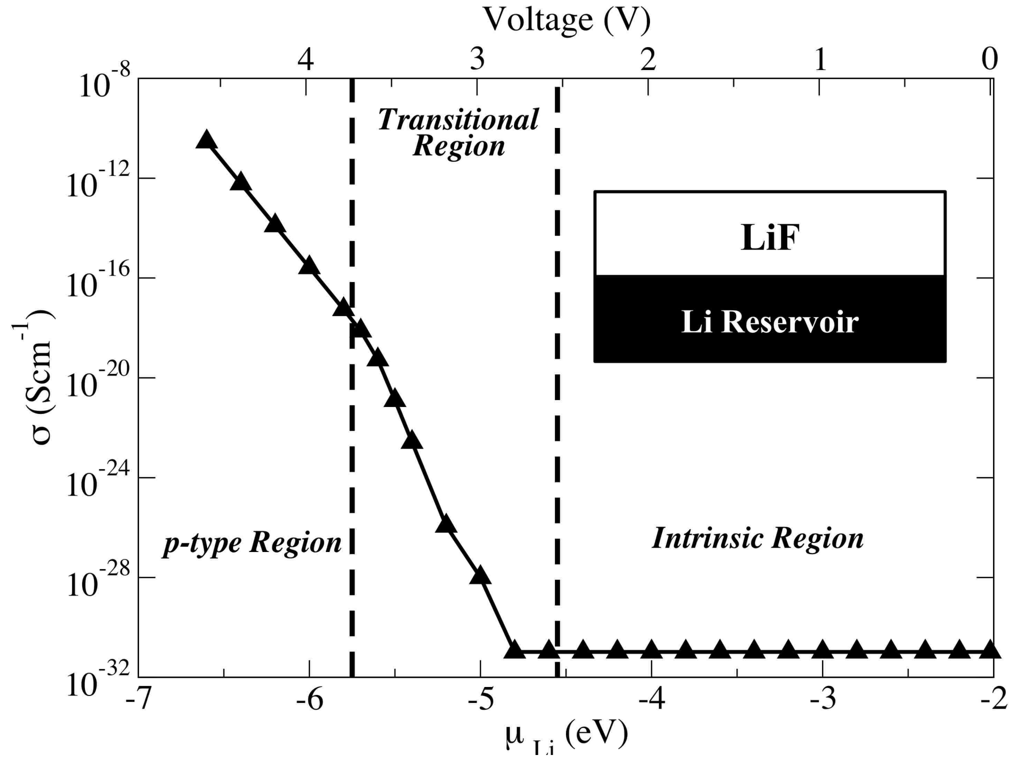

Figure 4.6: Ionic conductivity of LiF as a function of the chemical potential of Li reservoir. Insert: schematic drawing of LiF contacting a Li reservoir (e.g., an electrode for application of LIBs).

4.4.5 LiF as an engineered SEI for LIBs

Considering a solid electrolyte (an engineered artificial SEI) coated on electrodes for LIBs, the Li reservoir (insert in Figure 4.6) can be viewed as an electrode on which the LiF is coated. For different electrodes (e.g., $\mu_{Li}^{Li-metal} \sim -2.02$ eV, $\mu_{Li}^{LiCoO_2} = -6.2$ eV) or electrodes with different state of charge (e.g., LiC_{12}, LiC_6), the values of μ_{Li} are different. In electrochemistry, the electrochemical potential of Li$^+$ in a spatial point is defined as[162]

$$\tilde{\mu}_{Li^+} = \mu_{Li^+} + z_i F \phi, \tag{4.22}$$

where $\tilde{\mu}_{Li^+}$ is the electrochemical potential, μ_{Li^+} is the chemical potential of Li^+, z_i ($z_i = 1$ for Li^+) is the associated charge, and ϕ is the electrical potential in that spatial point. At thermodynamic equilibrium, the electrochemical potential is the same everywhere in a battery (i.e., $\tilde{\mu}_{Li^+}^{Cathode} = \tilde{\mu}_{Li^+}^{Anode}$). Under this condition, we can estimate the cell voltage by

$$V = \phi^{Cathode} - \phi^{Anode} = -\frac{\mu_{Li^+}^{Cathode} - \mu_{Li^+}^{Anode}}{F}. \tag{4.23}$$

By assuming $\mu_{Li} \approx \mu_{Li^+} + \mu_{\ominus}$ in the electrode and the same wire (e.g., copper) used to connect the cathode and anode ($\mu_{\ominus}^{Cathode} = \mu_{\ominus}^{Cathode}$), the voltage of the cell can be estimated from the differences of μ_{Li} in electrodes. This is the well-know Nernst equation in electrochemistry[85]. In LIBs, μ_{Li} in Li metal is typically defined as a reference (zero volt). Therefore, we can relate μ_{Li} in the reservoir to the open-circuit voltage of the electrodes (a half cell) by referencing to μ_{Li} in Li metal

$$V = -(\mu_{Li} - \mu_{Li}^{Metal})/e. \tag{4.24}$$

The ionic conductivity σ in LiF highly depends on the electrode it contacts with. For example, if LiF is coated on a negative electrode surface (e.g., graphite, silicon), σ is very small($\approx 10^{-30}$ Scm^{-1}). Compared with σ in other SEI species (e.g., Li_2CO_3[98,99]), σ in LiF is 18 to 20 orders of magnitude lower. However, if it is coated on a positive electrode (e.g., $LiCO_2$), σ is controlled by free V_{Li}^- diffusion and it is comparable with other SEI species (e.g., Li_2CO_3[98,99]). This result is significant since it demonstrates that the ionic conductivity of LiF is strongly voltage-dependent. Therefore, higher doping of divalent cation (e.g., Mg^{2+}) is suggested to improve Li ion conductivity of LiF coating on negative electrodes by increasing the concentration of diffusion carrier V_{Li}^-.

The ionic transport contributes to the electrical conduction in ionic crystals (e.g., LiF).[31,80] It can be expected that LiF is more electrical insulating on the negative electrode than other species (e.g., Li_2CO_3[98,99]) due to its low ionic conductivity. It was believed that the electron leakage from the electrode is an important step in the ethylene carbonate decomposition leading to SEI formation.[100–102] Various groups have reported fluoroethylene carbonate (FEC) as an electrolyte additive that can improve the performance of Si electrode with increased LiF formation in the SEI layer.[120–125] Our results provide a reason for this observation that LiF on the negative electrode surface can better passivate the electrode surface and prevent electron leakage. As a result, it can cause less capacity loss and longer cycling life of the electrode.

4.5 Conclusions

We developed a new method to study the defect physics in a material in equilibrium with an external phase. This method establishes a correlation between the open-circuit voltage and Li chemical potential in the electrodes. We applied this approach to study defect reactions in LiF in contact with different electrode materials which serve as Li reservoirs. We demonstrate that the defect formation in a solid electrolyte can be affected by the open-circuit voltage of the electrode, which is a measurable and controllable parameter. Three regions (intrinsic, transition, and *p*-type) were defined to describe the main defect reactions with different electrodes. We found that the main defect type in the intrinsic region (high μ_{Li} reservoirs) was Schottky pair and in the *p*-type region (low μ_{Li} reservoirs) was Li-ion vacancy. The diffusion barrier of main defects in each region was estimated from CI-NEB calculation and mapped to ionic conduction based on the Nernst-Einstein formula. The ionic conductivity is very low (10^{-31} $\mathrm{Scm^{-1}}$) in the intrinsic region and increases (to 10^{-12} $\mathrm{Scm^{-1}}$ when $\mu_{Li} \approx -6.5$ eV) with increasing the voltage of the nearby electrode. Thus, the ionic conduction in a solid electrolyte is very sensitive to the external potential of the electrode on which the electrolyte material is coated. This work extends the well known relationship between defect concentration and chemical potential for gas phase reactions to electrochemical reactions.

Chapter 5 Electrical conduction in multi-component solid electrolyte interphases

5.1 Summary

Designing a solid electrolyte interphase (SEI) with high ionic conductivity and low electronic conductivity is believed to be important for high performance and durable Li ion batteries. Li ionic conduction in SEI affects the rate performance, while the electron leakage through SEI causes electrolyte decomposition and, thus, causes capacity loss. To help design an artificial SEI, it is necessary to know the defect chemistry and transport in the multicomponent SEI present on electrodes.

In this chapter, we present a multi-scale model based on density functional theory and space charge model to investigate the defect distribution in a multicomponent SEI consisting of LiF and Li_2CO_3. We consider the effects of LiF/Li_2CO_3 interface on the defect redistribution in the bulk of LiF and Li_2CO_3 that are both in equilibrium with the electrode. On negative electrodes, the dominant defect type in LiF is Schottky pair while the major ionic carrier in Li_2CO_3 is Li ion interstitial whose charge is balanced by electrons. Based on these bulk defects, we calculated the defect redistribution near the LiF/Li_2CO_3 interface by considering the defect migrations and reactions across the interface. Because the low concentration of ionic carriers in the bulk LiF, we approximated LiF as an ionic insulator in the mixture. We found that, in the ionic space charge region of Li_2CO_3 near the LiF/Li_2CO_3 interface, Li ion interstitial is accumulated but the electron is depleted. This demonstrates a possibility that, by engineering a mixture of LiF and Li_2CO_3 in an artificial SEI, the ionic conduction can be enhanced and the electron leakage through the SEI can be reduced, thus enhancing the durability and performance of electrodes.

This chapter is reproduced from the theoretical part of the work published as: Qinglin Zhang†, Jie Pan†, Peng Lu, Zhongyi Liu, Mark W. Verbrugge, Brian W. Sheldon, Yang-Tse Cheng, Yue Qi, Xingcheng Xiao, “Synergetic Effects of Inorganic Components in Solid Electrolyte Interphase on High Cycle Efficiency of Lithium Ion Batteries” Nano Letters, 16(3), 2011-2016 (2016) (†: co-first author). Copyright © American Chemical Society 2016

5.2 Introduction

One of the most significant challenges for current and future lithium ion batteries is to control the charge transfer at the electrode/electrolyte interface.[163,164] This issue is further complicated by the existence of an ultrathin interphase layer covering the electrode.[163] This interphase layer is typically formed by electrolyte decomposition and called as the solid electrolyte interphase (SEI). However, the name of SEI does not fully capture its multi-functional nature. Ideally it should be: (1) electronic insulating (suppress the electrolyte reduction)[101]; (2) ionic conducting (enable the fast Li ion transport)[26,163,165]; (3) mechanically “tough” (sustain the large strains in electrodes during cycling)[26,166]; and (4) chemically stable (long shelf- and cycle-life)[26].

Intensive research efforts have been devoted to designing an artificial SEI layer in order to control the electron and ion transport at the electrode/SEI/electrolyte interface. For example, inorganic coatings, e.g., oxides[26], carbonates[167], and fluorides[168], and electrolyte additives, e.g., Fluoroethylene Carbonate (FEC)[123,169–171], have been developed to modify the properties of SEIs to stabilize the electrode. These efforts motivated extensive studies on correlating the structure and property of each SEI component to the performance of the battery.[123,163,170–172], It has been believed that that there are four major inorganic components in naturally formed SEI from liquid electrolyte decomposition and the main inorganic components include: lithium carbonate (Li_2CO_3), lithium alkylcarbonate, lithium oxide (Li_2O), and lithium fluoride

(LiF).[101,123,163,172,173] Their mechanical and transport properties have been investigated by simulations[174,175] and their contributions in naturally formed SEI to the cycling performance have been revealed by experiments as well[119,123,170].

However, the complex mosaic and heterogeneous structural nature of naturally formed SEI has not been fully understood. For example, the ionic conduction through the multi-component SEI depends on various factors, such as interfacial defect chemistry, topological distribution of phases.[176,177] In a broader view of solid ionic conductors, it has been demonstrated that the bulk transport properties can be either increased or decreased dramatically, sometimes anomalously, by introducing heterogeneous structures and interfaces. For example, addition of small insulating particles into ionic conductors may, under certain conditions, enhance the ionic conductivity due to a space-charge layer effect.[178] This was firstly observed when non-Li-conducting Al_2O_3 was mixed with LiI, resulting in a heterogeneous structure, where Li ion was adsorbed into the Al_2O_3 interface, which increases the Li vacancy (the diffusive carrier) concentration in LiI by orders of magnitude.[178] Utilizing this effect and reducing the distance between the space-charge layers, multi-layer fast ionic conductors were achieved.[179] On the other hand, the ionic conductivity in structures with heterogeneous interfaces can decrease due to the depletion of ionic carriers near the interface, such as Li ion conduction near the LiF/Al_2O_3 interface.[180,181] As a result, whether SEI components have synergetic or antagonistic effects remains an open question. We believe that addressing this question can lead to a new avenue of designing artificial SEI design and precise control of electron and ion transport at the electrode/electrolyte interface.

Two interesting SEI components, Li_2CO_3 and LiF serve as a good example to explore this question. In this study, we chose Li_2CO_3 and LiF as two representative components to show the effect heterogeneity in the SEI to the electrical conduction. Both components form crystalline phases on the electrode and they are stable in the

SEI comparing with other phases, such as lithium alkylcarbonate[173]. In addition, we believe that Li_2CO_3 is a close approximation to other carbonates, such as alkylcarbonate, to calculate the SEI properties. Theoretically, it has been shown that the dominant defects in a pure LiF coating on negative electrodes are Schottky pairs (cation and anion vacancy pair).[175] Due to the low defect concentration and high transport barriers, LiF coating on negative electrodes was believed to be a good electronic insulator with poor ionic conductivity ($\approx 10^{-31}$ S/cm).[175] On the other hand, the main defect in Li_2CO_3 in contact with negative electrodes is Li ion interstitials with its charge balanced by free electrons.[99,174] As a result, Li_2CO_3 can provide relatively high ionic conductivity ($\approx 10^{-8}$ S/cm) but containing a considerable electron concentration on negative electrodes.[99,174] Considering these drawbacks, neither one of them alone has the desired properties as an ideal SEI. However, they may benefit from each other as they co-exist in SEI to provide improved ionic conduction and electronic insulation on negative electrodes.

5.3 Methodology and theory

5.3.1 Interfacial defect reactions and space charge potential

The heterostructural interface can influence the defect distribution and thus, vary the ionic and electronic conductivity compared with those in the bulk materials.[81,176,179,182] Multiple physical processes can occur when two different materials are in contact[176], e.g., the lattice mismatch, the formation of a third phase. However, to a first approximation, we consider an planar abrupt interface of which the atomic structures maintain the same as those in the perfect crystal (Figure 5.1). As a result, the properties of materials behave as a step function around the interface, e.g., formation energy of defects, dielectric constant.

An important physical process shall be considered near this ideal interface is the defect reactions at the interface, i.e., electrochemical reaction[176]. The defect reactions depend on the type of dominant defects in the bulk materials. The dominant defect in Li_2CO_3 on anode is Li ion interstitial ($Li_i^\bullet$) and the positive charge is balanced by electrons (e$'$).[174] In LiF, the main defect is Schottky pair, i.e., Li ion (V_{Li}') and F ion vacancies ($V_F^\bullet$).[175] The flow of electrons across the interface is neglected, since LiF is an electronic insulator when coated on anode.[175] As a result, we consider the following four defect reactions (as depicted in Figure 5.1, A denotes Li_2CO_3 and B denotes LiF):

(R1): A lattice Li ion in LiF migrates to form a $Li_i^\bullet$ in Li_2CO_3:

$$Nil \implies Li_i^\bullet(A) + V_{Li}'(B);$$

(R2): A lattice Li in Li_2CO_3 migrates to occupy a V_{Li}' in LiF (i.e., V_{Li}' migrates from LiF to Li_2CO_3):

$$V_{Li}'(B) \implies V_{Li}'(A);$$

(R3): A lattice Li in Li_2CO_3 migrates to form a $Li_i^\bullet$ in LiF:

$$Nil \implies Li_i^\bullet(B) + V_{Li}'(A);$$

(R4): A $Li_i^\bullet$ in Li_2CO_3 migrates to form a $Li_i^\bullet$ in LiF:

$$Li_i^\bullet(A) \implies Li_i^\bullet(B).$$

The chemical potential difference $\Delta\mu$ after the reaction determines whether the reaction is favorable at this interface. The chemical potential of a defect M with charge z and the equilibrium bulk concentration c_{M^z} in a material can be determined by

$$\mu_{M^z} = \mu_{M^z}^\circ + k_B T \ln\left(\frac{c_{M^z}}{N_s(M^z)}\right) + k_B T \ln f_{M^z}, \tag{5.1}$$

where $\mu_{M^z}^\circ$ represents the standard chemical potential of M^z in the bulk and $N_s(M^z)$ is the density of the available sites for defect M^z. f_{M^z} is the activity coefficient and is approximated to be zero by considering dilute defect situation. At the initial contact, we consider a reaction is favorable when

$$\Delta\mu < 0. \tag{5.2}$$

From first principles calculations of bulk defect properties of LiF and Li_2CO_3 coated on anode[174,175], we found that only reaction (R1) is possible at LiF/Li_2CO_3 interface ($\Delta\mu \approx -0.95$ eV). The energy levels of reaction (R1) is depicted in Figure 5.2(a). In addition, the migrations of fluorine and oxocarbon ion between Li_2CO_3 and LiF are neglected since these processes are energetically unfavorable.

This interfacial defect reaction allows the deviation from local electrical neutrality, i.e., building up a space charge potential $\phi(x)$ near the interface (Figure 5.2 (b) and (c)), and it is very important to the distribution of defects.[179–181,183–186] As a result, $Li_i^\bullet$ is accumulated near the interface in Li_2CO_3 with V_{Li}' segregation in LiF side. The equilibrium condition of this reaction is reached[176] when

$$\sum_i \tilde{\mu_i} = \tilde{\mu}_{Li_i^\bullet} + \tilde{\mu}_{V_{Li}'} = 0, \tag{5.3}$$

where $\tilde{\mu_i}$ is the electrochemical potential of defect i with charge z_i

$$\tilde{\mu_i} = \mu_i^\circ + k_B T \ln\left(\frac{c_i}{N_s(i)}\right) + z_i e\phi(x) = \mu_i + z_i e\phi(x). \tag{5.4}$$

The penetration of this reaction from the interface to the bulk material, which is characterized as the space charge region, depends on the Debye length of the material[176]. At the boundary of the space charge region, this reaction reaches its equilibrium and the defect concentration approaches the value in the bulk. As a result, the built-up space charge potential difference ($\Delta\phi$, depicted in Figure 5.2 (c)) can be calculated by

$$e\Delta\phi = \phi_A^\infty - \phi_B^\infty = -(\mu_{Li_i^\bullet}(A) + \mu_{V_{Li}'}(B)). \tag{5.5}$$

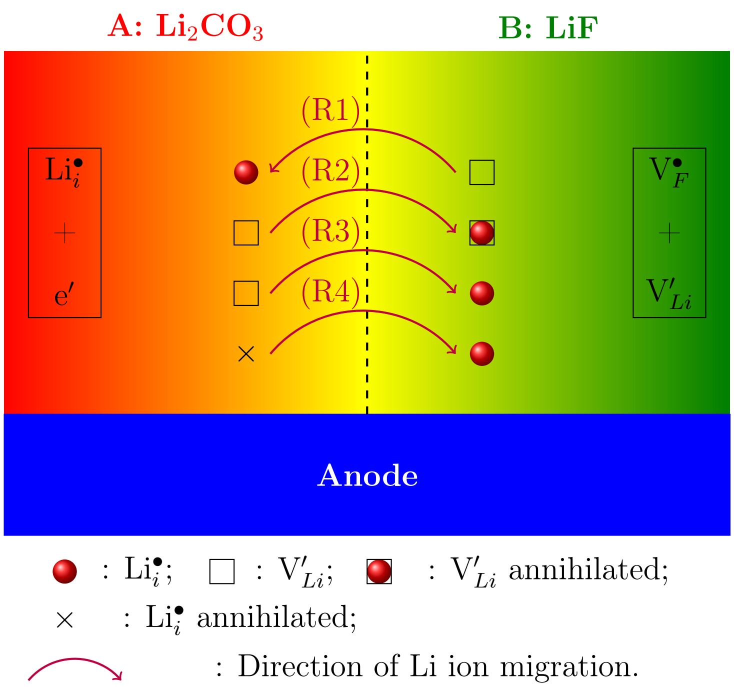

Figure 5.1: Defect reactions [(R1)-(R4)] at the LiF/Li_2CO_3 interface on anodes.

5.3.2 Space charge model

In the space charge region (typically within $\approx 2\lambda_D - 3\lambda_D$, λ_D is the Debye length[81,176,184,185], the deviation from the local charge neutrality is allowed due to the defect reactions. The net charge density in the space charge region can be expressed as

$$\rho(x) = \sum_i z_i c_i(x), \tag{5.6}$$

where $c_i(x)$ is the density of the charged defect i and z_i is the amount of charge carried by a single defect i. The density of the charged defects $c_i(x)$at a spatial point x with electrostatic potential $\phi(x)$ can be calculated by

$$c_i(x) = c_i^\infty \mathrm{e}^{-\frac{z_i e \phi(x)}{k_B T}}, \tag{5.7}$$

where c_i^∞ is the bulk defect density. In the bulk material, the charge neutrality is maintained by the following relationship

$$\rho(x = \infty) = \sum_i z_i c_i^\infty = 0. \tag{5.8}$$

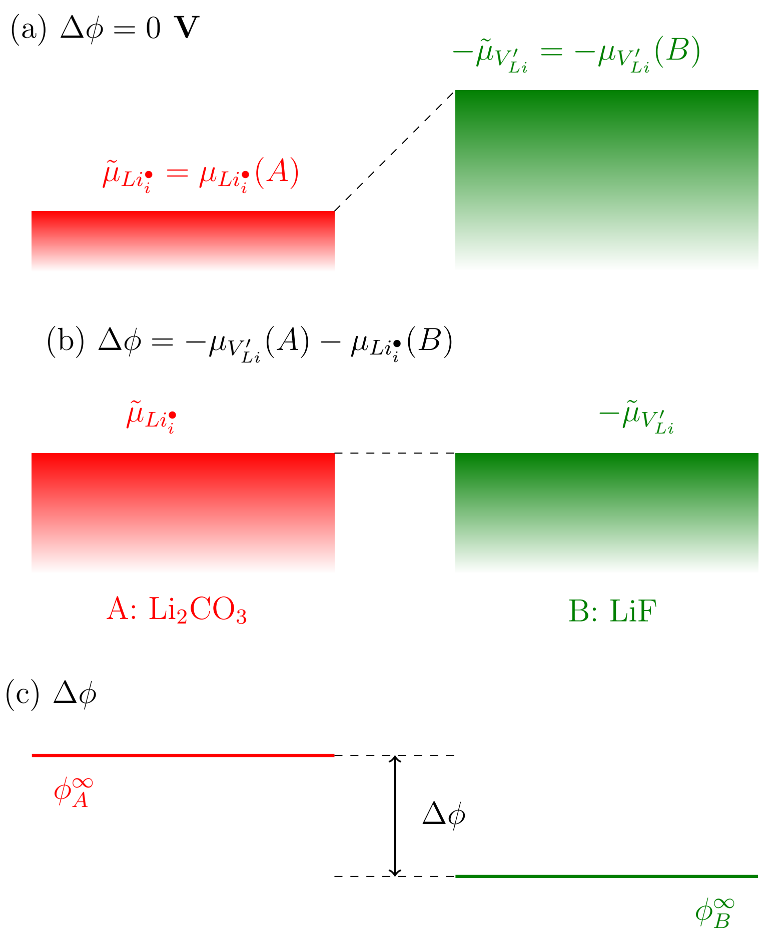

Figure 5.2: Energy levels of defect reaction $Nil = Li_i^\bullet(A) + V'_{Li}(B)$ before (a) and after (b) equilibrium at the boundary of space charge region near LiF/Li_2CO_3 interface. (c) $\Delta\phi = \phi_A^\infty - \phi_B^\infty$.

According to the poison's equation, we can have

$$\begin{aligned}\frac{\partial^2\phi(x)}{\partial x^2} &= -\frac{\rho(x)}{\varepsilon\varepsilon_r}\\ &= -\sum_i z_i c_i(x)/\varepsilon\varepsilon_r.\end{aligned} \tag{5.9}$$

5.3.3 Interfacial defect chemistry and electrical conductivity

The defect chemistry near the interface can influence the electrical conductivity, i.e. ionic and electronic conductivity. We consider the electrical conductivity parallel to

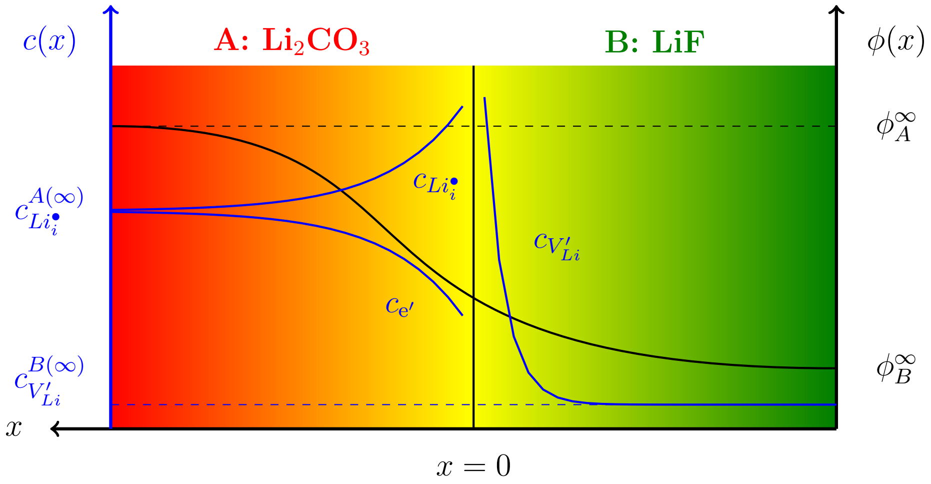

Figure 5.3: Space charge model for LiF/Li_2CO_3 interface.

the interface. According to the Nernst-Einstein relationship, the ionic conductivity is propotional to both the concentration and diffusivity of the defect carrier that is the dominant defects. We assume that the ionic transport barrier of accumulated defects in the space charge region does not change significantly with that in the bulk. The total concentration of ionic carriers (M^z) is[183]

$$S'_{M^z} = \frac{1}{L}\int_0^L c_{M^z}(x)\mathrm{d}x, \tag{5.10}$$

where L is the average grain size. As a result, the change of defect concentration compared with bulk material of the same size (L) can be expressed as

$$\Delta S_{M^z} = S'_{M^z} - S^\infty_{M^z}, \tag{5.11}$$

where $S^\infty_{M^z} = \int_0^L c^\infty_{M^z}\mathrm{d}x = c^\infty_{M^z}L$ is the defect concentration in the bulk. According to Nernst-Einstein relationship, the variation in ionic conductivity due to this interface is

$$\Delta\sigma = \frac{z^2F^2D_{Li_i^\bullet}}{RT}\Delta S_{M^z}. \tag{5.12}$$

If $L = \infty$, the increment in ionic conduction is

$$L\Delta\sigma = \Delta Y = \frac{z^2F^2D_{M^z}}{RT}\int_0^\infty \mathrm{d}x[c_{M^z}(x) - c^\infty_{M^z}], \tag{5.13}$$

Similarly, the total electrons near the interface can be calculated by

$$n_e = \frac{1}{L}\int_0^L c_e(x)\mathrm{d}x. \tag{5.14}$$

As a result, the influence of the interface to the electronic conductivity can be estimated

$$\Delta\sigma_e = e\mu_e\Delta n_e, \tag{5.15}$$

where μ_e is the mobility of electrons and it is assumed to be the same in the space charge region as in the bulk material, Δn_e is the amount of electron which is depleted near the interface $\Delta n_e = n_e' - n_e^\infty$.

5.4 Results and discussion: Gouy-Chapman profile in Li$_2$CO$_3$

At the LiF/Li$_2$CO$_3$ interface, Li ions tend to migrate from LiF side (A) to Li$_2$CO$_3$ side (B) forming Li ion interstitials ($Li_i^\bullet$) in B and leaving Li ion vacancies (V_{Li}') behind in A. We consider LiF is an ionic insulator on the anode surface for the following two reasons: 1) The concentrations of majority defects in bulk Li$_2$CO$_3$ and LiF varies orders of magnitude ($\frac{c_{Li_i^\bullet}(A)}{c_{V_{Li}'}(B)} \approx 10^{12}$)[174,175]; 2)The defect concentration dies out dramatically from the interface to the bulk LiF ($c_{V_{Li}'}$ curve in Figure 5.5). With this consideration, our space charge model in Figure 5.3 can be simplified to a semi-infinite model as depicted in Figure 5.4: 1) In LiF side, there accumulated a high concentration of V_{Li}' that is comparable with the dominate defect concentration in bulk Li$_2$CO$_3$ near the interface ($\approx 1-2$ nm from the interface); 2) The potential drop in LiF side is very small and we approximate $\phi(x=0) \approx \phi_B^\infty$. Equation (5.9) can be written as the following for the space charge region in Li$_2$CO$_3$

$$\begin{aligned}\frac{\partial^2\phi(x)}{\partial x^2} &= -\frac{e}{\varepsilon\varepsilon_r}(c_{Li_i^\bullet}^\infty \mathrm{e}^{\frac{-e\phi(x)}{k_BT}} - c_{\mathrm{e}'}^\infty \mathrm{e}^{\frac{e\phi(x)}{k_BT}})\\ &= -\frac{ec_{Li_i^\bullet}^\infty}{\varepsilon\varepsilon_r}(\mathrm{e}^{\frac{-e\phi(x)}{k_BT}} - \mathrm{e}^{\frac{e\phi(x)}{k_BT}}),\end{aligned} \tag{5.16}$$

where the concentration of electron and Li ion interstitial in the bulk Li$_2$CO$_3$ are equal ($c_{\mathrm{e}'}^\infty = c_{Li_i^\bullet}^\infty$). For simplicity, we define a concentration enhancement $\zeta = \frac{c_{Li_i^\bullet}(x)}{c_{Li_i^\bullet}^\infty}$

and Equation (5.16) becomes[183]

$$\frac{\partial^2 \ln\phi(\xi)}{\partial\xi^2} = \frac{1}{2}(\zeta - \zeta^{-1}), \tag{5.17}$$

where $\xi = x/\lambda_D$ and λ_D is the Debye length in Li_2CO_3 which is defined as[183]

$$\lambda_D = \sqrt{\frac{\varepsilon\varepsilon_r RT}{2F^2 c^{\infty}_{Li_i^\bullet}}}. \tag{5.18}$$

If we assume the interface is a planar contact and the grain size of lithium carbonate is larger than its Debye length ($\lambda_D^{Li_2CO_3} \approx 19$ nm when $\varepsilon_r = 4.9$[187]), we can have[183]

$$\zeta = \left[\frac{1+\vartheta e^{-\xi}}{1-\vartheta e^{-\xi}}\right]^2, \tag{5.19}$$

where $\vartheta = \frac{1-\zeta^{-1/2}(\xi=0)}{1+\zeta^{-1/2}(\xi=0)}$.

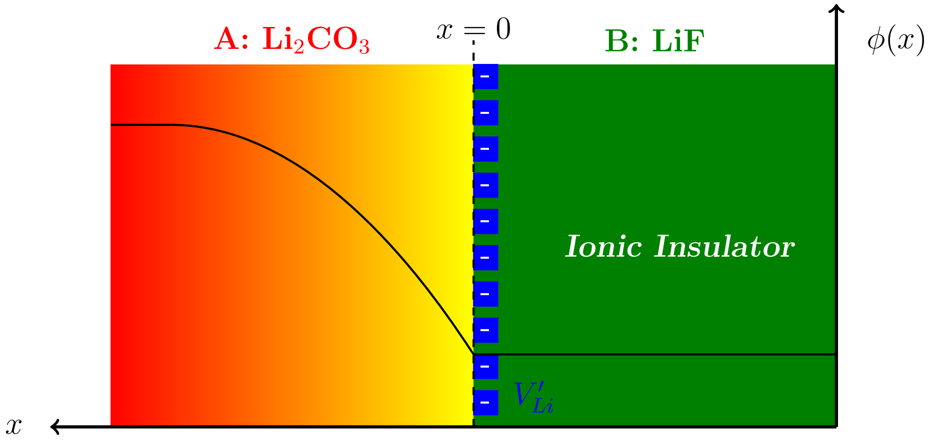

Figure 5.4: Simplified semi-infinite model for space charge region in Li_2CO_3 near LiF/Li_2CO_3 interface.

The concentration of accumulated Li ion interstitials, $c_{Li_i^\bullet}(x)$, and electrons,$c_{e'}(x)$, in Li_2CO_3 can be related to the potential $\phi(x)$ by solving the Poisson-Boltzmann relationship, based on the space charge model (Equation 5.16). The calculated defect distribution and the electrostatic potential are shown in Figure 5.5. We found that the Li ion interstitials are accumulated in the space charge region and the electrons are depleted (Figure 5.5). Near the interface, the concentration of ionic carriers in Li_2CO_3

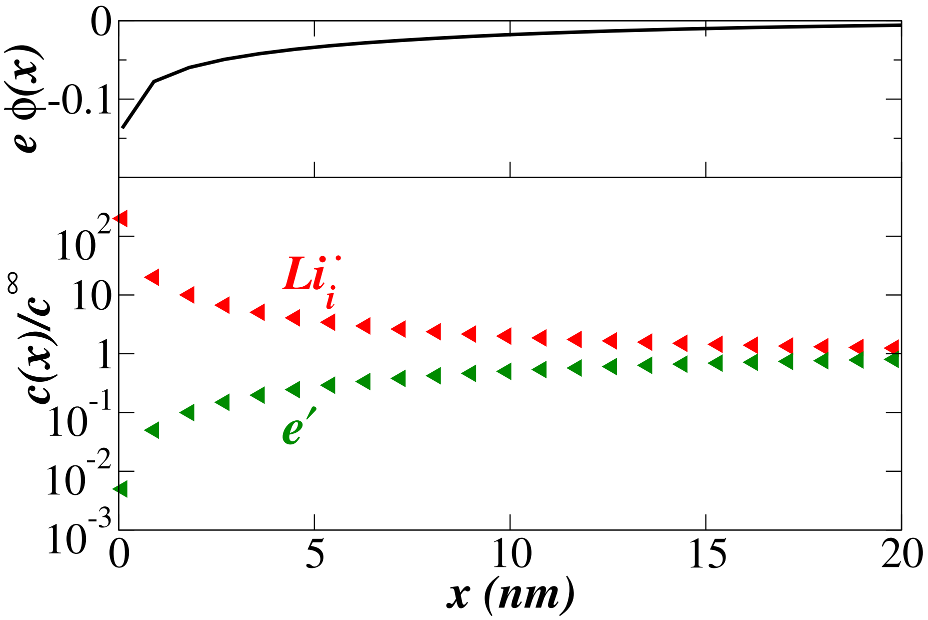

Figure 5.5: Defect distribution in the space charge region of Li_2CO_3 near the LiF/Li_2CO_3 interface.

can increase by two orders of magnitude compared with that in bulk Li_2CO_3. As a result, Li ionic conductivity can be promoted by introducing LiF/Li_2CO_3 interfaces due to the increased amount of ionic carriers. According to the Nernst-Einstein relationship15, the ionic conductivity is proportional to the concentration of ionic carriers. As a result, the accumulation of $Li_i^{\bullet}$ near the interface in Li_2CO_3 would increase the density of ionic charge carriers, promote the ionic conduction through Li_2CO_3, and improve the charge transfer step through the SEI. In addition, due to the depletion of electrons near the interface (Figure 5.5), the electron leakage through the LiF and Li_2CO_3 composite coating can be reduced (Equation 5.15) by building up the LiF/Li_2CO_3 interface.

5.5 Conclusions

In summary, we developed a density functional theory informed space charge model to study the defect chemistry near LiF and Li_2CO_3 interface. We found that, near this heterogeneous interface, the ionic carriers, i.e., Li ion interstitials in Li_2O_3, are accumulated while the electronic carriers, i.e., electrons in Li_2CO_3, are depleted. This increment in ionic carrier concentration can facilitate the Li ion transport, especially parallel to the heterogeneous interface, through the composite SEI and improve the rate capability of the coated electrode. The decrease in electronic concentration can prevent electron leakage through the SEI and avoid additional electrolyte decomposition and severe capacity loss. As a result, LiF in the multicomponent SEI plays two important roles: (1) The defect chemistry near LiF/Li_2CO_3 interface can make Li_2CO_3 more electronic insulating by depleting electrons near the interface but more ionic conducting by accumulating ionic carriers; (2) LiF itself is a good electronic insulator to prevent electron leakage.

Chapter 6 Design of nanostructured heterogeneous solid ionic coatings for artificial solid electrolyte interphases

6.1 Summary

Understanding of the electrical conduction, i.e., ionic and electronic conduction, through the solid electrolyte interphase (SEI) is critical to the design of durable lithium ion batteries (LIBs) with high rate capability and long life. It is believed that an ideal SEI should be an ionic conductor but an electronic insulator. In this study, we present a theoretical design of an artificial SEI consisting of lithium fluoride (LiF) and lithium carbonate (Li_2CO_3) on a LIB anode based on a newly developed density functional theory (DFT) informed space charge model. We demonstrate that the migration of lattice Li ions from LiF phase to form Li interstitials in Li_2CO_3 is energetically favorable near the LiF/Li_2CO_3 interface. At equilibrium, this interfacial defect reaction establishes a space charge potential across the interface which causes the accumulation of ionic carriers but the depletion of electronic carriers near the LiF/Li_2CO_3 interface. To utilize this space charge effect, we propose a computationally designed nano-structured artificial SEI structure with high density of interfaces of LiF and Li_2CO_3 perpendicular to the electrode. Based on this structure, the influence of grain size and volume ratio of the two phases were studied. Our results reveal that reducing the grain size of Li_2CO_3 in the nano-structured composite can promote ionic carriers and increase the ionic conductivity through the composite SEI by orders of magnitude. At the same time, the electronic conductivity is reduced due to electron depletion near the LiF/Li_2CO_3 interface. Furthermore, an optimal volume fraction which ensures high ionic and low electronic conduction was predicted.

This chapter is reproduced from the work published as: Jie Pan, Qinglin Zhang,

Xingcheng Xiao, Yang-Tse Cheng, Yue Qi, "Design of Nanostructured Heterogeneous Solid Ionic Coatings through a Multiscale Defect Model," ACS Applied Materials & Interfaces 8(8), 5687-5693 (2016). Copyright © American Chemical Society 2016

6.2 Introduction

A grand challenge to design lithium ion batteries (LIBs) with high energy and power density is to mitigate the side reactions and maintain the discharge capacity after many cycles.[1,163,188,189] The capacity retention highly relies on the formation of a stable solid electrolyte interphase (SEI) which acts as a protective layer on the electrode, e.g., graphite.[95,163,190] However, the naturally formed SEIs cannot always passivate the electrode, since the structure and composition of SEI depend on various factors, such as solvents and additives in electrolytes[114,169–171,191–193], surface chemistry of electrodes[194–196] , and mechanical degradation of electrodes[197]. For example, the promising anode material silicon (Si) with the highest theoretical capacity[198] can not maintain the natural SEI[197] due to the large stress and strain generated in the electrode during operation[103,166,199–202]. The SEI on metal oxide cathode also cannot efficiently prevent dissolution of the redox-active metal from cathode to the liquid electrolyte[203]. It is believed that these physical phenomenon caused by the lack of a protective interphase between electrode material and electrolyte can cause severe capacity loss which shortens the life of batteries. As a result, engineering a protective coating, also known as an artificial SEI, on electrodes is very important to improve the capacity retention of lithium ion batteries (LIBs). In the past, inorganic materials, such as oxides (e.g, Al_2O_3[26], TiO_2[204]), carbonates[167], and fluorides(e.g., AlF_3[168], CaF_2[205]), have been applied as artificial SEI coatings to improve the capacity retention of electrodes.

Theoretically, an ideal artificial SEI shall be an ionic conductor[206,207] and electronic insulator[101,163,194,208], sharing the same characteristics as the requirements for a solid electrolyte material. A high Li ionic conductivity in the artificial SEI enables good rate performance[206,207] while the blockage of electrons leaking from the electrode to the electrolyte prevents the decomposition of electrolyte molecules, e.g., ethylene carbonate, which consumes Li.[101,163,194,208] The electrical conduction, i.e., ionic and electronic conduction, in most coating materials depends on the defect concentration and transport.[81,175] The defect chemistry in inorganic matters can be manipulated through doping of ions with different valence charge[209,210], varying the properties of the environment[81,175], and designing heterogeneous systems[81,176,179,211].

Designing heterostructural systems (or multi-component systems) can be a promising approach to alter the defect chemistry, and as a result, effectively tune the electrical conduction. Liang discovered that, by mixing alumina (Al_2O_3) into solid electrolyte material lithium iodide (LiI), the ionic conductivity can be increased by two orders of magnitude compared with that in pure LiI.[178] A similar behavior was also observed in other systems, e.g., Al_2O_3/AgI[212], Al_2O_3/$LiBr{\cdot}H_2O$[213], Al_2O_3/AgCl[183], SiO_2/AgCl[183], LiF/TiO_2[180,186], and LiF/SiO_2[214]. The origin of this improved ionic conduction was attributed to the formation of space charge layers near the two-phase interfaces.[176,184,185] In these space charge layers, the density of diffusive ionic carriers can be increased, thus providing dramatically improved ionic conduction along the interface.[176,184,185,215] However, a range of physical properties of the two-phase mixture can affect the space charge layer, such as particle/grain size[183,216–218], volume fraction[178,183], and the topological distribution of two phases[176,177,219]. Previous examples have shown that the ionic conduction would firstly increase and then decrease with the volume fraction of the ionic insulator. It suggests that the density of heterogeneous interfaces as a function of the volume fraction can be optimized.[183] Furthermore, the particle/grain size and the distribution of phases can affect percolating paths for ionic conduction[177]. However, the lack of a predictive and quantitative model hinders the development and design of heterogeneous solid ionic materials (in general) and coatings (in artificial SEI applications). A model that can predict the interracial defect chemistry and also consider the heterogeneous structure complexity shall be developed.

In this study, we developed a density functional theory (DFT) informed space charge model for the design of an artificial SEI consisting of lithium fluoride (LiF) and lithium carbonate (Li_2CO_3). DFT calculations have been used to compute the thermodynamics of defects in the two phases in equilibrium with electrodes[174,175] and predict possible defect reactions near the LiF/Li_2CO_3 interface. This information was then inputted to a space charge model[183] to calculate the ionic and electronic conductivity through the composite artificial SEI.

6.3 Methodology and model system

6.3.1 Interfacial defect chemistry: a revisit

The LiF and Li_2CO_3 composite coating serves as a good model system for this study. Firstly, the ionic carrier and diffusion mechanisms are very different in LiF and Li_2CO_3. It has been predicted that the Li ion interstitial is the dominant diffusion carrier in Li_2CO_3 and it transports through a "knock-off" mechanism[174]; while, in LiF, the major ionic carrier is Li ion vacancy and it diffuses via a hopping mechanism[175]. LiF is a good electronic insulator but Li_2CO_3 provides a relatively good ionic conduction on an anode surface.[174,175] Secondly, to the authors' best knowledge, the interfacial defect chemistry around LiF/Li_2CO_3 interface has not been explored though it is critical to the performance of the composite coating. For example, if Li interstitials in Li_2CO_3[174] prefer to migrate across the LiF/Li_2CO_3 to couple Li ion vacancies in LiF, this process would cause the depletion of ionic carriers and reduce the ionic conduction through the composite SEI. However, it has been shown that the mixture of LiF and Li_2CO_3 as an artificial SEI on anode surfaces can improve the rate capability and durability of the electrode.[220] This phenomenon has been rationalized by assuming that the mixture can simultaneously enhance ionic conduction and electronic insulation.[220] Our results also show that, by creating LiF/Li_2CO_3 interfaces in the artifitical SEI, the concentration of ionic carriers is promoted near the interface with the depletion of electronic carriers. Furthermore, to optimize electrical transport properties in the mixture coating on anode, we propose a structure that can maximize the interfacial effect and investigate the influences of the grain size and the volume ratio of the two components on the total electrical conduction. Our results show that the electrical conduction through the artificial SEI coating can be optimized by carefully engineering the grain size and volume fraction.

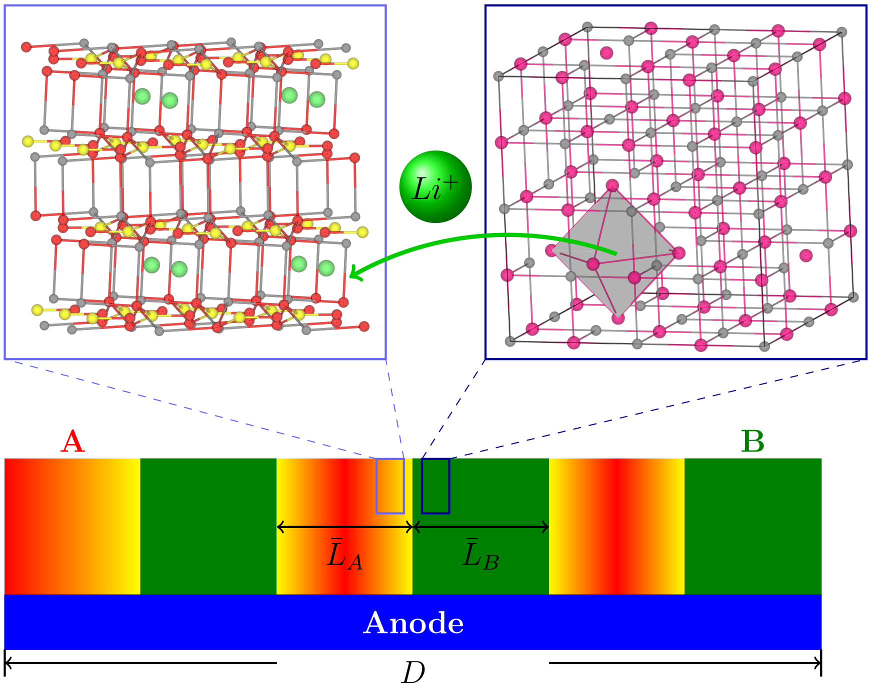

Figure 6.1: Designed artificial SEI structure coated on the electrode surface (A represents Li_2CO_3 and B represents LiF); Zoom-in (Left): crystal structure of Li_2CO_3 with Li interstitial defect (green: Li interstitial, grey: lattice Li, red: oxygen, and yellow: carbon); Zoom-in (right): crystal structure of LiF with a Li ion vacancy (magenta: fluorine and grey: lattice Li). The green arrow from the right to the left represents the defect reaction near LiF/Li_2CO_3 interface: a lattice Li ion in LiF migrates to Li_2CO_3 side forming a Li ion interstitial in Li_2CO_3 and leaving a Li ion vacancy behind in LiF.

The designed structure of SEI is an array structure with Li_2CO_3 (phase A) and LiF (phase B) grains alternately coated on the electrode surface (as shown in Figure 6.1 with a 2-D illustration). The ionic flux is parallel to the LiF/Li_2CO_3 interfaces, e.g., during lithiation, the ions travel from top, through the SEI, to the electrode at the bottom. In the past, a two-dimensional layered structure has been synthesized for various purposes.[221,222] The advantage of this structure is that: 1) it simplifies the topological distribution of the two phases; 2) this structure, with the two-phase interface parallel to the ionic conduction path, can provide the maximum ionic transport (or a theoretical upper limit).[183] As a result, this structure enables the maximum increment of ionic conduction through the designed film in terms of the topological distribution of the two phases.[183] The average grain size is $\bar{L}_A$ for Li_2CO_3 and $\bar{L}_B$ for LiF. The volume fraction (φ_V^A) of Li_2CO_3 is defined as

$$\varphi_V^A = \frac{n_A \bar{L}_A}{n_A \bar{L}_A + n_B \bar{L}_B} = \frac{n_A \bar{L}_A}{D}, \tag{6.1}$$

where $n_A(n_B)$ is the number of grains of Li_2CO_3 (LiF) and $n_A \approx n_B$ when $n_A(n_B) \gg 1$. Similarly, the volume fraction (φ_V^B) of LiF is $\varphi_V^B = \frac{n_B \bar{L}_B}{D}$.

The heterostructural LiF/Li_2CO_3 interface can influence the ionic conduction compared with those in the bulk materials.[81,176,179–181,186,223] Ionic conduction in LiF and Li_2CO_3 is determined by the concentration of charge carriers and their migration barriers.[175] Since the defect formation energy in both materials is much larger than the migration barrier, the Li ion conduction is limited by the concentration of diffusing carriers. Thus, we only considered, in this model, the influence of heterogeneous interface on the defect distribution. In addition, the defect concentration near the interface is still low enough to satisfy the dilute defect condition. Multiple physical processes can occur when two different materials are in contact[176], e.g., the lattice mismatch and the formation of a third phase. However, to a first approximation, we consider a planar abrupt interface of which the atomic structures maintain the same as those in the perfect crystal (Figure 5.3). An important physical process shall be considered near this ideal interface is defect reactions at the interface, i.e., electrochemical reaction[176]. The defect reactions depend on the type of dominant defects in the bulk materials. The dominant defect in Li_2CO_3 on anode is Li ion interstitial ($Li_i^\bullet$) and the positive charge is balanced by electrons (e$'$).[174] In LiF, the main defect is Schottky pairs, i.e., Li ion (V'_{Li}) and F ion vacancies ($V_F^\bullet$).[175] The flow of electrons across the interface is neglected, since LiF is an electronic insulator when coated on anode.[175] In addition, the migrations of fluorine and oxocarbon ion between Li_2CO_3 and LiF are neglected since these processes are energetically unfavorable. As a result, we consider the following four Li point defects related reactions:

(R1): A lattice Li ion in LiF migrates to form a $Li_i^\bullet$ in Li_2CO_3:

$$Nil \implies Li_i^\bullet(A) + V'_{Li}(B);$$

(R2): A lattice Li in Li_2CO_3 migrates to occupy a V'_{Li} in LiF (i.e., V'_{Li} migrates from LiF to Li_2CO_3):

$$V'_{Li}(B) \implies V'_{Li}(A);$$

(R3): A lattice Li in Li_2CO_3 migrates to form a $Li_i^\bullet$ in LiF:

$$Nil \implies Li_i^\bullet(B) + V'_{Li}(A);$$

(R4): A $Li_i^\bullet$ in Li_2CO_3 migrates to form a $Li_i^\bullet$ in LiF:

$$Li_i^\bullet(A) \implies Li_i^\bullet(B).$$

The change in chemical potential ($\Delta\mu$) of each reaction can be estimated from first principles calculations and only reactions with $\Delta\mu < 0$ is energetically favorable to occur across the interface. The chemical potential difference after each reaction can be written as

$$\Delta\mu = \sum_i (\Delta h_i - T\Delta s_i). \tag{6.2}$$

In Equation (6.2), Δh_i is the change of enthalpy of a defect i and can be estimated by the formation energy of a defect at the ground state

$$\Delta h_i = E_{tot}(i) - n_{Li}\mu_{Li} - E_{tot}(bulk), \tag{6.3}$$

where $E_{tot}(i)$ and $E_{tot}(bulk)$ are the calculated energies for the supercell with and without the defect i. The calculated values of $\Sigma_i \Delta h_i$ for each reaction are listed in Table 6.1.[174,175] In this study, the values of energy (e.g., $E_{tot}(i)$, $E_{tot}(bulk)$) were calculated by density functional theory (DFT) with the plane wave basis sets in the Vienna *ab initio* simulation package (VASP), as detailed in single phase calculations[55,224]. The exchange-correlation functional was approximated by the generalized gradient approximation in the Perdew-Burke-Ernzerhof flavor (GGA-PBE)[143]. Ionic potentials were mimicked by the projector-augmented-wave (PAW) potentials[144]. n_{Li} is the difference of number of Li atoms in the defected supercell compared with the perfect one. μ_{Li} is the chemical potential of Li in the electrode with which the coated material (LiF or Li_2CO_3) is in thermodynamic equilibrium. In this study, $\mu_{Li} \approx -2.02$ eV corresponding to μ_{Li} in the Li metal. In addition, $T\Delta s_i$ in Equation (6.2) can be estimated by (neglecting the contribution from vibrational entropy and assuming the dilute defect situation)

$$T\Delta s_i \approx -k_B T \ln\left(\frac{c_i}{N_s(i)}\right), \tag{6.4}$$

where c_i is the concentration of the defect i in the bulk material (Li_2CO_3 or LiF) in equilibrium with the electrode in contact with.[174,175] The values of c_i in the bulk materials were calculated by balancing the charges on all possible ionic defects and electronic carriers, i.e., holes and electrons.[174,175] $N_s(i)$ is the density of the available sites for defect i. The calculated values of $\Sigma_i T\Delta s_i$ and $\Delta\mu$ for reactions R(1) to R(4) are listed in Table 6.1. As a result, only reaction (R1) is possible at the LiF/Li_2CO_3 interface.

At equilibrium, this reaction causes the ionic carrier accumulation near the interface and a space charge potential ($\phi(x)$), as shown in Figure 5.3. It is important to

Table 6.1: Summary of calculated values of $\Delta\mu$, $\Sigma_i \Delta h_i$, and $\Sigma_i T\Delta s_i$ (eV) for each reaction from DFT

	R1	R2	R3	R4
$\Delta\mu$	-0.95	0.95	0.22	0.22
$\Sigma_i \Delta h_i$	0.86	0.76	3.09	1.47
$\Sigma_i T\Delta s_i$	1.81	-0.19	2.87	1.25

note that the space charge potential is continuous across the heterogeneous interface which allows some interfacial atomic structural details to be neglected, such as the interfacial elastic effects, higher dimensional defects, and the formation of a third phase.[176] The potential across the interface and the density of charge carriers can be linked through the Poison-Boltzmann relationship[176]

$$\frac{\partial^2 \phi(x)}{\partial x^2} = -\sum_i z_i c_i(x)/\varepsilon\varepsilon_r, \tag{6.5}$$

where $c_i(x)$ is the density of the charged defect i and z_i is the quantity of charge carried by a single defect i. At thermodynamic equilibrium, the electrochemical potential (defined as $\tilde{\mu}_{M^z} = \mu_{M^z} + ze\phi(x)$, where μ_{M^z} is the chemical potential of a defect M with charge z) is uniform

$$\sum_i \tilde{\mu}_i(x) = \tilde{\mu}_{Li_i^\bullet}(x) + \tilde{\mu}_{V'_{Li}}(x) = 0. \tag{6.6}$$

6.3.2 Defect concentration and grain size of Li_2CO_3

We consider the conductivity parallel to the interface in Li_2CO_3. According to the Nernst-Einstein relationship, the ionic conductivity is proportional to both the concentration and diffusivity of the dominant defect carrier. We assume that the transport property of accumulated defects in the space charge region of Li_2CO_3 does not change significantly with that in the bulk. The total concentration of ionic carriers ($Li_i^\bullet$) in Li_2CO_3 is[183]

$$C'_{Li_i^\bullet} = \frac{1}{\bar{L}_A}\int_0^{\bar{L}_A} c_{Li_i^\bullet}(x)\mathrm{d}x, \tag{6.7}$$

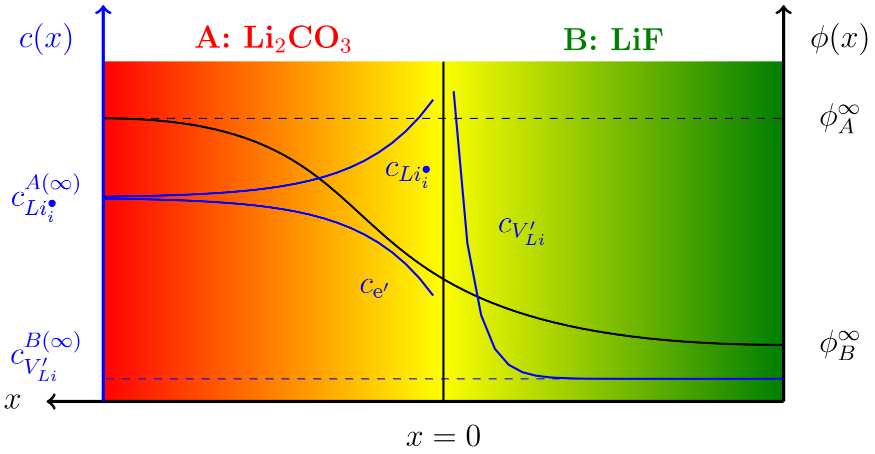

Figure 6.2: Schematic illustration of defect distribution and space charge potential across the LiF/Li_2CO_3 interface.

where $\bar{L}_A$ is the size of the Li_2CO_3 phase. As a result, the increment of defect concentration compared with bulk Li_2CO_3 can be expressed as

$$\Delta C_{Li_i^\bullet} = C'_{Li_i^\bullet} - C^\infty_{Li_i^\bullet}, \tag{6.8}$$

where $C^\infty_{Li_i^\bullet} = \int_0^{\bar{L}_A} c^\infty_{Li_i^\bullet} \mathrm{d}x = c^\infty_{Li_i^\bullet} \bar{L}_A$ is the defect concentration in the bulk. According to Nernst-Einstein relationship, the increment in ionic conductivity due to this interface is

$$\Delta\sigma = \frac{z^2 F^2 D_{Li_i^\bullet}}{RT} \Delta C_{Li_i^\bullet}. \tag{6.9}$$

The ionic conduction parallel to the Li_2CO_3/LiF interface depends on the defect chemistry near the interface and the grain size ($\bar{L}_A/2$ for 1-D approximation) of Li_2CO_3, i.e., Eq. (6.8). On the one hand, the interfacial defect effect will vanish if $\bar{L}_A \gg 4\lambda_D$ and the ionic conductivity will be dominated by the bulk properties; On the other hand, if L is too small (typically when $\bar{L}_A \ll 4\lambda_D$), the defect concentration at $\bar{L}_A/2$ is not the bulk defect concentration (Insert (b) of Fig. 3)[225]. In the following discussion, we consider a symmetric piece of Li_2CO_3 sandwiched by LiF. As a result, the defect chemistry is symmetric about $x = \bar{L}_A/2$ and the electric field vanishes at $x = \bar{L}_A/2$[225]. The electric field can be expressed by integrating the poison's equation[225]

$$\frac{\mathrm{d}Z}{\mathrm{d}\xi} = \pm(2\cosh Z - 2\cosh Z^*)^{1/2}, \tag{6.10}$$

where $Z \equiv (\phi - \phi^\infty)/k_BT$ and Z^* refers to the value of Z at $x = \bar{L}_A/2$. Replacing Z with ζ according to the relationship $Z = 2\mathrm{ln}\frac{1-\vartheta\mathrm{e}^{-\xi}}{1+\vartheta\mathrm{e}^{-\xi}}$, Eq. (6.10) reads

$$\frac{\mathrm{dln}\zeta}{\mathrm{d}\xi} = \left[(\zeta + \zeta^{-1}) - (\zeta^* + \zeta^{*-1})\right]^{1/2}. \tag{6.11}$$

Integrating Equation (6.11) from $x = 0$ to $x = \bar{L}_A/2$, the relationship between the defect concentration at $x = \bar{L}_A/2$ (ζ^*) and that at $x = 0$ (ζ_0)[225]

$$\frac{\bar{L}_A}{2\lambda_D} = 2\sqrt{\zeta^*}[\mathscr{F}(\zeta^*;\frac{\pi}{2}) - \mathscr{F}(\zeta^*;\arcsin\sqrt{\zeta_0/\zeta^*})], \tag{6.12}$$

where $\mathscr{F}(k;\chi) = \int_0^\chi \mathrm{d}\alpha(1 - k^2\sin^2\alpha)^{-1/2}$ is the elliptical integral.

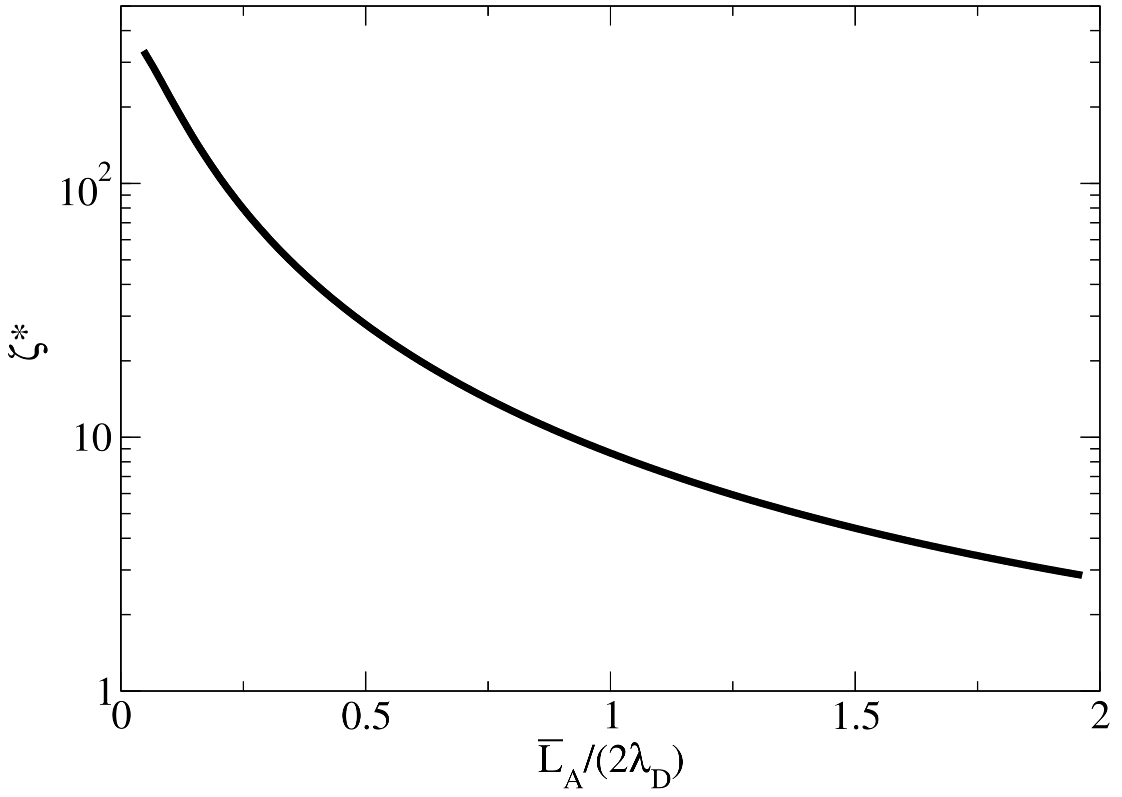

Figure 6.3: Concentration enhancement at $\bar{L}_A/2$ (ζ^*) as a function of the reduced grain size ($\frac{\bar{L}_A}{2\lambda_D}$).

According to Eq. (6.9), the increment of ionic conduction of $Li_i^\bullet$ in $\mathrm{Li_2CO_3}$ with length L can be estimated by[225]

$$\Delta\sigma_{Li_i^\bullet} = \frac{2}{\bar{L}_A}\frac{z^2F^2D_{Li_i^\bullet}}{RT}\int_0^{\bar{L}_A/2}\mathrm{d}x(c_{Li_i^\bullet}(x) - c^\infty_{Li_i^\bullet}) \tag{6.13}$$

Since there is no explicit expression for $c_{Li_i^\bullet}(x) - c^\infty_{Li_i^\bullet}$, we use the approximation $c_{Li_i^\bullet}(x) - c^\infty_{Li_i^\bullet} \approx c_{Li_i^\bullet}(x) - c'_e = \frac{\rho(x)}{zF}$[225] and insert it to Eq. (6.13)

$$\Delta\sigma_{Li_i^\bullet} \approx \frac{2}{\bar{L}_A}\frac{zFD_{Li_i^\bullet}}{RT}\int_0^{\bar{L}_A/2}\mathrm{d}x\rho(x). \tag{6.14}$$

Inserting Poisson's equation to Eq. (6.14), we have

$$\begin{aligned}\Delta\sigma_{Li_i^\bullet} &= \frac{2\varepsilon\varepsilon_r}{\bar{L}_A}\frac{zFD_{Li_i^\bullet}}{RT}\int_0^{\bar{L}_A/2}\mathrm{d}x\left[-\frac{\mathrm{d}^2\phi}{\mathrm{d}x^2}\right] \\ &= -\frac{2\varepsilon\varepsilon_r}{\bar{L}_A}\frac{zFD_{Li_i^\bullet}}{RT}\left[\left.\frac{\mathrm{d}\phi}{\mathrm{d}x}\right|_{x=\frac{\bar{L}_A}{2}} - \left.\frac{\mathrm{d}\phi}{\mathrm{d}x}\right|_{x=0}\right]\end{aligned} \tag{6.15}$$

Since the electric field vanishes at $x = \bar{L}_A/2$ by considering the symmetry, the increment of ionic conduction can be expressed as

$$\Delta\sigma_{Li_i^\bullet} \approx \frac{2\varepsilon\varepsilon_r}{\bar{L}_A}\frac{zFD_{Li_i^\bullet}}{RT}\left.\frac{\mathrm{d}\phi}{\mathrm{d}x}\right|_{x=0}. \tag{6.16}$$

Inserting Eq.(6.10) (positive solution) to Eq. (6.15), we have[225]

$$\begin{aligned}\Delta\sigma_{Li_i^\bullet} =& \frac{4\lambda_D}{\bar{L}_A}\frac{z^2F^2D_{Li_i^\bullet}}{RT}c^\infty_{Li_i^\bullet} \\ &\times\left[(\zeta_0 + \zeta_0^{-1}) - (\zeta^* + \zeta^{*-1})\right]^{1/2}.\end{aligned} \tag{6.17}$$

As a result, the increment of the ionic conduction due to the movement of $Li_i^\bullet$ depends on the defect chemistry near the interface ($x = 0$) and the defect concentration in the middle $x = \bar{L}_A/2$. Since the defect concentration ($c_{Li_i^\bullet}$) in $\mathrm{Li_2CO_3}$ near the LiF/$\mathrm{Li_2CO_3}$ interface is strongly enhanced, ζ_0^{-1} is negligible compared with ζ_0. In addition, when the grain size of $\mathrm{Li_2CO_3}$ is very small, typically $\bar{L}_A \leq 4\lambda_D$, the value of ζ^* is comparable with that of ζ_0, and thus, ζ^{*-1} can be neglected.[225] As a result, Eq. (6.17) can be simplified as

$$\Delta\sigma_{Li_i^\bullet} = \frac{4\lambda_D}{\bar{L}_A}\frac{z^2F^2D_{Li_i^\bullet}}{RT}\left[c^\infty_{Li_i^\bullet}(c^{x=0}_{Li_i^\bullet} - c^*_{Li_i^\bullet})\right]^{1/2}, \tag{6.18}$$

where $c^{x=0}_{Li_i^\bullet}$ is the concentration of $Li_i^\bullet$ at the interfacial boundary.

6.4 Results and discussion

This interfacial space charge region causes an accumulation of ionic carriers, and thus, promotes the ionic conductivity. As shown in Figure 6.2, Li lattice ions migrate from the LiF (B) side to the Li_2CO_3 (A) side forming Li ion interstitials ($Li_i^\bullet$) in Li_2CO_3 and leaving Li ion vacancies (V_{Li}') behind in LiF. For simplification, we consider LiF as an ionic and electronic insulator on the negative electrodes for the following reasons: 1) The concentration of charge carriers in bulk Li_2CO_3 and LiF varies orders of magnitude ($\frac{c_{Li_i^\bullet}(A)}{c_{V_{Li}'}(B)} \approx 10^{12}$)[174,175]; 2) The defect concentration dies out dramatically away from the interface ($c_{V_{Li}'}$ curve in Figure 6.2); 3) The transport barrier for V_{Li}' in LiF is much higher than that of $Li_i^\bullet$ in Li_2CO_3. According to the Nernst-Einstein relationship, the ionic conductivity is proportional to both the concentration and diffusivity of the dominant defect carrier. We assume that the ionic transport barrier of accumulated defects, i.e., $Li_i^\bullet$, in the space charge region does not change significantly from that in the bulk. As a result, the increment of ionic conductivity in a single Li_2CO_3 grain with size L due to the space charge effect is

$$\Delta\sigma = \frac{z^2 F^2 D_{Li_i^\bullet}}{RT} \Delta C_{Li_i^\bullet}, \tag{6.19}$$

where $\Delta C_{Li_i^\bullet} = \frac{1}{\bar{L}_A} \int_0^{\bar{L}_A} c_{Li_i^\bullet}(x) \mathrm{d}x - c_{Li_i^\bullet}^{\infty}$[183] is the total increased amount of ionic carriers in the Li_2CO_3 grain compared with that in the bulk material of the same size, F is the Faraday constant, $D_{Li_i^\bullet}$ is the diffusion coefficient of $Li_i^\bullet$ in Li_2CO_3 which is estimated from DFT calculations[174], R is the gas constant, and T is the temperature.

It is important to point out that the increment of ionic conductivity through a single Li_2CO_3 grain highly depends on the grain size ($\bar{L}_A$), as shown in Equation (6.19). The interfacial effect vanishes if $\bar{L}_A$ is too large, typically when $\bar{L}_A \gg 4\lambda_D$[217,225]. λ_D is the Debye length which is defined as[81]

$$\lambda_D = \sqrt{\frac{\varepsilon \varepsilon_r RT}{2F^2 c_{Li_i^\bullet}^{\infty}}} \tag{6.20}$$

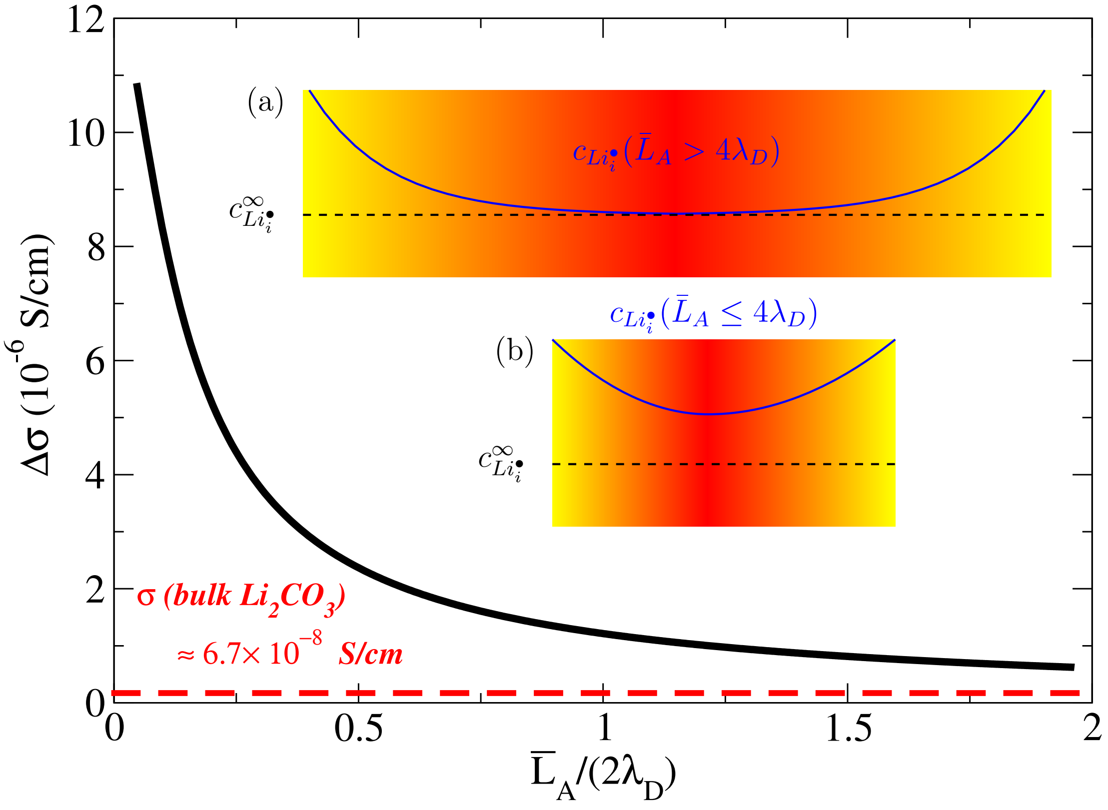

Figure 6.4: The increment of ionic conductivity as a function of the reduced average grain size of Li_2CO_3 ($\bar{L}_A/(2\lambda_D)$); Insert (a): illustration of $Li_i^\bullet$ concentration profile in Li_2CO_3 when $\bar{L}_A > 4\lambda_D$; Insert (b): illustration of $Li_i^\bullet$ concentration profile in Li_2CO_3 when $\bar{L}_A \leq 4\lambda_D$.

where $\varepsilon_r = 4.9$[187] is the relative permittivity of Li_2CO_3 and $c^\infty_{Li_i^\bullet}$ is the bulk defect concentration in Li_2CO_3. For example, $\lambda_D^{Li_2CO_3} \approx 9$ nm when Li_2CO_3 is coated on lithium metal electrode. When $\bar{L}_A \gg 4\lambda_D$, the contribution of accumulated defects near the LiF/Li_2CO_3 interfaces becomes insignificant (Insert of Figure 6.4). In our study, in order to estimate the grain size effect on the total ionic conduction, we consider Li_2CO_3 grains symmetrically sandwiched by LiF (as shown in Figure 6.1). As a result, the profile of defect concentration has a mirror symmetry about $\bar{L}_A/2$ and the increment of ionic conductivity ($\Delta\sigma_{Li_i^\bullet}(\bar{L}_A)$) depends on the defect concentration at $\bar{L}_A/2$ ($c^{*}_{Li_i^\bullet}$)

$$\Delta\sigma_{Li_i^\bullet}\left(\bar{L}_A\right) = \frac{4\lambda_D}{\bar{L}_A}\frac{z^2F^2D_{Li_i^\bullet}}{RT}\left[c^{\infty}_{Li_i^\bullet}(c^{x=0}_{Li_i^\bullet} - c^{*}_{Li_i^\bullet})\right]^{1/2}, \tag{6.21}$$

where $c^{x=0}_{Li_i^\bullet}$ is the concentration of $Li_i^\bullet$ at the LiF/Li_2CO_3 interfacial boundary. Figure 6.4 shows the dependence of $\Delta\sigma_{Li_i^\bullet}$ on the reduced average grain size of Li_2CO_3 ($\bar{L}_A/(2\lambda_D)$) when this composite material is coated on Li metal electrodes. Comparing with the ionic conductivity of Li ion in bulk Li_2CO_3 coated on Li metal electrodes ($\approx 6.7 \times 10^{-8}$ S/cm), the ionic conductivity through Li_2CO_3 can be increased by two orders of magnitude if the average grain size in the coating is less than λ_D ($\lambda_D \approx 9$ nm when coated on Li metal). This corresponds to a drop in the area specific resistance (ASR) from 1.5×10^7 Ωcm^2 to 10^5 Ωcm^2 by assuming that the one dimensional size of the electrode (D) is about 1 cm ($ASR[\Omega\text{cm}^2] = \frac{D[\text{cm}]}{\sigma[\text{S/cm}]}$).

Another important factor that influences the ionic conductivity of the LiF/Li_2CO_3 composite coating is the volume fraction. On the one hand, increasing the LiF amount would potentially increase the interface density which is beneficial to the ionic conductivity; on the other hand, LiF can play a negative role in promoting the ionic conduction due to the fact that LiF is a poor ionic conduction on anode surfaces (blocking Li ionic conduction). Assuming all the electrode surface is covered by the composite artificial SEI, i.e., $n_A\bar{L}_A + n_B\bar{L}_B = D$, the total ionic conductivity through the composite coating can be calculated by

$$\sigma = \varphi^A_V\sigma_{Li_i^\bullet}\left(\bar{L}_A\right) = (1-\varphi^B_V)\sigma_{Li_i^\bullet}\left(\bar{L}_A\right), \tag{6.22}$$

where φ^A_V (φ^B_V) is the volume fraction of Li_2CO_3 (LiF) as defined in Equation (6.1). However, Equation (6.22) can be invalid when φ^A_V approaches 1 ($\varphi^B_V \to 0$), due to the fact that the space charge effect vanishes when too little amount of LiF is in the coating (left side of Figure 6.5). In our model, we assume that the space charge effect vanishes when the average grain size of LiF ($\bar{L}_B \approx \bar{L}_A(\frac{1}{\varphi^A_V} - 1)$) diminishes to the lattice constant of LiF. The theoretical upper bound for the ionic conductivity through the composite SEI coating is controlled by the average grain size of Li_2CO_3 ($\bar{L}_A$). For a fixed value of the average grain size of Li_2CO_3 ($\bar{L}_A$), the ionic conductivity initially increases by introducing LiF into Li_2CO_3 but decreases after reaching a maximum at which the maximum density of LiF/Li_2CO_3 interface is achieved. Interestingly, the ionic conductivity can be promoted by one order of magnitude compared with that of bulk Li_2CO_3 with 90%volume of LiF when the average grain size of Li_2CO_3 is very small, e.g., $\bar{L}_A = 0.25\lambda_D$. It is because that small Li_2CO_3 grains are highly ionic conductive when $\bar{L}_A$ is below $0.5\lambda_D$ (Figure 6.4). However, the ionic conductivity can be lower than the value for the bulk Li_2CO_3 when φ_V^B is above a critical value, e.g., $\varphi_V^B > 0.9$ for $\bar{L}_A = 4\lambda_D$. It is caused by the ionic blocking effect of LiF which becomes dominant at this large φ_V^B region (right side of Figure 6.5).

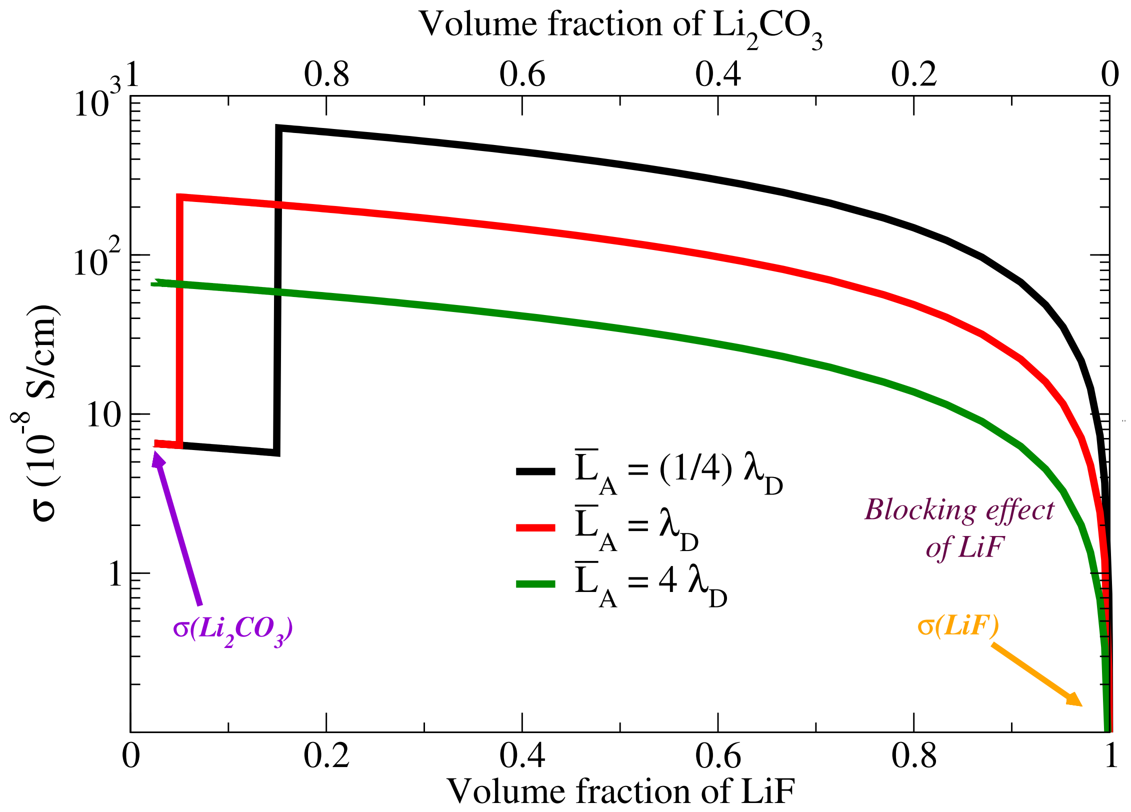

Figure 6.5: The total ionic conductivity (σ) of the LiF/Li_2CO_3 coating as a function of the volume fraction for different average grain size of Li_2CO_3.

It should be noted that the magnitude of the enhancement in ionic conduction is based on our proposed structure which provides a theoretically high ionic conduction caused by the space charge effect near the LiF/Li_2CO_3 interfaces. We realize that, in experimentally synthesized artificially SEIs or naturally formed SEIs, the nano-structure of LiF/Li_2CO_3 phases, which may be different from that described in the study, could influence the ionic conduction. For example, the orientations of LiF/Li_2CO_3 interfaces, especially when they are parallel to the electrode[226,227], would make the contribution from space charge effect to the total ionic conductivity less dramatic as described in Figure 6.5. Furthermore, if the two phases form a random nano composite structure, an approach similar to that of the Hashin's bound[228] for the sphere-based composites may be used to estimate the overall ionic conductivity. Nevertheless, interfaces that penetrate through the thin film may still be important. As a result, the current model is considered. In addition, the chemical component variation in the natural SEI could also enhance the ionic conduction. For example, Li_2EDC (dilithium ethylene carbonate), in contact with electrolyte, could cause an accumulation of Li ion and a depletion of electrons in Li_2EDC near the interface.[229] This effect would also increase the ionic conduction due to the increment in ionic carriers in the SEI but reduce the electronic conduction due to the decreased concentration of electrons in SEI. As a result, more complicated structural and chemical heterogeneity should be considered for a complete description of electrical conduction through the multi-component SEIs.

Besides the improvement in ionic conduction, this LiF/Li_2CO_3 composite artificial SEI coating can provide a better protection of electrolyte decomposition. It is believed that the leakage of electrons from the electrode to the electrolyte can cause electrolyte molecule decomposition and, leading to irreversible capacity loss.[101,194,208] The number of the electronic carriers are reduced (e.g., electrons in Li_2CO_3[174]): 1) LiF is a good electronic insulator on an anode surface with low concentration of electrons and holes;[175] 2) In the space charge region of LiF/Li_2CO_3 interface, the electron in Li_2CO_3 is depleted, as shown in Figure 6.2. As a result, the electronic leakage can be reduced due to the decreased electronic concentration which leads to a reduced electronic conductivity

$$\Delta\sigma_e = e\mu_e\Delta n_e, \tag{6.23}$$

where μ_e is the mobility of electrons which is assumed to be the same in the space charge region as in the bulk material, Δn_e is the difference in the concentration of electronic carriers compared with that of a bulk material.

6.5 Conclusions

In summary, we presented a theoretical design of a two-component artificial SEI coating based on the space charge model and density functional theory. We found that the LiF/Li_2CO_3 composite coating on an anode surface can provide an improved passivation function (reduced electron leakage) with an increased ionic conduction. This phenomenon can be attributed to defect reaction and redistribution near the LiF/Li_2CO_3 interface by forming a space charge layer. We further proposed a structure that can maximize the space charge effect. Based on this structure, we investigated the influence of two important factors, i.e., volume fraction and grain size, on the total ionic conduction. Our results suggested that ionic conduction in Li_2CO_3 can be improved by mixing the ionic insulator LiF. However, the magnitude of increment in ionic conduction depends on the grain size and the volume fraction of the two phases. The ionic conductivity can be promoted by decreasing the grain size of Li_2CO_3. With the same average grain size of Li_2CO_3, the ionic conductivity increases initially by introducing LiF into the composite SEI coating for the reason of the increased density of LiF/Li_2CO_3 interfaces. However, it decreases with further increment of LiF due to the ionic blocking effect of LiF. The knowledge is important not only to understanding the electrical conduction through the naturally formed SEI but also to providing a new insight for designing composite protective coatings on electrodes and composite solid electrolyte with high ionic conductivity.

Chapter 7 Summary and outlook

In this thesis, we have demonstrated a multiscale modeling study of ionic and electronic conduction in the Si electrode and its SEI with consideration of the multiscale physics and chemistry. The main conclusions are:

1. **Ionic transport in stressed amorphous Si electrodes**: The coupling effect between stress and lithium diffusion leads to a grand challenge to optimize the design of Si electrodes with high capacity and high rate capability, particularly considering the amorphization of Si during initial cycles. We presented a study integrating both calculations and experiments to understand the effect of stress on Li diffusion in Si electrodes. Explicit *ab initio* molecular dynamics (AIMD) simulations based on density functional theory (DFT) were performed to study the changes in structure, diffusion rates, and mechanisms in stressed Li-Si systems. Our results showed that two Li diffusion mechanisms are operating depending on the stress state. Specifically, the stress can increase Li diffusion either through increasing free volume under tension or by changing local structure under compression. Both calculation and experimental results demonstrated that diffusion coefficients vary by one order of magnitude within the range of stress generated during the lithiation and delithation process.

2. **Ionic conduction in single-component solid electrolyte coatings on electrodes**: Our results provided a new understanding of the physics of ionic transport by considering a solid electrolyte in contact with an electrode, whereas previous studies largely focused on ionic transport in stand-along solid electrolytes. Applying first principles quantum mechanics to a solid electrolyte and electrode system, we established a linkage between defect concentration, ionic

transport, and the open-circuit voltage of the electrodes. We demonstrated that, by varying the voltage of the electrode, the ionic conduction can be altered by 18 orders of magnitude in the solid electrolyte. In addition, our newly developed computational method is generally applicable to a wide range of ionic conduction problems. For example, it can be applied to predict ionic conduction in various physical systems in which defect concentrations and thus, the rate of ionic transport, are a function of an external field (e.g., chemical or electrochemical potentials).

3. **Ionic and electronic conduction in multicomponent solid electrolytes**: We investigated the effect of interfaces in SEI components (e.g., LiF/Li_2CO_3) on defect distribution, and thus, ionic and electronic conduction. Based on the bulk defect properties obtained from DFT calculations, we calculated the defect redistribution near the LiF/Li_2CO_3 interface by considering defect migration and reactions across the interface. We found that, in the ionic space charge region of Li_2CO_3 near the LiF/Li_2CO_3 interface, Li ion interstitials are accumulated but the electrons are depleted. This demonstrates a possibility that, by engineering a mixture of LiF and Li_2CO_3 in an artificial SEI, the ionic conduction can be enhanced and the electron leakage through the SEI can be reduced, thus enhancing the durability and performance of electrodes. This method can be applied to design SEI composition and structure, as well as multi-phase solid electrolytes with high ionic conductivity.

4. **Design of nanostructured heterogeneous artificial SEI coatings**: In order to help engineer an artificial SEI with optimized electrical conduction, it is necessary to study the influence of some important physical properties, e.g., grain size, volume fraction, and topological distribution of the two phases. Based on our thermodynamic data from density functional theory calculations

and space charge model, we studied the effect of grain size and volumetric ratio on the total ionic conductivity. We chose a coating structure of LiF/Li_2CO_3 with the LiF/Li_2CO_3 interfaces parallel to the transport direction of ions. Theoretically, this structure presents an upper limit of the ionic conduction through a two-components mixture. The ionic conductivity through Li_2CO_3 grain increases by decreasing the grain size. It is because that the interfacial effect that causing the accumulation of ionic carrier becomes more dominant when reducing the grain size. In addition, the total ionic conductivity benefits from moderately mixing LiF into Li_2CO_3. The optimized amount of mixing depends on the grain size of Li_2CO_3. As a result, our results predict that the optimized ionic conduction can be achieved by reducing the grain size of Li_2CO_3 and introducing moderate amount of LiF into the artificial SEI.

This research opens many opportunities to further optimize the ionic and electronic conduction in Si electrode and its SEI. For example, the defect chemistry in other components in SEI, e.g., Li_2O, is important to map the whole picture of electrical conduction through the SEI. The topological distribution of different components in SEI would also be important to determine the contribution of space charge effect to the total electrical conduction. In addition, to the development of methodology, models with consideration of more complicated physics are necessary. For instance, in our DFT informed space charge model, we assume an abrupt contact between two phases. But, in really, multiple physical processes may happen, e.g., the lattice mismatch, the formation of a third phase, and Fermi level matching (for two phases both with considerable electronic carrier concentration). In our study of the LiF/Li_2CO_3 interface, we assume that the defect reaction near the interface reaches a thermodynamic equilibrium. However, to make this DFT informed space charge model applicable to other cases, we need to consider the kinetics of ion/electron/hole transport which may be a limiting step to reach equilibrium.

Bibliography

[1] V. Etacheri, R. Marom, R. Elazari, G. Salitra, and D. Aurbach. Challenges in the development of advanced li-ion batteries: a review. *Energy Environ. Sci.*, 4(9):3243–3262, 2011.

[2] M. N. Obrovac, L. Christensen, D. B. Le, and J. R. Dahnb. Alloy design for lithium-ion battery anodes. *J. Electrochem. Soc.*, 154(9):A849–A855, 2007.

[3] L. Zhou. Progress and problems in hydrogen storage methods. *Renew. Sust. Energ. Rev.*, 9(4):395–408, 2005.

[4] R. Huggins. *Advanced Batteries: Materials Science Aspects*. SpringerLink: Springer e-Books. Springer London, Limited, 2009.

[5] S. J. Lee, J. K. Lee, S. H. Chung, H. Y. Lee, S. M. Lee, and H. K. Baik. Stress effect on cycle properties of the silicon thin-film anode. *J. Power Sources*, 97-8:191–193, 2001.

[6] P. Johari, Y. Qi, and V. B. Shenoy. The mixing mechanism during lithiation of si negative electrode in li-ion batteries: An ab lnitio molecular dynamics study. *Nano Lett.*, 11(12):5494–5500, 2011.

[7] L. Y. Beaulieu, T. D. Hatchard, A. Bonakdarpour, M. D. Fleischauer, and J. R. Dahn. Reaction of li with alloy thin films studied by in situ afm. *J. Electrochem. Soc.*, 150(11):A1457–A1464, 2003.

[8] R. A. Sharma and R. N. Seefurth. Thermodynamic properties of lithium-silicon system. *J. Electrochem. Soc.*, 123(8):C239–C239, 1976.

[9] W. Wang and P. N. Kumta. Reversible high capacity nanocomposite anodes of si/c/swnts for rechargeable li-ion batteries. *J. Power Sources*, 172(2):650–658, 2007.

[10] B. A. Boukamp, G. C. Lesh, and R. A. Huggins. All-solid lithium electrodes with mixed-conductor matrix. *J. Electrochem. Soc.*, 128(4):725–729, 1981.

[11] M. Winter and J. O. Besenhard. Rechargeable batteries. *Chem. Unserer Zeit*, 33(6):320–332, 1999.

[12] C. K. Chan, X. F. Zhang, and Y. Cui. High capacity li ion battery anodes using ge nanowires. *Nano Lett.*, 8(1):307–309, 2008.

[13] C. K. Chan, H. L. Peng, G. Liu, K. McIlwrath, X. F. Zhang, R. A. Huggins, and Y. Cui. High-performance lithium battery anodes using silicon nanowires. *Nat. Nanotechnol.*, 3(1):31–35, 2008.

[14] C. K. Chan, R. N. Patel, M. J. O'Connell, B. A. Korgel, and Y. Cui. Solution-grown silicon nanowires for lithium-ion battery anodes. *Acs Nano*, 4(3):1443–1450, 2010.

[15] K. Kang, H. S. Lee, D. W. Han, G. S. Kim, D. Lee, G. Lee, Y. M. Kang, and M. H. Jo. Maximum li storage in si nanowires for the high capacity three-dimensional li-ion battery. *Appl. Phys. Lett.*, 96(5), 2010.

[16] T. Song, J. L. Xia, J. H. Lee, D. H. Lee, M. S. Kwon, J. M. Choi, J. Wu, S. K. Doo, H. Chang, W. Il Park, D. S. Zang, H. Kim, Y. G. Huang, K. C. Hwang, J. A. Rogers, and U. Paik. Arrays of sealed silicon nanotubes as anodes for lithium ion batteries. *Nano Lett.*, 10(5):1710–1716, 2010.

[17] M. H. Park, M. G. Kim, J. Joo, K. Kim, J. Kim, S. Ahn, Y. Cui, and J. Cho. Silicon nanotube battery anodes. *Nano Lett.*, 9(11):3844–3847, 2009.

[18] H. Ma, F. Y. Cheng, J. Chen, J. Z. Zhao, C. S. Li, Z. L. Tao, and J. Liang. Nest-like silicon nanospheres for high-capacity lithium storage. *Adv. Mater.*, 19(22):4067–4070, 2007.

[19] S. H. Nam, K. S. Kim, H. S. Shim, S. H. Lee, G. Y. Jung, and W. B. Kim. Probing the lithium ion storage properties of positively and negatively carved silicon. *Nano Lett.*, 11(9):3656–3662, 2011.

[20] J. H. Lee, W. J. Kim, J. Y. Kim, S. H. Lim, and S. M. Lee. Spherical silicon/graphite/carbon composites as anode material for lithium-ion batteries. *J. Power Sources*, 176(1):353–358, 2008.

[21] Z. Y. Zeng, J. P. Tu, X. L. Wang, and X. B. Zhao. Electrochemical properties of si/liti2o2 nanocomposite as anode materials for li-ion secondary batteries. *J. Electroanal. Chem.*, 616(1-2):7–13, 2008.

[22] R. D. Deshpande, J. C. Li, Y. T. Cheng, and M. W. Verbrugge. Liquid metal alloys as self-healing negative electrodes for lithium ion batteries. *J. Electrochem. Soc.*, 158(8):A845–A849, 2011.

[23] Y. S. Jung, A. S. Cavanagh, L. A. Riley, S. H. Kang, A. C. Dillon, M. D. Groner, S. M. George, and S. H. Lee. Ultrathin direct atomic layer deposition on composite electrodes for highly durable and safe li-ion batteries. *Adv. Mater.*, 22(19):2172–+, 2010.

[24] H. Wu, G. Chan, J. W. Choi, I. Ryu, Y. Yao, M. T. McDowell, S. W. Lee, A. Jackson, Y. Yang, L. B. Hu, and Y. Cui. Stable cycling of double-walled silicon nanotube battery anodes through solid-electrolyte interphase control. *Nat. Nanotechnol.*, 7(5):309–314, 2012.

[25] M. T. McDowell, S. W. Lee, I. Ryu, H. Wu, W. D. Nix, J. W. Choi, and Y. Cui. Novel size and surface oxide effects in silicon nanowires as lithium battery anodes. *Nano Lett.*, 11(9):4018–4025, 2011.

[26] X. C. Xiao, P. Lu, and D. Ahn. Ultrathin multifunctional oxide coatings for lithium ion batteries. *Adv. Mater.*, 23(34):3911, 2011.

[27] V. Etacheri, O. Haik, Y. Goffer, G. A. Roberts, I. C. Stefan, R. Fasching, and D. Aurbach. Effect of fluoroethylene carbonate (fec) on the performance and surface chemistry of si-nanowire li-ion battery anodes. *Langmuir*, 28(1):965–976, 2012.

[28] D.A. McQuarrie. *Quantum chemistry.* University Science Books, 2008.

[29] D. Sholl and J.A. Steckel. *Density Functional Theory: A Practical Introduction.* Wiley, 2011.

[30] J. P. Perdew, K. Burke, and M. Ernzerhof. Generalized gradient approximation made simple. *Phys. Rev. Lett.*, 77(18):3865–3868, 1996.

[31] C. Kittel. *Introduction to Solid State Physics.* Wiley, 2005.

[32] H. J. Monkhorst and J. D. Pack. Special points for brillouin-zone integrations. *Phys. Rev. B*, 13(12):5188–5192, 1976.

[33] S. Nose. A molecular-dynamics method for simulations in the canonical ensemble. *Molecular Physics*, 52(2):255–268, 1984. Sv647 Times Cited:2554 Cited References Count:17.

[34] R. Mukherjee, R. Krishnan, T. M. Lu, and N. Koratkar. Nanostructured electrodes for high-power lithium ion batteries. *Nano Energy*, 1(4):518–533, 2012.

[35] M. T. McDowell, S. W. Lee, W. D. Nix, and Y. Cui. 25th anniversary article: Understanding the lithiation of silicon and other alloying anodes for lithium-ion batteries. *Adv. Mater.*, 25(36):4966–85, 2013.

[36] X. H. Wang, L. N. Sun, R. A. Susantyoko, Y. Fan, and Q. Zhang. Ultrahigh volumetric capacity lithium ion battery anodes with cnt-si film. *Nano Energy*, 8:71–77, 2014.

[37] L. B. Hu, N. Liu, M. Eskilsson, G. Y. Zheng, J. McDonough, L. Wagberg, and Y. Cui. Silicon-conductive nanopaper for li-ion batteries. *Nano Energy*, 2(1):138–145, 2013.

[38] L. Y. Beaulieu, T. D. Hatchard, A. Bonakdarpour, M. D. Fleischauer, and J. R. Dahn. Reaction of li with alloy thin films studied by in situ afm. *J. Electrochem. Soc.*, 150(11):A1457–A1464, 2003.

[39] B. A. Boukamp, G. C. Lesh, and R. A. Huggins. All-solid lithium electrodes with mixed-conductor matrix. *J. Electrochem. Soc.*, 128(4):725–729, 1981.

[40] J. C. Li, X. C. Xiao, F. Q. Yang, M. W. Verbrugge, and Y. T. Cheng. Potentiostatic intermittent titration technique for electrodes governed by diffusion and interfacial reaction. *J. Phys. Chem. C*, 116(1):1472–1478, 2012.

[41] N. Ding, J. Xu, Y. X. Yao, G. Wegner, X. Fang, C. H. Chen, and I. Lieberwirth. Determination of the diffusion coefficient of lithium ions in nano-si. *Solid State Ionics*, 180(2-3):222–225, 2009.

[42] J. Xie, N. Imanishi, T. Zhang, A. Hirano, Y. Takeda, and O. Yamamoto. Li-ion diffusion in amorphous si films prepared by rf magnetron sputtering: A comparison of using liquid and polymer electrolytes. *Mater. Chem. Phys.*, 120(2-3):421–425, 2010.

[43] N. Balke, S. Jesse, Y. Kim, L. Adamczyk, A. Tselev, I. N. Ivanov, N. J. Dudney, and S. V. Kalinin. Real space mapping of li-ion transport in amorphous si anodes with nanometer resolution. *Nano Lett.*, 10(9):3420–3425, 2010.

[44] M. T. McDowell, S. W. Lee, C. M. Wang, and Y. Cui. The effect of metallic coatings and crystallinity on the volume expansion of silicon during electrochemical lithiation/delithiation. *Nano Energy*, 1(3):401–410, 2012.

[45] Tzu-Liang Chan and James R Chelikowsky. Controlling diffusion of lithium in silicon nanostructures. *Nano Lett.*, 10(3):821–825, 2010.

[46] Y. Z. Fu and A. Manthiram. Silicon nanoparticles supported on graphitic carbon paper as a hybrid anode for li-ion batteries. *Nano Energy*, 2(6):1107–1112, 2013.

[47] V. A. Sethuraman, V. Srinivasan, A. F. Bower, and P. R. Guduru. In situ measurements of stress-potential coupling in lithiated silicon. *J. Electrochem. Soc.*, 157(11):A1253–A1261, 2010.

[48] S. K. Soni, B. W. Sheldon, X. C. Xiao, M. W. Verbrugge, D. Ahn, H. Haftbaradaran, and H. J. Gao. Stress mitigation during the lithiation of patterned amorphous si islands. *J. Electrochem. Soc.*, 159(1):A38–A43, 2012.

[49] F. Faupel, W. Frank, M. P. Macht, H. Mehrer, Naundorf V, K. Ratzke, H. R. Schober, S. K. Sharma, and H. Teichler. Diffusion in metallic glasses and supercooled melts. *Rev. Mod. Phys.*, 75(1):237–280, 2003.

[50] I. Kushiro. Changes in viscosity and structure of melt of naalsi2o6 composition at high-pressures. *J. Geophys. Res.*, 81(35):6347–6350, 1976.

[51] S. D. Theiss, F. Spaepen, and M. J. Aziz. Pressure-enhanced interdiffusion in amorphous si/ge multilayers. *Appl. Phys. Lett.*, 68(9):1226–1228, 1996.

[52] P. Klugkist, K. Ratzke, S. Rehders, P. Troche, and F. Faupel. Activation volume of co-57 diffusion in amorphous co81zr19. *Phys. Rev. Lett.*, 80(15):3288–3291, 1998.

[53] P. Klugkist, K. Ratzke, and F. Faupel. Evidence of defect-mediated zirconium self-diffusion in amorphous co92zr8. *Phys. Rev. Lett.*, 81(3):614–617, 1998.

[54] G. Kresse and J. Furthmüller. Efficient iterative schemes for ab initio total-energy calculations using a plane-wave basis set. *Phys. Rev. B*, 54:11169–11186, Oct 1996.

[55] G. Kresse and J. Furthmuller. Efficiency of ab-initio total energy calculations for metals and semiconductors using a plane-wave basis set. *Comp. Mater. Sci.*, 6(1):15–50, 1996.

[56] G. Kresse and D. Joubert. From ultrasoft pseudopotentials to the projector augmented-wave method. *Phys. Rev. B*, 59(3):1758–1775, 1999.

[57] H Okamoto. Li-si (lithium-silicon). *J. Phase Equilib. Diff.*, 30(1):118–119, 2009.

[58] V. B. Shenoy, P. Johari, and Y. Qi. Elastic softening of amorphous and crystalline li-si phases with increasing li concentration: A first-principles study. *J. Power Sources*, 195(19):6825–6830, 2010.

[59] C. John Wen and Robert A. Huggins. Chemical diffusion in intermediate phases in the lithium-tin system. *J. Solid State Chem.*, 35(3):376–384, 1980.

[60] Juchuan Li, Xingcheng Xiao, Yang-Tse Cheng, and Mark W. Verbrugge. Atomic layered coating enabling ultrafast surface kinetics at silicon electrodes in lithium ion batteries. *J. Phys. Chem. Lett.*, 0(0):3387–3391, 2013.

[61] V. A. Sethuraman, M. J. Chon, M. Shimshak, V. Srinivasan, and P. R. Guduru. In situ measurements of stress evolution in silicon thin films during electrochemical lithiation and delithiation. *J. Power Sources*, 195(15):5062–5066, 2010.

[62] B. W. Sheldon, S. K. Soni, X. C. Xiao, and A. Tokranov. Thickness effects on the lithiation of amorphous silicon thin films. *Scr. Mater.*, 64(4):307–310, 2011.

[63] S. K. Soni, B. W. Sheldon, X. C. Xiao, A. F. Bower, and M. W. Verbrugge. Diffusion mediated lithiation stresses in si thin film electrodes. *J. Electrochem. Soc.*, 159(9):A1520–A1527, 2012.

[64] L.B. Freund and S. Suresh. *Thin film materials: stress, defect formation and surface evolution*. Cambridge University Press, 2004.

[65] Maria K. Y. Chan, C. Wolverton, and Jeffrey P. Greeley. First principles simulations of the electrochemical lithiation and delithiation of faceted crystalline silicon. *J. Am. Chem. Soc.*, 134(35):14362–14374, 2012.

[66] W. Tang, E. Sanville, and G. Henkelman. A grid-based bader analysis algorithm without lattice bias. *J. Phys.: Condens. Matter*, 21(8):084204, 2009.

[67] E. Sanville, S. D. Kenny, R. Smith, and G. Henkelman. Improved grid-based algorithm for bader charge allocation. *J. Comput. Chem.*, 28(5):899–908, 2007.

[68] G. Henkelman, A. Arnaldsson, and H. Jonsson. A fast and robust algorithm for bader decomposition of charge density. *Comp. Mater. Sci.*, 36(3):354–360, 2006.

[69] B. Key, M. Morcrette, J. M. Tarascon, and C. P. Grey. Pair distribution function analysis and solid state nmr studies of silicon electrodes for lithium ion batteries: Understanding the (de)lithiation mechanisms. *J. Am. Chem. Soc.*, 133(3):503–512, 2011.

[70] Arndt-Hendrik Zinn, Sara Borhani-Haghighi, Edgar Ventosa, Janine Pfetzing-Micklich, Nikolai Wieczorek, Wolfgang Schuhmann, and Alfred Ludwig. Mechanical properties of silixthin films at different stages of electrochemical li insertion. *Phys. Status Solidi a*, 211(11):2650–2656, 2014.

[71] J. R. Chelikowsky, J. J. Derby, V. V. Godlevsky, M. Jain, and J. Y. Raty. Ab initio simulations of liquid semiconductors using the pseudopotential-density functional method. *J. Phys.: Condens. Mat.*, 13(41):R817–R854, 2001.

[72] J. C. Li, A. K. Dozier, Y. C. Li, F. Q. Yang, and Y. T. Cheng. Crack pattern formation in thin film lithium-ion battery electrodes. *J. Electrochem. Soc.*, 158(6):A689–A694, 2011.

[73] Z. D. Zeng, N. Liu, Q. S. Zeng, Y. Ding, S. X. Qu, Y. Cui, and W. L. Mao. Elastic moduli of polycrystalline li15si4 produced in lithium ion batteries. *J. Power Sources*, 242:732–735, 2013.

[74] V. L. Chevrier, J. W. Zwanziger, and J. R. Dahn. First principles studies of silicon as a negative electrode material for lithium-ion batteries. *Can. J. Phys.*, 87(6):625–632, 2009.

[75] Hyunwoo Kim, Chia-Yun Chou, John G. Ekerdt, and Gyeong S. Hwang. Structure and properties of li-si alloys: A first-principles study. *J. Phys. Chem. C*, 115(5):2514–2521, 2011.

[76] H. S. Waff. Pressure-induced coordination changes in magmatic liquids. *Geophys. Res. Lett.*, 2(5):193–196, 1975.

[77] V. L. Chevrier, J. W. Zwanziger, and J. R. Dahn. First principles study of li-si crystalline phases: Charge transfer, electronic structure, and lattice vibrations. *J. Alloy. Compd.*, 496(1-2):25–36, 2010.

[78] K. J. Zhao, G. A. Tritsaris, M. Pharr, W. L. Wang, O. Okeke, Z. G. Suo, J. J. Vlassak, and E. Kaxiras. Reactive flow in silicon electrodes assisted by the insertion of lithium. *Nano Lett.*, 12(8):4397–4403, 2012.

[79] P.G. Shewmon. *Diffusion in solids*. McGraw-Hill series in materials science and engineering. McGraw-Hill, 1963.

[80] N.W. Ashcroft and N.D. Mermin. *Solid state physics*. Science: Physics. Saunders College, 1976.

[81] J. Maier. *Physical Chemistry of Ionic Materials: Ions and Electrons in Solids*. Wiley, 2004.

[82] Kazunori Takada. Progress and prospective of solid-state lithium batteries. *Acta Mater.*, 61(3):759–770, 2013.

[83] F. A. Kroger and H. J. Vink. Relations between the concentrations of imperfections in crystalline solids. *Solid State Phys.*, 3:307–435, 1956.

[84] R.A. Swalin. *Thermodynamics of Solids*. A Wiley-Interscience publication. Wiley, 1972.

[85] R. Huggins. *Advanced Batteries: Materials Science Aspects*. SpringerLink: Springer e-Books. Springer, 2008.

[86] Z. Liu, W. Fu, E. A. Payzant, X. Yu, Z. Wu, N. J. Dudney, J. Kiggans, K. Hong, A. J. Rondinone, and C. Liang. Anomalous high ionic conductivity of nanoporous beta-li3ps4. *J. Am. Chem. Soc.*, 135(3):975–978, 2013.

[87] N. Kamaya, K. Homma, Y. Yamakawa, M. Hirayama, R. Kanno, M. Yonemura, T. Kamiyama, Y. Kato, S. Hama, K. Kawamoto, and A. Mitsui. A lithium superionic conductor. *Nat. Mater.*, 10(9):682–6, 2011.

[88] N. D. Lepley, N. A. W. Holzwarth, and Yaojun A. Du. Structures, li$^+$ mobilities, and interfacial properties of solid electrolytes li$_3$ps$_4$ and li$_3$po$_4$ from first principles. *Phys. Rev. B*, 88:104103, Sep 2013.

[89] Yifei Mo, Shyue Ping Ong, and Gerbrand Ceder. First principles study of the li10gep2s12lithium super ionic conductor material. *Chem. Mater.*, 24(1):15–17, 2012.

[90] Yaojun A. Du and N. A. W. Holzwarth. Mechanisms of li$^+$ diffusion in crystalline γ- and β-li$_3$Po$_4$ electrolytes from first principles. *Phys. Rev. B*, 76:174302, Nov 2007.

[91] Yaojun A. Du and N. A. W. Holzwarth. First-principles study of lipon and related solid electrolytes. *Phys. Rev. B*, 81:184106, May 2010.

[92] Yaojun A. Du and N. A. W. Holzwarth. Effects of o vacancies and n or si substitutions on li$^+$ migration in li$_3$po$_4$ electrolytes from first principles. *Phys. Rev. B*, 78:174301, Nov 2008.

[93] Y. J. A. Du and N. A. W. Holzwarth. Li ion diffusion mechanisms in the crystalline electrolyte gamma-li3po4. *J. Electrochem. Soc.*, 154(11):A999–A1004, 2007.

[94] Juchuan Li, Cheng Ma, Miaofang Chi, Chengdu Liang, and Nancy J. Dudney. Lithium-ion batteries: Solid electrolyte: the key for high-voltage lithium batteries (adv. energy mater. 4/2015). *Adv. Energy Mater.*, 5(4):1401408, 2015.

[95] D. Aurbach. Review of selected electrode-solution interactions which determine the performance of li and li ion batteries. *J. Power Sources*, 89(2):206–218, 2000.

[96] P. Verma, P. Maire, and P. Novak. A review of the features and analyses of the solid electrolyte interphase in li-ion batteries. *Electrochim. Acta*, 55(22):6332–6341, 2010.

[97] S. Q. Hao and C. Wolverton. Lithium transport in amorphous al2o3 and alf3 for discovery of battery coatings. *J. Phys. Chem. C*, 117(16):8009–8013, 2013.

[98] S. Q. Shi, P. Lu, Z. Y. Liu, Y. Qi, L. G. Hector, H. Li, and S. J. Harris. Direct calculation of li-ion transport in the solid electrolyte interphase. *J. Am. Chem. Soc.*, 134(37):15476–15487, 2012.

[99] S. Q. Shi, Y. Qi, H. Li, and L. G. Hector. Defect thermodynamics and diffusion mechanisms in li2co3 and implications for the solid electrolyte interphase in li-ion batteries. *J. Phys. Chem. C*, 117(17):8579–8593, 2013.

[100] K. Leung and J. L. Budzien. Ab initio molecular dynamics simulations of the initial stages of solid-electrolyte interphase formation on lithium ion battery graphitic anodes. *Phys. Chem. Chem. Phys.*, 12(25):6583–6586, 2010.

[101] Kevin Leung. Electronic structure modeling of electrochemical reactions at electrode/electrolyte interfaces in lithium ion batteries. *J. Phys. Chem. C*, 117:1539–1547, 2013.

[102] K. Leung, Y. Qi, K. R. Zavadil, Y. S. Jung, A. C. Dillon, A. S. Cavanagh, S. H. Lee, and S. M. George. Using atomic layer deposition to hinder solvent decomposition in lithium ion batteries: First-principles modeling and experimental studies. *J. Am. Chem. Soc.*, 133(37):14741–14754, 2011.

[103] Q. L. Zhang, X. C. Xiao, Y. T. Cheng, and M. W. Verbrugge. A non-destructive method for measuring the mechanical properties of ultrathin films prepared by atomic layer deposition. *Appl. Phys. Lett.*, 105(6), 2014.

[104] H. Wu, G. Chan, J. W. Choi, I. Ryu, Y. Yao, M. T. McDowell, S. W. Lee, A. Jackson, Y. Yang, L. B. Hu, and Y. Cui. Stable cycling of double-walled silicon nanotube battery anodes through solid-electrolyte interphase control. *Nat. Nanotechnol.*, 7(5):309–314, 2012.

[105] M. N. Obrovac, L. Christensen, D. B. Le, and J. R. Dahnb. Alloy design for lithium-ion battery anodes. *J. Electrochem. Soc.*, 154(9):A849–A855, 2007.

[106] L. Y. Beaulieu, K. W. Eberman, R. L. Turner, L. J. Krause, and J. R. Dahn. Colossal reversible volume changes in lithium alloys. *Electrochem. Solid St.*, 4(9):A137–A140, 2001.

[107] T. D. Hatchard and J. R. Dahn. In situ xrd and electrochemical study of the reaction of lithium with amorphous silicon. *J. Electrochem. Soc.*, 151(6):A838–A842, 2004.

[108] T. Song, J. L. Xia, J. H. Lee, D. H. Lee, M. S. Kwon, J. M. Choi, J. Wu, S. K. Doo, H. Chang, W. Il Park, D. S. Zang, H. Kim, Y. G. Huang, K. C. Hwang, J. A. Rogers, and U. Paik. Arrays of sealed silicon nanotubes as anodes for lithium ion batteries. *Nano Lett.*, 10(5):1710–1716, 2010.

[109] L. Y. Beaulieu, T. D. Hatchard, A. Bonakdarpour, M. D. Fleischauer, and J. R. Dahn. Reaction of li with alloy thin films studied by in situ afm. *J. Electrochem. Soc.*, 150(11):A1457–A1464, 2003.

[110] X. C. Xiao, P. Lu, and D. Ahn. Ultrathin multifunctional oxide coatings for lithium ion batteries. *Adv. Mater.*, 23(34):3911–3915, 2011.

[111] Y. S. Jung, A. S. Cavanagh, L. A. Riley, S. H. Kang, A. C. Dillon, M. D. Groner, S. M. George, and S. H. Lee. Ultrathin direct atomic layer deposition on composite electrodes for highly durable and safe li-ion batteries. *Adv. Mater.*, 22(19):2172–2176, 2010.

[112] Zonghai Chen, Yan Qin, Khalil Amine, and Y.-K. Sun. Role of surface coating on cathode materials for lithium-ion batteries. *J. Mater. Chem.*, 20:7606–7612, 2010.

[113] D. W. Liu and G. Z. Cao. Engineering nanostructured electrodes and fabrication of film electrodes for efficient lithium ion intercalation. *Energ. Environ. Sci.*, 3(9):1218–1237, 2010.

[114] S. S. Zhang. A review on electrolyte additives for lithium-ion batteries. *J. Power Sources*, 162(2):1379–1394, 2006.

[115] K. Yang, L. Z. Fan, J. Guo, and X. H. Qu. Significant improvement of electrochemical properties of alf3-coated lini0.5co0.2mn0.3o2 cathode materials. *Electrochim. Acta*, 63:363–368, 2012.

[116] Y. Q. Wang, L. Guo, Y. G. Guo, H. Li, X. Q. He, S. Tsukimoto, Y. Ikuhara, and L. J. Wan. Rutile-tio2 nanocoating for a high-rate li4ti5o12 anode of a lithium-ion battery. *J. Am. Chem. Soc.*, 134(18):7874–7879, 2012.

[117] L. B. Chen, K. Wang, X. H. Xie, and J. Y. Xie. Enhancing electrochemical performance of silicon film anode by vinylene carbonate electrolyte additive. *Electrochem. Solid St.*, 9(11):A512–A515, 2006.

[118] L. B. Chen, K. Wang, X. H. Xie, and J. Y. Xie. Effect of vinylene carbonate (vc) as electrolyte additive on electrochemical performance of si film anode for lithium ion batteries. *J. Power Sources*, 174(2):538–543, 2007.

[119] Mengyun Nie, Dinesh Chalasani, Daniel P. Abraham, Yanjing Chen, Arijit Bose, and Brett L. Lucht. Lithium ion battery graphite solid electrolyte interphase revealed by microscopy and spectroscopy. *J. Phys. Chem. C*, 117(3):1257–1267, 2013.

[120] R. Elazari, G. Salitra, G. Gershinsky, A. Garsuch, A. Panchenko, and D. Aurbach. Li ion cells comprising lithiated columnar silicon film anodes, tis2 cathodes and fluoroethyene carbonate (fec) as a critically important component. *J. Electrochem. Soc.*, 159(9):A1440–A1445, 2012.

[121] V. Etacheri, O. Haik, Y. Goffer, G. A. Roberts, I. C. Stefan, R. Fasching, and D. Aurbach. Effect of fluoroethylene carbonate (fec) on the performance and surface chemistry of si-nanowire li-ion battery anodes. *Langmuir*, 28(1):965–976, 2012.

[122] K. Fridman, R. Sharabi, R. Elazari, G. Gershinsky, E. Markevich, G. Salitra, D. Aurbach, A. Garsuch, and J. Lampert. A new advanced lithium ion battery: Combination of high performance amorphous columnar silicon thin film anode, 5 v lini0.5mn1.5o4 spinel cathode and fluoroethylene carbonate-based electrolyte solution. *Electrochem. Commun.*, 33:31–34, 2013.

[123] E. Markevich, K. Fridman, R. Sharabi, R. Elazari, G. Salitra, H. E. Gottlieb, G. Gershinsky, A. Garsuch, G. Semrau, M. A. Schmidt, and D. Aurbach. Amorphous columnar silicon anodes for advanced high voltage lithium ion full cells: Dominant factors governing cycling performance. *J. Electrochem. Soc.*, 160(10):A1824–A1833, 2013.

[124] M. Y. Nie, D. P. Abraham, Y. J. Chen, A. Bose, and B. L. Lucht. Silicon solid electrolyte interphase (sei) of lithium ion battery characterized by microscopy and spectroscopy. *J. Phys. Chem. C*, 117(26):13403–13412, 2013.

[125] I. A. Profatilova, C. Stock, A. Schmitz, S. Passerini, and M. Winter. Enhanced thermal stability of a lithiated nano-silicon electrode by fluoroethylene carbonate and vinylene carbonate. *J. Power Sources*, 222:140–149, 2013.

[126] G. A. Baraff and M. Schlüter. Electronic structure, total energies, and abundances of the elementary point defects in gaas. *Phys. Rev. Lett.*, 55:1327–1330, Sep 1985.

[127] W. Shockley and J. L. Moll. Solubility of flaws in heavily-doped semiconductors. *Phys. Rev.*, 119:1480–1482, Sep 1960.

[128] W. Walukiewicz. Amphoteric native defects in semiconductors. *Appl. Phys. Lett.*, 54(21):2094–2096, 1989.

[129] B. P. R. Marioton and U. GÃűsele. Transport of thermodynamic information by selfâĂŘinterstitials between precipitates in silicon. *J. Appl. Phys.*, 63(9):4661–4668, 1988.

[130] S. B. Zhang and John E. Northrup. Chemical potential dependence of defect formation energies in gaas: Application to ga self-diffusion. *Phys. Rev. Lett.*, 67(17):2339–2342, 1991.

[131] D. B. Laks, C. G. Van de Walle, G. F. Neumark, P. E. Blöchl, and S. T. Pantelides. Native defects and self-compensation in znse. *Phys. Rev. B*, 45:10965–10978, May 1992.

[132] Jun-Liang Zhao, Wenqing Zhang, Xiao-Min Li, Ji-Wei Feng, and Xun Shi. Convergence of the formation energies of intrinsic point defects in wurtzite zno: first-principles study by projector augmented wave method. *J. Phys.: Condens. Matter*, 18(5):1495–1508, 2006.

[133] Jörg Neugebauer and Chris G. Van de Walle. Atomic geometry and electronic structure of native defects in gan. *Phys. Rev. B*, 50(11):8067–8070, 1994.

[134] Chris G. Van de Walle and Jörg Neugebauer. First-principles calculations for defects and impurities: Applications to iii-nitrides. *J. Appl. Phys.*, 95(8):3851, 2004.

[135] Q. L. Zhang, X. C. Xiao, W. D. Zhou, Y. T. Cheng, and M. W. Verbrugge. Towards high cycle efficiency of silicon-based negative electrodes by designing solid electrolyte interphase. *Adv. Energy Mater.*, 5:1401398, 2015.

[136] D. M. Roessler and W. C. Walker. Electronic spectrum of crystalline lithium fluoride. *J. Phys. Chem. Solids*, 28(8):1507–1515, 1967.

[137] R. C. Chaney, E. E. Lafon, and C. C. Lin. Energy band structure of lithium fluoride crystals by method of tight binding. *Phys. Rev. B*, 4(8):2734–2741, 1971.

[138] M. Piacentini, D. W. Lynch, and C. G. Olson. Thermoreflectance of lif between 12 and 30 ev. *Phys. Rev. B*, 13:5530–5543, Jun 1976.

[139] J. B. Goodenough and Y. Kim. Challenges for rechargeable li batteries. *Chemistry of Materials*, 22(3):587–603, 2010.

[140] A. Van der Ven, G. Ceder, M. Asta, and P. D. Tepesch. First-principles theory of ionic diffusion with nondilute carriers. *Phys. Rev. B*, 64(18):184307, 2001.

[141] G. Dolling, H. Smith, R. Nicklow, P. Vijayaraghavan, and M. Wilkinson. Lattice dynamics of lithium fluoride. *Phys. Rev.*, 168(3):970–979, 1968.

[142] C. A. Sholl. Diffusion correlation factors and atomic displacements for the vacancy mechanism. *J. Phys. C*, 14(20):2723–2729, 1981.

[143] John P. Perdew, Kieron Burke, and Matthias Ernzerhof. Generalized gradient approximation made simple. *Phys. Rev. Lett.*, 77:3865–3868, Oct 1996.

[144] G. Kresse and D. Joubert. From ultrasoft pseudopotentials to the projector augmented-wave method. *Phys. Rev. B*, 59:1758–1775, Jan 1999.

[145] D.B. Sirdeshmukh, L. Sirdeshmukh, and K.G. Subhadra. *Alkali Halides: A Handbook of Physical Properties*. Materials Science Series. Springer, 2001.

[146] C. A. Hutchison and H. L. Johnston. Determination of crystal densities by the temperature of flotation method. density and lattice constant of lithium fluoride. *J. Am. Chem. Soc.*, 62:3165–3168, 1940.

[147] Ryan M. Jacobs, John H. Booske, and Dane Morgan. Intrinsic defects and conduction characteristics of sc_2o_3 in thermionic cathode systems. *Phys. Rev. B*, 86:054106, Aug 2012.

[148] S. Lany and A. Zunger. Accurate prediction of defect properties in density functional supercell calculations. *Modell. Simul. Mater. Sci. Eng.*, 17(8):084002, 2009.

[149] G. Makov and M. C. Payne. Periodic boundary conditions in ab initio calculations. *Phys. Rev. B*, 51:4014–4022, Feb 1995.

[150] Jörg Neugebauer and Matthias Scheffler. Adsorbate-substrate and adsorbate-adsorbate interactions of na and k adlayers on al(111). *Phys. Rev. B*, 46:16067–16080, Dec 1992.

[151] M. Leslie and M. J. Gillan. The energy and elastic dipole tensor of defects in ionic-crystals calculated by the supercell method. *J. Phys. C Solid State*, 18(5):973–982, 1985.

[152] G. Henkelman and H. Jonsson. Improved tangent estimate in the nudged elastic band method for finding minimum energy paths and saddle points. *J. Chem. Phys.*, 113(22):9978–9985, 2000.

[153] G. Henkelman, B. P. Uberuaga, and H. Jonsson. A climbing image nudged elastic band method for finding saddle points and minimum energy paths. *J. Chem. Phys.*, 113(22):9901–9904, 2000.

[154] R. W. Godby, M. Schlüter, and L. J. Sham. Accurate exchange-correlation potential for silicon and its discontinuity on addition of an electron. *Phys. Rev. Lett.*, 56:2415–2418, Jun 1986.

[155] Patrick Rinke, Anderson Janotti, Matthias Scheffler, and Chris G. Van de Walle. Defect formation energies without the band-gap problem: Combining density-functional theory and the *gw* approach for the silicon self-interstitial. *Phys. Rev. Lett.*, 102:026402, Jan 2009.

[156] R. M. Nieminen. Positrons in alkali-halides. *J. Phys. C Solid State*, 8(13):2077–2084, 1975.

[157] Y. Haven. The ionic conductivity of li-halide crystals. *Recl. Trav. Chim. Pay.-B.*, 69(12):1471–1489, 1950.

[158] T. G. Stoebe and R. A. Huggins. Measurement of ionic diffusion in lithium fluoride by nuclear magnetic resonance techniques. *J. Mater. Sci.*, 1(2):117–126, 1966.

[159] S. Pizzini. Ionic conductivity in lithium compounds. *J. Appl. Electrochem.*, 1(3):153–161, 1971.

[160] R. W. Dreyfus and A. S. Nowick. Ionic conductivity of doped nacl crystals. *Phys. Rev.*, 126:1367–1377, May 1962.

[161] O. S. Spencer. Formation energy of individual cation vacancies in lif and nacl. *J. Appl. Phys.*, 40(1):168, 1969.

[162] A.D. McNaught, A. Wilkinson, International Union of Pure, and Applied Chemistry. *Compendium of Chemical Terminology: IUPAC Recommendations*. IUPAC Chemical Data Series. Blackwell Science, 1997.

[163] K. Xu. Electrolytes and interphases in li-ion batteries and beyond. *Chem. Rev.*, 114(23):11503–618, 2014.

[164] M Winter. The solid electrolyte interphase - the most important and the least understood solid electrolyte in rechargeable li batteries. *Z. Phys. Chem.*, 223:1395–1406, 2009.

[165] Shiqiang Hao and C. Wolverton. Lithium transport in amorphous al2o3 and alf3 for discovery of battery coatings. *J. Phys. Chem. C*, 117(16):8009–8013, 2013.

[166] Qinglin Zhang, Xingcheng Xiao, Weidong Zhou, Yang-Tse Cheng, and Mark W. Verbrugge. Toward high cycle efficiency of silicon-based negative electrodes by designing the solid electrolyte interphase. *Adv. Energy Mater.*, 5(5):1401398, 2015. 1401398.

[167] H. Sahan, H. Goktepe, and S. Patat. A novel method to improve the electrochemical performance of limn2o4 cathode active material by caco3 surface coating. *J. Mater. Sci. Technol.*, 27(5):415–420, 2011.

[168] K. Yang, L. Z. Fan, J. Guo, and X. H. Qu. Significant improvement of electrochemical properties of alf3-coated lini0.5co0.2mn0.3o2 cathode materials. *Electrochim. Acta*, 63:363–368, 2012.

[169] V. Etacheri, O. Haik, Y. Goffer, G. A. Roberts, I. C. Stefan, R. Fasching, and D. Aurbach. Effect of fluoroethylene carbonate (fec) on the performance and surface chemistry of si-nanowire li-ion battery anodes. *Langmuir*, 28(1):965–976, 2012.

[170] I. A. Profatilova, C. Stock, A. Schmitz, S. Passerini, and M. Winter. Enhanced thermal stability of a lithiated nano-silicon electrode by fluoroethylene carbonate and vinylene carbonate. *J. Power Sources*, 222:140–149, 2013.

[171] M. Y. Nie, D. P. Abraham, Y. J. Chen, A. Bose, and B. L. Lucht. Silicon solid electrolyte interphase (sei) of lithium ion battery characterized by microscopy and spectroscopy. *J. Phys. Chem. C*, 117(26):13403–13412, 2013.

[172] K. W. Schroder, H. Celio, L. J. Webb, and K. J. Stevenson. Examining solid electrolyte interphase formation on crystalline silicon electrodes: Influence of electrochemical preparation and ambient exposure conditions. *J. Phys. Chem. C*, 116(37):19737–19747, 2012.

[173] K. Xu. Nonaqueous liquid electrolytes for lithium-based rechargeable batteries. *Chem. Rev.*, 104(10):4303–4417, 2004.

[174] S. Q. Shi, Y. Qi, H. Li, and L. G. Hector. Defect thermodynamics and diffusion mechanisms in li2co3 and implications for the solid electrolyte interphase in li-ion batteries. *J. Phys. Chem. C*, 117(17):8579–8593, 2013.

[175] Jie Pan, Yang-Tse Cheng, and Yue Qi. General method to predict voltage-dependent ionic conduction in a solid electrolyte coating on electrodes. *Phys. Rev. B*, 91:134116, Apr 2015.

[176] J. Maier. Ionic-conduction in-space charge regions. *Prog. Solid State Chem.*, 23(3):171–263, 1995.

[177] A. Bunde, W. Dieterich, and E. Roman. Dispersed ionic conductors and percolation theory. *Phys. Rev. Lett.*, 55(1):5–8, 1985.

[178] C. C. Liang. Conduction characteristics of lithium iodide aluminum oxide solid electrolytes. *J. Electrochem. Soc.*, 120(10):1289–1292, 1973.

[179] N. Sata, K. Eberman, K. Eberl, and J. Maier. Mesoscopic fast ion conduction in nanometre-scale planar heterostructures. *Nature*, 408(6815):946–949, 2000.

[180] Chilin Li and Joachim Maier. Ionic space charge effects in lithium fluoride thin films. *Solid State Ionics*, 225:408–411, 2012.

[181] Chilin Li, Xiangxin Guo, Lin Gu, Dominik Samuelis, and Joachim Maier. Ionic space-charge depletion in lithium fluoride thin films on sapphire (0001) substrates. *Adv. Funct. Mater.*, 21(15):2901–2905, 2011.

[182] Jie Pan, Qinglin Zhang, Xingcheng Xiao, Yang-Tse Cheng, and Yue Qi. Design of nanostructured heterogeneous solid ionic coatings through a multiscale defect model. *ACS Appl. Mater. Interfaces*, 8(8):5687–5693, 2016.

[183] J. Maier. Space-charge regions in solid 2-phase systems and their conduction contribution .1. conductance enhancement in the system ionic conductor-inert phase and application on agcl-al2o3 and agcl-sio2. *J. Phys. Chem. Solids*, 46(3):309–320, 1985.

[184] X. X. Guo and J. Maier. Comprehensive modeling of ion conduction of nanosized caf2/baf2 multilayer heterostructures. *Adv. Funct. Mater.*, 19(1):96–101, 2009.

[185] Xiangxin Guo, Ion Matei, Janez Jamnik, Jong-Sook Lee, and Joachim Maier. Defect chemical modeling of mesoscopic ion conduction in nanosized $\mathrm{Caf_2Baf_2}$ multilayer heterostructures. *Phys. Rev. B*, 76:125429, Sep 2007.

[186] C. Li, L. Gu, X. Guo, D. Samuelis, K. Tang, and J. Maier. Charge carrier accumulation in lithium fluoride thin films due to li-ion absorption by titania (100) subsurface. *Nano Lett.*, 12(3):1241–6, 2012.

[187] K. F. Young and H. P. R. Frederikse. Compilation of the static dielectric constant of inorganic solids. *J. Phys. Chem. Ref. Data*, 2(2):313–410, 1973.

[188] J. Vetter, P. Novak, M. R. Wagner, C. Veit, K. C. Moller, J. O. Besenhard, M. Winter, M. Wohlfahrt-Mehrens, C. Vogler, and A. Hammouche. Ageing mechanisms in lithium-ion batteries. *J. Power Sources*, 147(1-2):269–281, 2005.

[189] J. M. Tarascon and M. Armand. Issues and challenges facing rechargeable lithium batteries. *Nature*, 414(6861):359–367, 2001.

[190] P. Verma, P. Maire, and P. Novak. A review of the features and analyses of the solid electrolyte interphase in li-ion batteries. *Electrochim. Acta*, 55(22):6332–6341, 2010.

[191] C. C. Nguyen and B. L. Lucht. Comparative study of fluoroethylene carbonate and vinylene carbonate for silicon anodes in lithium ion batteries. *J. Electrochem. Soc.*, 161(12):A1933–A1938, 2014.

[192] R. Elazari, G. Salitra, G. Gershinsky, A. Garsuch, A. Panchenko, and D. Aurbach. Li ion cells comprising lithiated columnar silicon film anodes, tis2 cathodes and fluoroethyene carbonate (fec) as a critically important component. *J. Electrochem. Soc.*, 159(9):A1440–A1445, 2012.

[193] K. Schroder, J. Avarado, T. A. Yersak, J. C. Li, N. Dudney, L. J. Webb, Y. S. Meng, and K. J. Stevenson. The effect of fluoroethylene carbonate as an additive on the solid electrolyte interphase on silicon lithium-ion electrodes. *Chem. Mater.*, 27(16):5531–5542, 2015.

[194] K. Leung, Y. Qi, K. R. Zavadil, Y. S. Jung, A. C. Dillon, A. S. Cavanagh, S. H. Lee, and S. M. George. Using atomic layer deposition to hinder solvent decomposition in lithium ion batteries: First-principles modeling and experimental studies. *J. Am. Chem. Soc.*, 133(37):14741–14754, 2011.

[195] P. Ganesh, P. R. C. Kent, and D. E. Jiang. Solid-electrolyte interphase formation and electrolyte reduction at li-ion battery graphite anodes: Insights from

first-principles molecular dynamics. *J. Phys. Chem. C*, 116(46):24476–24481, 2012.

[196] Hyun Choia Cao Cuong Nguyen and Seung-Wan Song. Roles of oxygen and interfacial stabilization in enhancing the cycling ability of silicon oxide anodes for rechargeable lithium batteries. *J. Electrochem. Soc.*, 160(6):A906–A914, 2013.

[197] H. Wu, G. Chan, J. W. Choi, I. Ryu, Y. Yao, M. T. McDowell, S. W. Lee, A. Jackson, Y. Yang, L. B. Hu, and Y. Cui. Stable cycling of double-walled silicon nanotube battery anodes through solid-electrolyte interphase control. *Nat. Nanotechnol.*, 7(5):310–315, 2012.

[198] M. N. Obrovac, L. Christensen, D. B. Le, and J. R. Dahn. Alloy design for lithium-ion battery anodes. *J. Electrochem. Soc.*, 154(9):A849–A855, 2007.

[199] L. Y. Beaulieu, K. W. Eberman, R. L. Turner, L. J. Krause, and J. R. Dahn. Colossal reversible volume changes in lithium alloys. *Electrochem. Solid State Lett.*, 4(9):A137–A140, 2001.

[200] M. J. Chon, V. A. Sethuraman, A. McCormick, V. Srinivasan, and P. R. Guduru. Real-time measurement of stress and damage evolution during initial lithiation of crystalline silicon. *Phys. Rev. Lett.*, 107:045503, Jul 2011.

[201] Jie Pan, Qinglin Zhang, Juchuan Li, Matthew J. Beck, Xingcheng Xiao, and Yang-Tse Cheng. Effects of stress on lithium transport in amorphous silicon electrodes for lithium-ion batteries. *Nano Energy*, 13:192–199, 2015.

[202] Mark W. Verbrugge, Daniel R. Baker, Xingcheng Xiao, Qinglin Zhang, and Yang-Tse Cheng. Experimental and theoretical characterization of electrode materials that undergo large volume changes and application to the lithium-silicon system. *J. Phys. Chem. C*, 119(10):5341–5349, 2015.

[203] M. Aykol, S. Kirklin, and C. Wolverton. Thermodynamic aspects of cathode coatings for lithium-ion batteries. *Adv. Energy Mater.*, 4(17), 2014.

[204] Y. Q. Wang, L. Guo, Y. G. Guo, H. Li, X. Q. He, S. Tsukimoto, Y. Ikuhara, and L. J. Wan. Rutile-tio2 nanocoating for a high-rate li4ti5o12 anode of a lithium-ion battery. *J. Am. Chem. Soc.*, 134(18):7874–7879, 2012.

[205] K. Xu, Z. F. Jie, R. H. Li, Z. X. Chen, S. T. Wu, J. F. Gu, and J. Z. Chen. Synthesis and electrochemical properties of caf2-coated for long-cycling li[mn1/3co1/3ni1/3]o-2 cathode materials. *Electrochim. Acta*, 60:130–133, 2012.

[206] S. Q. Hao and C. Wolverton. Lithium transport in amorphous al2o3 and alf3 for discovery of battery coatings. *J. Phys. Chem. C*, 117(16):8009–8013, 2013.

[207] S. Q. Shi, P. Lu, Z. Y. Liu, Y. Qi, L. G. Hector, H. Li, and S. J. Harris. Direct calculation of li-ion transport in the solid electrolyte interphase. *J. Am. Chem. Soc.*, 134(37):15476–15487, 2012.

[208] K. Leung and J. L. Budzien. Ab initio molecular dynamics simulations of the initial stages of solid-electrolyte interphase formation on lithium ion battery graphitic anodes. *Phys. Chem. Chem. Phys.*, 12(25):6583–6586, 2010.

[209] R. Dreyfus and A. Nowick. Ionic conductivity of doped nacl crystals. *Phys. Rev.*, 126(4):1367–1377, 1962.

[210] T. Takahashi, H. Iwahara, and T. Ishikawa. Ionic-conductivity of doped cerium trifluoride. *J. Electrochem. Soc.*, 124(2):280–284, 1977.

[211] N. J. Dudney. Composite electrolytes. *Annu. Rev. Mater. Sci.*, 19:103–120, 1989.

[212] T. Jow and J. B. Wagner. Effect of dispersed alumina particles on the electrical-conductivity of cuprous chloride. *J. Electrochem. Soc.*, 126(11):1963–1972, 1979.

[213] O. Nakamura and J. B. Goodenough. Conductivity enhancement of lithium bromide monohydrate by al2o3 particles. *Solid State Ionics*, 7(2):119–123, 1982.

[214] Chilin Li, Lin Gu, and Joachim Maier. Enhancement of the li conductivity in lif by introducing glass/crystal interfaces. *Adv. Funct. Mater.*, 22(6):1145–1149, 2012.

[215] X. X. Guo, I. Matei, J. S. Lee, and J. Maier. Ion conduction across nanosized caf2/baf2 multilayer heterostructures. *Appl. Phys. Lett.*, 91(10), 2007.

[216] H. Maekawa, R. Tanaka, T. Sato, Y. Fujimaki, and T. Yamamura. Size-dependent ionic conductivity observed for ordered mesoporous alumina-lii composite. *Solid State Ionics*, 175(1-4):281–285, 2004.

[217] J. Maier. Point-defect thermodynamics and size effects. *Solid State Ionics*, 131(1-2):13–22, 2000.

[218] J. Maier. Ionic transport in nano-sized systems. *Solid State Ionics*, 175(1-4):7–12, 2004.

[219] H. E. Roman, A. Bunde, and W. Dieterich. Conductivity of dispersed ionic conductors - a percolation model with 2 critical-points. *Phys. Rev. B*, 34(5):3439–3445, 1986.

[220] Qinglin Zhang, Jie Pan, Peng Lu, Zhongyi Liu, Mark W. Verbrugge, Brian W. Sheldon, Yang-Tse Cheng, Yue Qi, and Xingcheng Xiao. Synergetic effects of inorganic components in solid electrolyte interphase on high cycle efficiency of lithium ion batteries. *Nano Lett.*, 16(3):2011–2016, 2016.

[221] N. Sata, K. Eberman, K. Eberl, and J. Maier. Mesoscopic fast ion conduction in nanometre-scale planar heterostructures. *Nature*, 408(6815):946–949, 2000.

[222] J. Garcia-Barriocanal, A. Rivera-Calzada, M. Varela, Z. Sefrioui, E. Iborra, C. Leon, S. J. Pennycook, and J. Santamaria. Colossal ionic conductivity at interfaces of epitaxial zro2 : Y2o3/srtio3 heterostructures. *Science*, 321(5889):676–680, 2008.

[223] J. Maier. Nanoionics: Ionic charge carriers in small systems. *Phys. Chem. Chem. Phys.*, 11(17):3011–3022, 2009.

[224] G. Kresse and J. Furthmüller. Efficient iterative schemes for *ab initio* total-energy calculations using a plane-wave basis set. *Phys. Rev. B*, 54:11169–11186, Oct 1996.

[225] J. Maier. Space-charge regions in solid 2-phase systems and their conduction contribution .3. defect chemistry and ionic-conductivity in thin-films. *Solid State Ionics*, 23(1-2):59–67, 1987.

[226] A. v Cresce, S. M. Russell, D. R. Baker, K. J. Gaskell, and K. Xu. In situ and quantitative characterization of solid electrolyte interphases. *Nano Lett.*, 14(3):1405–12, 2014.

[227] L. M. Suo, O. Borodin, T. Gao, M. Olguin, J. Ho, X. L. Fan, C. Luo, C. S. Wang, and K. Xu. "water-in-salt" electrolyte enables high-voltage aqueous lithium-ion chemistries. *Science*, 350(6263):938–943, 2015.

[228] Z. Hashin and S. Shtrikman. A variational approach to the theory of the elastic behaviour of multiphase materials. *J. Mech. Phys. Solids*, 11(2):127–140, 1963.

[229] Oleg Borodin and Dmitry Bedrov. Interfacial structure and dynamics of the lithium alkyl dicarbonate sei components in contact with the lithium battery electrolyte. *J. Phys. Chem. C*, 118(32):18362–18371, 2014.

Vita

Education

- **Ph.D.**, Materials Science and Engineering, University of Kentucky 2016
- **B.S.**, Applied Physics, Jinan University, Guangzhou, China 2009

Journal publications

1. Tao Chen, Qinglin Zhang, Jiagang Xu, Jie Pan, Yang-Tse Cheng*, "Binder-free lithium ion battery electrodes made of silicon and pyrolized lignin," ***RSC Advances*** 6 (35), 29308-29313 (2016);

2. Qinglin Zhang, Jie Pan *(co-first author)*, Peng Lu, Zhongyi Liu, Mark W. Verbrugge, Brian W. Sheldon, Yang-Tse Cheng*, Yue Qi*, Xingcheng Xiao*, ***Nano Letters*** 16(3), 2011-2016 (2016);

3. Jie Pan*, Qinglin Zhang, Xingcheng Xiao, Yang-Tse Cheng*, Yue Qi*, ***ACS Applied Materials & Interfaces*** 8(8), 5687-5693 (2016);

4. Bo Lu, Yicheng Song*, Qinglin Zhang, Jie Pan, Yang-Tse Cheng, Junqian Zhang*, ***Physical Chemistry Chemical Physics*** 18, 4721-4727 (2016);

5. Jiagang Xu, Rutooj D. Deshpande*, Jie Pan, Yang-Tse Cheng, Vincent S. Battaglia, ***Journal of the Electrochemical Society*** 162 (10), A2026-A2035 (2015);

6. Jie Pan*, Yang-Tse Cheng*, Yue Qi*, ***Physical Review B*** 91 (13), 134116 (2015);

7. Jie Pan, Qinglin Zhang, Juchuan Li, Matthew J. Beck, Xingcheng Xiao, Yang-Tse Cheng*, ***Nano Energy*** 13, 192-199 (2015);
8. Lei Han, Jie Pan, Qinglin Zhang, Shibin Li, Zhi Chen*, ***ECS Journal of Solid State Science and Technology*** 3 (12), N155-N160 (2014);

Technical presentations

1. Jie Pan, "Electrical conduction in electrodes and at interphases for lithium ion batteries," National Renewable Energy Laboratory, Golden, CO, February 29, 2016. (Invited)
2. Jie Pan, Yang-Tse Cheng, Yue Qi, "The Role of Interfaces on Ionic and Electronic Transport in Solid Electrolyte Interphases," *Materials Research Society Fall Meeting & Exhibit*, Boston, MA, 2015. (Abstract No. PP2.09, Oral)
3. Jie Pan, Yue Qi, Yang-Tse Cheng, "Ionic and Electronic Conduction in Solid Electrolyte Interphases on Silicon Electrodes," *Materials Research Society Spring Meeting & Exhibit*, San Francisco, CA, 2015. (Abstract No. I1.07, Oral)
4. Jie Pan, Yue Qi, Yang-Tse Cheng, "Defect and Ionic Transport in Li-ion Batteries," *Kentucky Renewable Energy & Energy Efficiency Workshop*, Louisville, KY, 2015 (Poster)
5. Jie Pan, Yang-Tse Cheng, Yue Qi, "Defect Formation and Ionic Conduction in Lithium Fluoride - A Component in Solid Electrolyte Interphase for Lithium Ion Batteries," *Materials Research Society Fall Meeting & Exhibit*, Boston, MA, 2014. (Abstract No. Z10.11, Oral)
6. Jie Pan, Matthew J. Beck, Yang-Tse Cheng, "Transport Behavior of Lithium in Silicon and Germanium Electrodes for Lithium Ion Batteries," *Materials Science & Technology*, Pittsburgh, PA, 2014. (Oral)

7. Jie Pan, Yang-Tse Cheng, Yue Qi, “The Function of Lithium Fluoride in Solid Electrolyte Interface for Lithium-ion Batteries,” *The 40th annual American Vacuum Society - Michigan Chapter Symposium - Thin films for Energy Storage and Conversion Applications*, East Lansing, MI, 2014. (Poster)

8. Jie Pan, Yang-Tse Cheng, Matthew J. Beck, “Effects of Stress and State-of-Charge on Lithium Transport Behavior in Silicon Electrodes,” *225th Electrochemical Society Meeting*, Orlando, FL, 2014 (Abstract No. 339, Oral)

Professional services and memberships

- **Chair (Co-Founder)**, Electrochemical Society Kentucky Student Chapter 2014 - 2016

- **Treasurer**, Materials Research Society UK Chapter 2014 - 2016

- **Member** of the American Physical Society, the Electrochemical Society, and Materials Research Society

Awards

- Outstanding Graduate Student Award, University of Kentucky, Lexington, KY, 2016

- Poster Award, Renewable Energy & Energy Efficiency Workshop, Louisville, KY, 2015

- Travel Grant for the 225^{th} ECS Meeting, Battery Division ECS, Orlando, FL, 2014

- Student Fellowship, Lawrence Berkeley National Laboratory, 2013